1985

Influence on the mechanical properties of electroless copper deposits in multilayer interconnection board (MIB)-plated through hole (PTH) applications /

Kenneth Scott Vecchio
Lehigh University

INFLUENCES ON THE MECHANICAL PROPERTIES OF ELECTROLESS COPPER DEPOSITS IN MULTILAYER INTERCONNECTION BOARD (MIB)-PLATED THROUGH HOLE (PTH) APPLICATIONS

by

Kenneth Scott Vecchio

A Thesis

Presented to the Graduate Committee

in Candidacy for the Degree of

Master of Science

in

Metallurgy and Materials Engineering

Lehigh University

1985

CERTIFICATE OF APPROVAL

This thesis is accepted and approved in partial fulfillment of the requirements for the degree of Master of Science.

May 6, 1985

Date

Professor in Charge

Department Chairperson

ACKNOWLEDGEMENTS

I wish to express my sincere gratitude to Dr. R. W. Hertzberg for his guidance, patience, and support throughout this research project. Thanks are also extended to Dr. D. B. Williams and Dr. J. R. Michael for their help and suggestions regarding the microscopy work.

I would like to express my gratitude to the International Business Machines Corporation, and in particular, to D. Seriphim, C. K. Lim, L. Lee, and V. S. Darekar for providing the materials and funds for this research.

Special thanks are extended to my brother, Robert, for his help in developing the Finite Element Models in this study, and for his many hours of discussion on this project. I am profoundly grateful. The assistance of Dr. M. McGirr in discussing the Analytical PTH Model is also greatly appreciated.

Many thanks are extended to the technical staff at both Whitaker and Coxe Laboratories, and also to my fellow graduate students for their assistance. In particular, I would like to thank Sailesh Merchant and Charles Robino for their time and discussions during the preparation of this manuscript, and to George Rommal for conducting the Auger work in this study. Thanks are also extended to Betty Zdinak for her work in producing this now readable manuscript.

I would like to thank my parents for their support and understanding which allowed me to give so much time to this research.

Finally, I would like to thank my financee, Cynthia, for her encouragement and understanding during the course of this work. Her

efforts and commitment throughout this project have been significant. I am truly grateful.

TABLE OF CONTENTS

LIST OF FIGURES

LIST OF TABLES

ABSTRACT

The thermomechanical deformation of plated-through-holes (PTHs) in multilayer interconnection boards (MIBs) has been examined with the aim of developing a suitable test methodology for evaluating the long term reliability of electroless copper PTH structures. The concern over PTH reliability comes from the large Z-direction (through-thickness) thermal expansion coefficient mismatch between the epoxy-glass and copper which generates stresses when the MIB is subjected to a temperature change.

Analytical and finite element modeling of the PTH is used to calculate the stresses and strains in the copper barrel section of the PTH. A test methodology and failure criterion were developed to allow critical evaluation of the influence of significant design and material parameter changes on the cyclic strain fatigue life of PTHs. The use of acoustic emission techniques to monitor the fatigue tests revealed that when delamination along the copper/epoxy-glass interface occurred, it was invariably linked to reduced life. A constitutive relationship relating the cyclic life as a function of applied cyclic strain was derived from the results.

Also discussed are several analytical techniques used in investigating the cause of the reported low ductility of electroless copper. It was found that electroless copper is an inherently ductile material with the reported low ductility believed to be an artifact of the technique used to evaluate the ductility of the material.

I. INTRODUCTION

The demands for increased performance of large computer systems have produced a corresponding increase in the complexity of printed circuit boards. The natural evolution of single-sided and double-sided printed circuit boards has led to the development of the multilayer interconnection board, or MIB, which has been used extensively in the high density electronic interconnection/packaging industry. With the increased complexity and packaging density of the MIBs, the demand for more numerous and reliable interconnections has grown in proportion. In general, the interconnection of the various conduction layers in MIBs is accomplished by means of copper plated-through holes (PTHs). A schematic diagram showing the typical interconnections in a MIB is given in Figure 1.

Although the concept of the plated-through-hole (PTH) has been accepted and widely utilized in the electronic interconnection/packaging industry, it is well known [1-3] that the majority of electrical continuity failures associated with multilayer interconnection boards are due to PTH failures. Such failures have been associated with the fact that the epoxy-glass composite substrates, currently used in MIBs, have a coefficient of thermal expansion in the board thickness direction that is several times larger than that of the copper PTH; this mismatch in thermal coefficients is generally believed to be responsible for the thermomechanical deformation and fracture of PTHs. Accordingly, pessimism in the industry regarding the PTH reliability has created increased interest in understanding the PTH structure and its

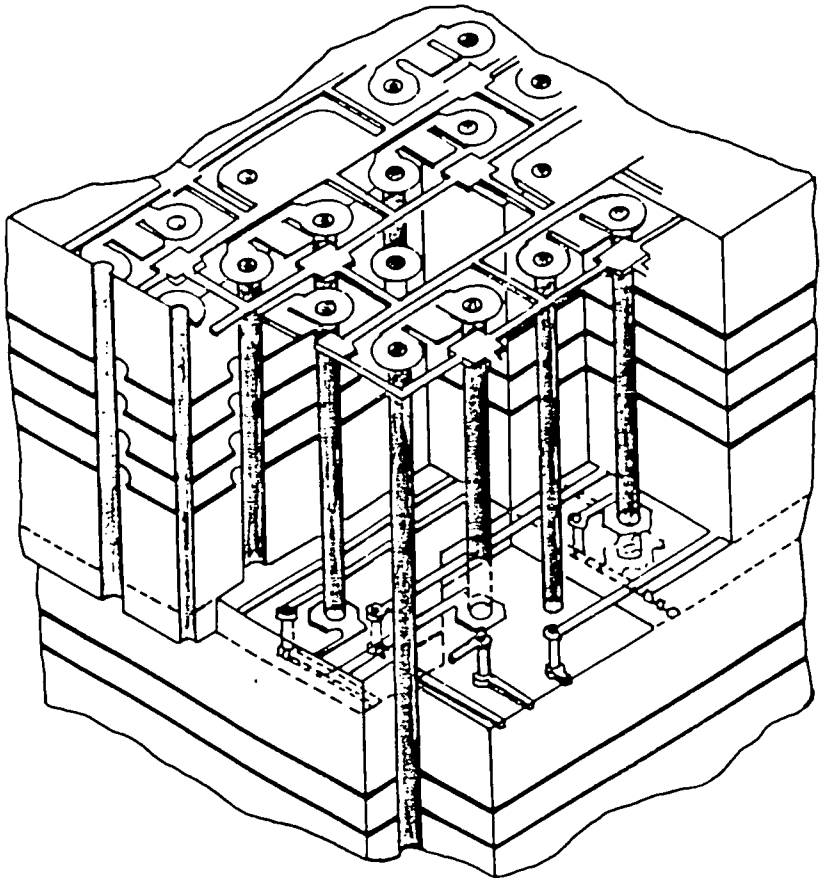

Figure 1: Schematic diagram of a multilayer interconnection board showing typical interconnections (after Seraphim [5]).

thermomechanical response. A typical cross-section of a PTH barrel-land structure is shown in Figure 2.

The thermomechanical failures of plated through holes in MIBs are of two principal types: 1) PTH barrel cracks extending around the circumference of the barrel, and 2) interfacial fractures occurring at the junction of interplanar copper lands and the PTH barrel. The thermal stimuli for these thermo-mechanical failures are generally the result of either a soldering transient of up to 250°C during the initial MIB make up, or due to in-service thermal cycling associated with normal on/off procedures.

Recently, the interconnection/packaging industry replaced the usual electro-plated copper technology, for producing MIBs, with a new, economical electroless copper plating technique. This electro-less plating process allows for metal films to be deposited directly on to non-metallic substrates after a simple surface activation treatment.

Unfortunately, the ductility of electroless copper ($\sim$2-7%) [4] is generally less than that of electroplated copper ($\sim$12-20%) [1], even though copper is intrinsically a ductile material. Since the ductility of electroless copper is 3 to 10 times less than that of electroplated copper, MIBs plated with electroless copper are significantly more susceptible to PTH barrel cracking. As such, the lower ductility of electroless copper permits less tolerance in the PTH to the thermal strain associated with thermal transients.

To develop and manufacture economical multilayer interconnection boards with high PTH reliability, it is necessary to identify the

Figure 2: Optical micrograph showing a typical PTH structure from an IBM 3081 processor unit.

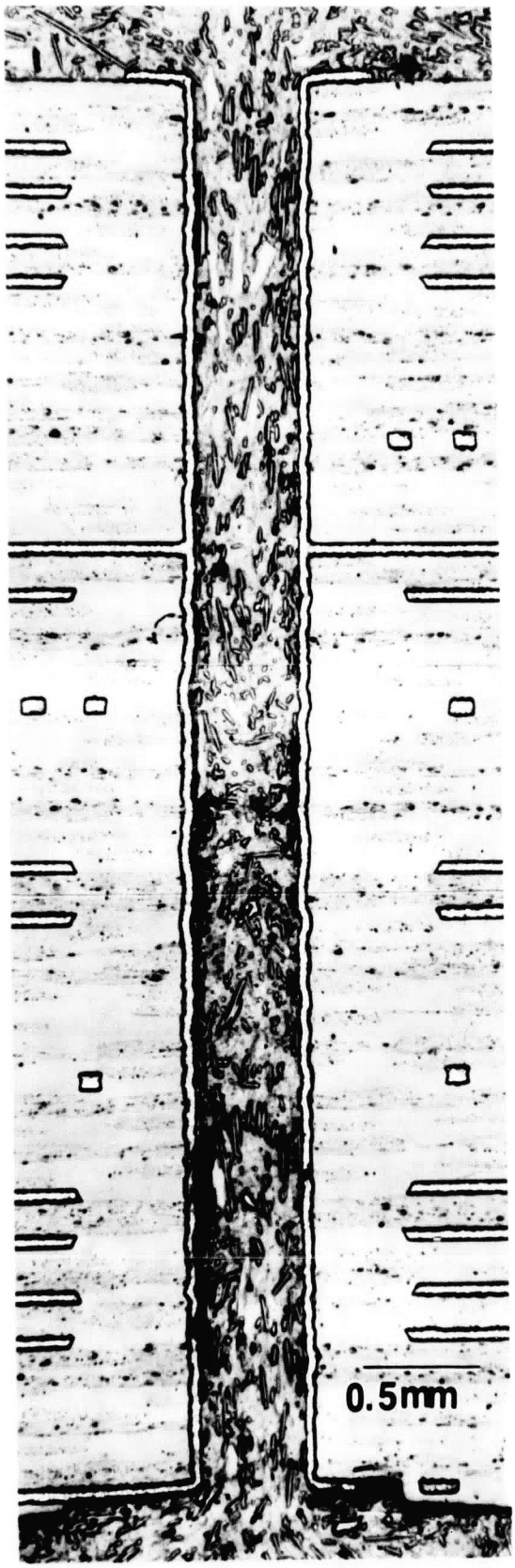
0.5mm

influence of design, process, and material parameters on the reliability of PTHs in MIBs. Furthermore, the complex and highly variable nature of PTH manufacturing processes and electroless copper deposition makes assessment of the influence of these various parameters difficult from an empirical point of view. An understanding of basic failure mechanisms in an actual PTH structure is required in order to develop an experimental program which allows accurate assessment of the influence of these parameters on PTH reliability.

II. BACKGROUND

2.1 MIB-PTH STRUCTURE AND RELIABILITY

Recent developments in printed circuit technologies have permitted the manufacture of multilayer interconnection boards (MIBs) with greater circuit capacity and increased response speed. Seraphim [5] has described the basic design and manufacturing processes of the MIB for the IBM 3081 Processor Unit. Plated-through-holes (PTHs) are used for the interconnection of interplanar copper circuits with logic service terminals. The PTH is drilled in a two-stage mechanical drilling process, followed by abrasive and chemical cleaning to remove residual epoxy material. A through-hole aspect ratio of 11:1 is used and plating the hole is accomplished in an electroless copper bath. The plating process is carefully controlled to reduce impurity levels to ensure good copper quality.

IBM's 3081 multilayer interconnection board is believed to be the largest MIB currently being manufactured in the electronic interconnection/packaging industry (600 mm x 700 mm) with some 40,000 PTHs in each of its four boards. Since the failure of a single PTH may result in a computer shutdown, it is apparent that extremely high reliability is essential. Statistically, if only one in a million PTH failures occur, a relatively small number of processor units would be involved in generating a failure.

The principal factors to be considered with respect to PTH failure mechanisms are: 1) nominal stresses and strains due to thermal transients in well manufactured MIB-PTHs, 2) stress concentrations which result in local stress and strain amplification and 3)

the level of local ductility of the copper plating available to resist these stresses and strains. Clearly, an understanding of the relative importance and interdependence of these factors is necessary to assess PTH reliability.

2.1.1 PTH Failures

It is widely known that PTH failures can result from the thermomechanical deformation due to the thermal expansion coefficient mismatch between the epoxy-glass matrix and the copper PTH; such strains are generated by thermal transients during soldering operations.

The failures of PTHs associated with the soldering transient are of two principal types: 1) barrel cracks extending around the circumference of the PTH, and 2) fractures in the vicinity of the interface created by interplanar copper (land)-PTH barrel junction. Less widely known is the deformation in the PTH resulting from long term thermal cycling associated with in-service unit on/off operations. For long term thermal cycling, Oien [2] states that "if a PTH barrel remains uncracked during the initial soldering transient, it will generally require hundreds of rather severe thermal cycles to produce cyclic fatigue cracking of the barrel." In other words, defects initially present or cracks initiated during the soldering transient may propagate during subsequent thermal cycles. Thus, long term thermal cycling may be a viable mechanism for PTH barrel cracking.

Some conventional experimental techniques are too insensitive to detect barrel cracks initiated during the initial soldering transient. Failure to perceive these cracks may result in the misconception that

subsequent thermal cycling will not produce PTH fracture. Rudy [6] has developed a highly sensitive electrical technique for detecting these PTH barrel cracks, a modification of which was used to monitor copper cracking during cyclic fatigue tests in this study. The technique developed by Rudy is very useful for detecting PTH barrel cracking, but gives no indication as to whether debonding is occurring at the epoxy-glass/copper-barrel interface. Oien [2] pointed out that if debonding of the epoxy-glass from the copper barrel were to occur it would have a significant influence on PTH deformation. When an actual PTH structure is stressed in tension, a stress gradient is developed at the copper barrel epoxy-glass interface which may act to debond the interface. Since debonding is considered to be highly detrimental to the integrity of the PTH structure, detection of debonding is vital for predicting the reliability of the PTH.

2.1.2 PTH Stress Analyses

A simple analytical model has been developed by Oien [3] to understand the mechanics and thermomechanical deformation of a plated-through hole. Oien's model is based on a piece-wise linear approach (see Figure 3) which assumes common displacements between two linear elements (one copper, one epoxy-glass) as a function of temperature. The elastic strain in the copper element is given by:

$$\varepsilon_{Cu} = \frac{(\alpha_M - \alpha_{Cu})\ \Delta T}{1 + A_{Cu}Y_{Cu}/A_MY_M} \qquad (1)$$

where α_M and α_{Cu} are the thermal expansion coefficients for the epoxy-glass matrix and copper, respectively, Y_M and Y_{Cu} the

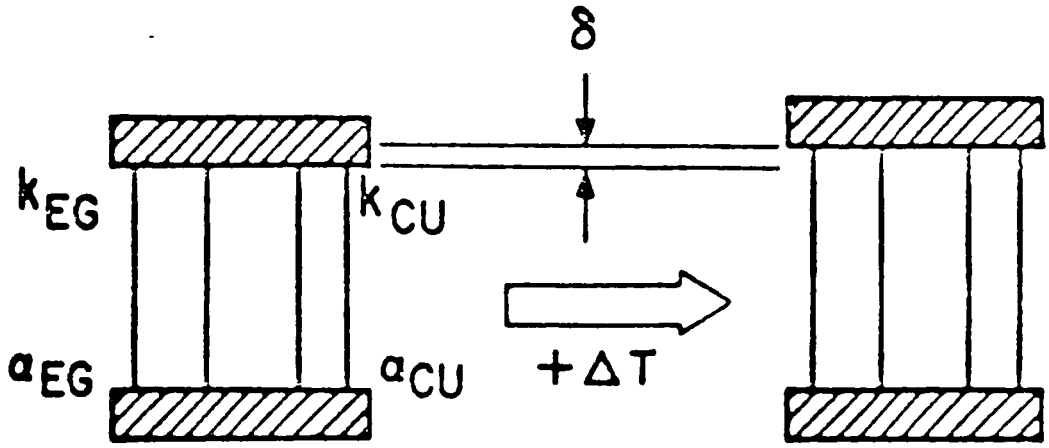

Figure 3: Oien's [3] simple model for Plated-Through-Hole Barrel Strains.

elastic moduli of epoxy-glass matrix and copper, respectively, A_M and A_{Cu} are the area of the epoxy-glass matrix and copper, respectively, and ΔT is the temperature change. Figure 4 shows Oien's calculated barrel strain versus temperature change from Equation 1.

Oien's model assumes the elements are straight, of uniform quality, defect free, and symmetrically stressed. From inspection of the PTH in Figure 2, it can be seen that all of the aforementioned assumptions do not describe the geometry and non-uniformity of an actual PTH structure. When good quality electroplated copper ($\sim$20% ductility) is employed, PTHs should be highly resistant to the formation of barrel cracks in well manufactured MIBs. Oien noted however, that manufacturing difficulties resulting in thinly plated regions, stress concentrations and/or material with low ductility may produce PTH failures.

Ammann and Jocher [17] have made direct measurements of the axial strain in the PTH barrel during an initial soldering transient. For a 16 layer MIB, maximum axial strains near the barrel center were on the order of 1.7% at 240°C. For a 20 layer MIB, as in the 3081, the axial strain near the barrel center is expected to be slightly higher, making them more susceptible to failure.

In an effort to improve the reliability of MIB-PTH structures and expand our understanding of the micromechanics of PTH failures, it is necessary to determine the effects of selected design and processing parameters on the deformation of PTH structures. Efficient evaluation of the effects of design and processing parameter on long term cyclic life can only be accomplished through accelerated test

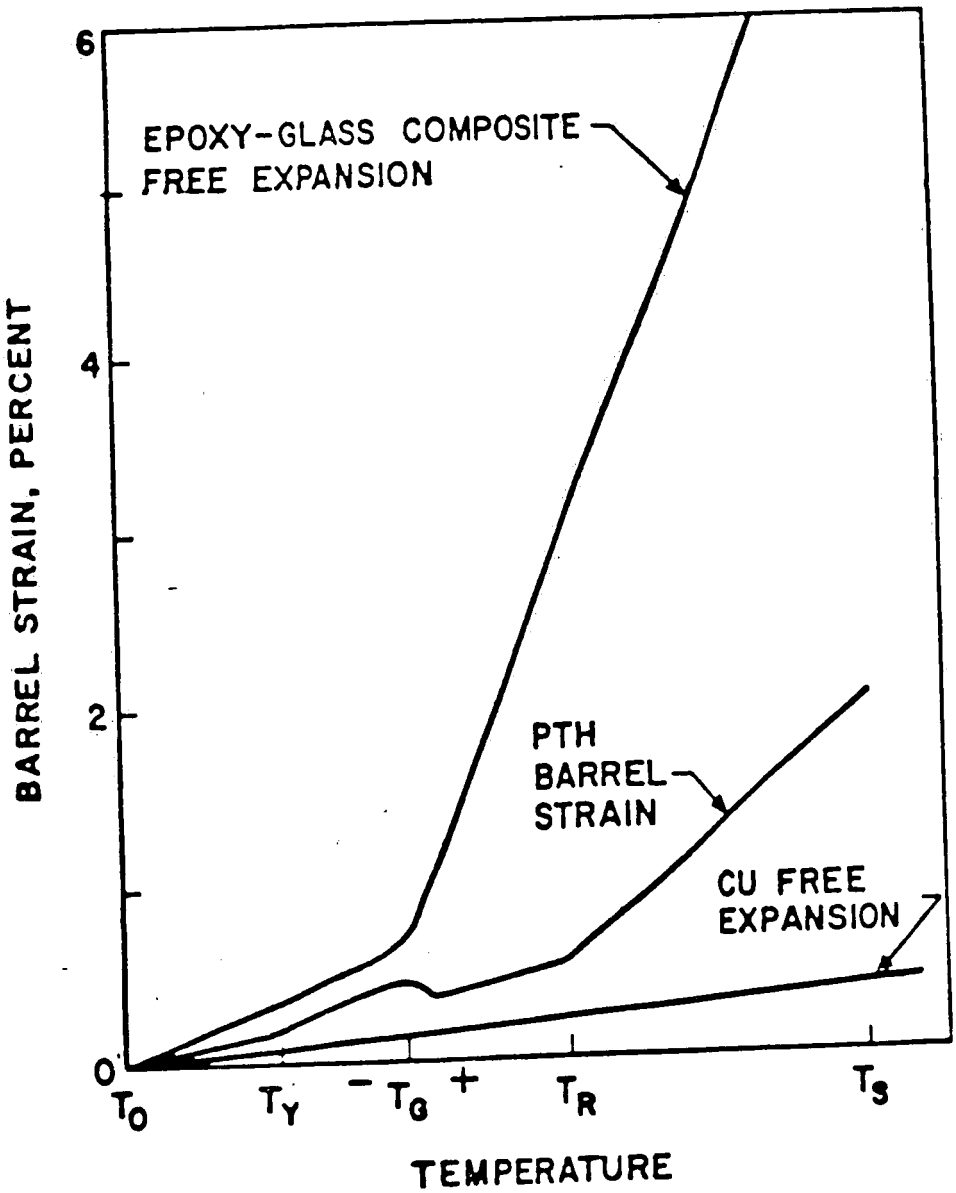

Figure 4: PTH barrel strain versus temperature based on the simple piece-wise linear model of Oien [3].

programs. The research described here is directed at developing such an accelerated test program.

2.2 DEPOSITED COPPER DUCTILITY

Anderson and Wild [8] studied the circumferential PTH barrel cracks present when electrodeposited copper PTH structures underwent the thermal transient associated with the soldering process. They observed that copper foil cracks developed within the relatively weak columnar grain boundaries of the electrodeposited copper. In general, foils with less than 1% elongation would crack, while foils with greater than 1% elongation would not. The authors concluded from TEM analysis that the only clear difference between the foils was the presence of a duplex grain structure in the lower ductility foils as opposed to the equiaxed structure of the higher ductility foils which exhibited tensile elongations of over 5%.

Fox [1] has reported elongation data for electroplated copper with values ranging from 1.5%-20% for various specimen thicknesses. Tensile and yield strengths were found to decrease with decreasing foil thickness though no parallel trend was observed for elongation values. Fox concluded, however, that elongation to failure is not a good measure of localized ductility because some necking occurs prior to failure which reduces the nominal elongation. Reduction in area is a better indication of localized ductility, however, this is difficult to measure for thin foils. In PTH applications, local ductility is a more important property than elongation to failure for assessing reliability.

Electroless copper deposits used in the fabrication of MIBs have been shown to possess better ductility when certain additives are incorporated into the plating bath [9,10]. Two general theories exist

to explain the effect of these additives on the foil ductility: 1) the formation and incorporation of $copper_2O$ is believed to be the cause of low ductility additives to serve to reduce the formation of this specie, and 2) copper deposits become embrittled as a result of hydrogen gas bubble incorporation with certain additives believed to serve to reduce the concentration of hydrogen in the deposits. Although no evidence for the incorporation of $copper_2O$ in electroless copper has been reported, Nakahara and Okinaka [11] noted the presence of hydrogen bubbles in copper deposits which reduced foil ductility. Their observations suggest that reduced ductility originates from small hydrogen bubbles present within the grains and not from larger voids present at grain boundaries. The small bubbles within grains are believed to act as obstacles to planar slip and result in hardening of the foils.

Electroless copper deposits are produced from plating baths which are constantly replenished over time. Replenishing the copper is generally accomplished by adding copper sulfate. As a result, sulfate ions accumulate in the bath over time. Homma et al. [12] recently found that sulfate ions incorporated into the deposits, adversely affected the ductility of electroless copper foils. Homma and Mizushima [4] have shown that when sulfate ion concentrations increase from 0.03 mol/L to 0.24 mol/L in the plating bath, electroless copper elongations decreased from 7% to 1-2% and tensile strength similarly decreased to a lesser extent; the presence of carbonate ions also showed the same tendency.

Aycock et al. [9] have used a spiral contractometer to measure the internal stresses in electroless copper. When certain additives were used in the plating bath, either a residual compressive or tensile stress was observed in the copper foils (Figure 5). The residual stresses were found to become more compressive with increasing foil thickness. Aycock suggests that residual tensile stresses could contribute to the lower ductility of the deposits. Others [10,11] have suggested that the presence of internal stresses cause pores to develop in the channels between the growing grains, thereby entrapping gases. However, no clear understanding of the interrelations of internal stresses and pores is currently available.

All of the above investigations fail to fully explain the influence of certain bath additives, contaminants, or residual stresses on the ductility of electroless copper. Furthermore, no clear explanation has been given for the consistently higher ductility reported for electroplated copper as compared with that for electroless copper.

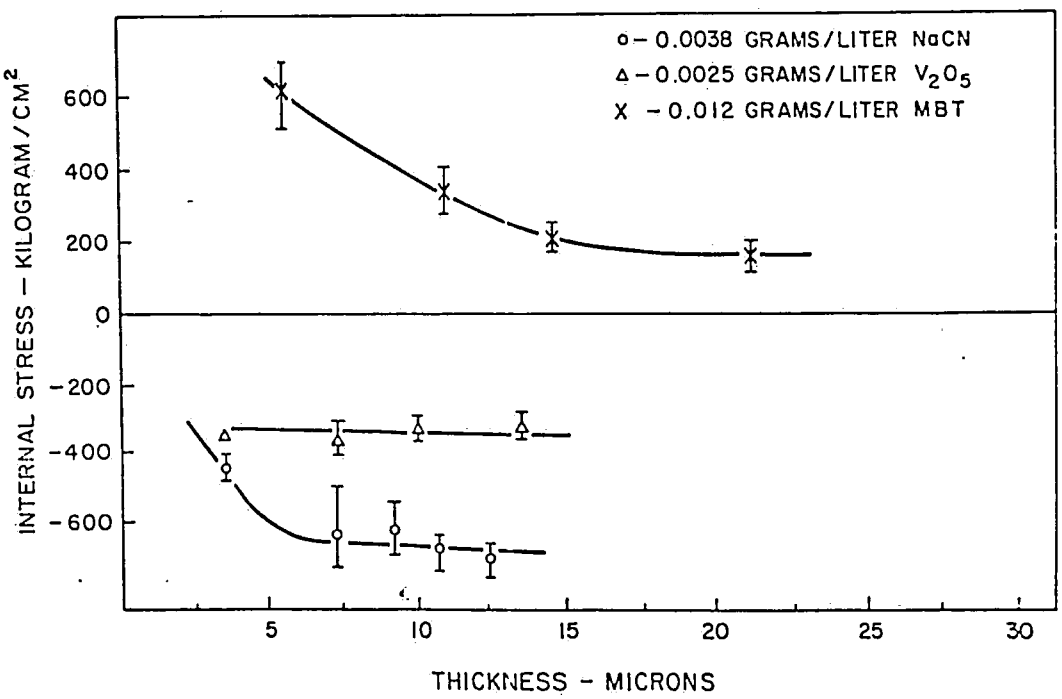

Figure 5: Internal stress versus thickness of Cu deposits from NaCN, V_2O_5 and MBT stabilized electroless baths (after Aycock et al. [9]).

2.3 EXPERIMENTAL TECHNIQUES

2.3.1 Acoustic Emission

Acoustic emission (AE) corresponds to high frequency stress waves generated by the rapid release of strain energy that occurs within a material during crack growth, plastic deformation or phase transformation. As such, AE can provide current information about the ongoing microscopic processes of fracture. AE analyses of fatigue and fracture toughness tests, stress corrosion cracking, hydrogen embrittlement, twinning deformation, martensitic phase transformations, deformation processes in welded joints, and other tests are becoming increasingly useful as a research tool. On a more practical side, AE testing is used as a non-destructive inspection method and has been applied in quality control systems. Because AE inspection is limited to the detection of an active flaw, AE testing must be applied while the material or structure is subjected to stress. Its ability to detect dynamic flaws makes AE a tool of increasing importance for monitoring crack growth and predicting life in components under stress.

Current AE technology employs transducers and amplifiers to detect the very faint stress waves emitted upon the release of strain energy within a material. Figure 6 shows a schematic diagram of an acoustic emission event and some pertinent features which may be used for its characterization. To this end, acoustic emission (AE) technology will be used in this study to elucidate information regarding copper deformation and debonding from the substrate during cyclic fatigue tests.

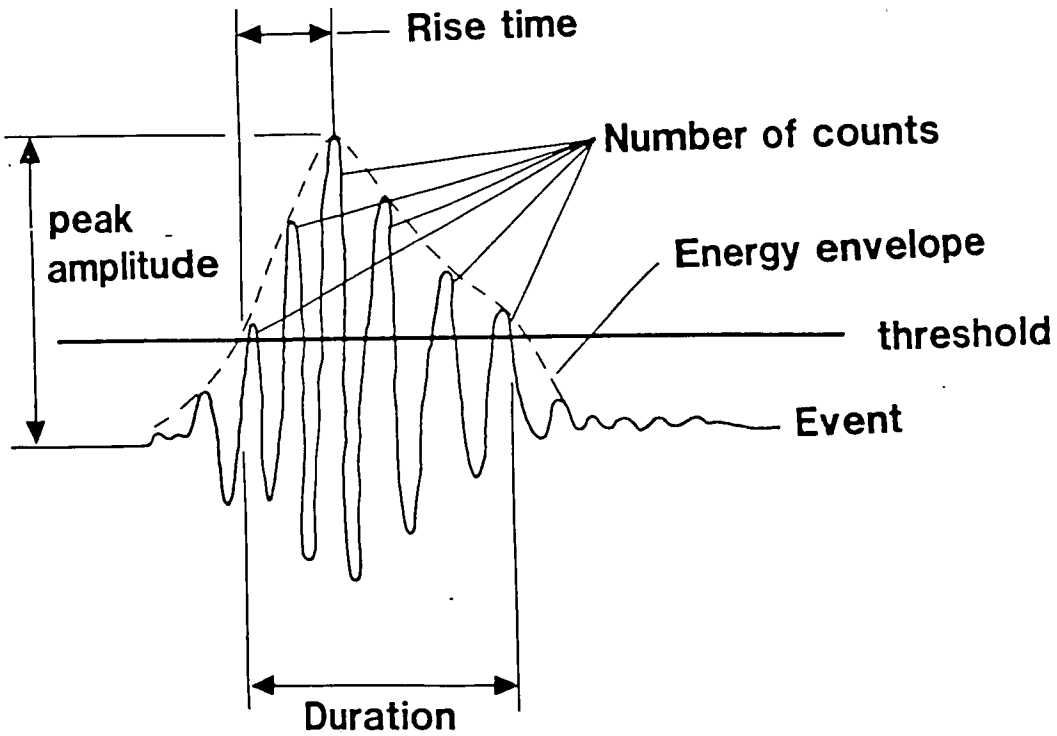

Figure 6: Schematic diagram of an acoustic emission event showing various features which may be used for its characterization.

2.3.2 Microscopy

Grain boundary embrittlement in metals can have a very detrimental effect on the mechanical properties of the material, particularly strength and ductility. The embrittlement phenomenon has been attributed to intergranular segregation of impurities to the grain boundaries, which is believed to reduce boundary cohesion. In the past, indirect techniques were used to study grain boundary segregation. The major disadvantage of these techniques is that they all require a prior knowledge of the segregating element as these techniques cannot distinguish the species that are segregating. Such indirect techniques rely on the measurement of the result of segregation. Usually these techniques are only qualitative in nature, except for those based on the measurement of grain boundary energy. Some of the indirect techniques are metallographic effects, microhardness measurements, kinetic effects, x-ray lattice parameter measurements, electrical properties [13] and grain boundary energy versus composition measurements [14].

Direct techniques involve the actual identification of the segregating species as well as quantitative measurement of the composition of the grain boundary. Two major direct techniques currently used are Scanning Transmission Electron Microscopy (STEM) with Energy Dispersive X-ray Spectroscopy (EDS) and Auger Electron Spectroscopy (AES).

i) Analytical Electron Microscopy

In recent years, the Analytical Electron Microscope (AEM) has shown increasing usefulness in studying the chemistry of

materials. The AEM, which refers to a STEM with EDS, allows for the identification and quantification of chemical species of atomic number 11 or greater. STEM allows the grain boundary to be viewed at high magnification, and by positioning the electron beam (which may be as small as 20Å) on the boundary, chemical analysis may be obtained by detecting the x-rays emitted by the sample. An x-ray spectrum, a plot of x-ray intensity vs. x-ray energy, can be generated from this analysis. This spectrum usually contains a number of x-ray peaks of specific energy corresponding to the elements present in the specimen, superimposed on a low level of background signal. In order to quantify such data, the peak intensities must be extracted from the EDS spectrum and converted to compositions using the Cliff-Lorimer ratio technique [15]. The AEM has been used to study grain boundary segregation in copper-bismuth [16,17] and in iron-3 wt% nickel with phosphorus and tin segregation [18-20]. The advantage of this technique is that the boundary need not be disturbed; thus, the technique may be used for systems that do not fracture intergranularly and the quantification of the x-ray data is easily achieved [21]. The disadvantages of AEM mainly involve the technique of specimen preparation and the x-ray spatial resolution.

ii) Auger Electron Spectroscopy

AES has become an important tool in the study of grain boundary segregation because of its high depth resolution and its ability to detect small amounts of a species. The analysis is carried out in a high vacuum after the sample has been fractured. The exposed fracture surface is then illuminated by an electron beam of 1-3 keV.

Auger electrons emitted by the sample are of low energy and, consequently escape from only the first few atom layers beneath the surface. As such this technique is very surface sensitive. Auger electrons have discrete energies characteristic of the species from which they were emitted. The Auger electrons are detected and displayed as sharp peaks in the energy derivation of the secondary electron spectrum. AES has been used to investigate segregation in copper-bismuth [22-24] in iron-3 wt% nickel with additions of phosphorus or tin [19] and in iron-tin [25] amongst others.

The main advantage of AES is its ability to identify the surface active species or species on the exposed grain boundaries. The major disadvantage of AES is the requirement that the sample be fractured to expose the grain boundary. This limits the technique to those systems in which the segregant causes greatly reduced grain boundary cohesion.

2.3.3 Strain Analysis Through Convergent Beam Electron Diffraction

In recent years, the development of instruments such as the AEM, which provides the ability to form focussed convergent electron probes, allows convergent beam electron diffraction (CBED) to be performed. When the parallel incident electron beam is made to converge at the specimen, the well defined spots in the parallel beam diffraction patterns are replaced by discs whose radii are proportional to the angular convergence of the incident beam. The discs in the CBED pattern may contain patterns of fine lines (dark or defect in the transmitted spot and bright or excess in the higher order zone spots) which are termed High Order Laue Zone lines or HOLZ lines.

The HOLZ lines represent elastic scattering effects corresponding to reflections in upper Laue layers, which occur in the intensity discs in the CBED patterns when the electron beam is accurately aligned parallel to certain zone axes [26]. The overall symmetry of these lines reflects the three-dimensional symmetry of the crystal structure from which they arise [27].

The position of the HOLZ lines is sensitive to the lattice parameter of the crystal and the electron wavelength of the illuminating beam. The sensitivity of HOLZ lines to the lattice parameter, thereby makes composition measurement possible through lattice parameter shifts [28,29]. Since the lattice parameter changes with lattice strain, HOLZ line positions can be used also to characterize residual strains in the lattice.

In order to perform absolute lattice parameter determinations using CBED patterns, a simulation technique was developed by Ecob et al.[26]. This technique requires a calibration specimen of known lattice parameter. Since the lattice parameter is known, the kV (and therefore wavelength) is then varied in the simulations to achieve good agreement between calculated and measured patterns. One difficulty of this technique is that, since dispersion effects are not accounted for, each different zone axis will have a unique value of the electron wavelength associated with it. If proper calibration techniques are used, the absolute lattice parameter may be measured to an accuracy of 2 parts in 10,000.

2.4 SUMMARY

At the present time there is no standard test method for evaluating the influence of design and processing parameters on the cyclic fatigue life of electroless copper in plated-through-holes. Furthermore, no definitive experiment has been described for testing thin metallic foils involving compressive loadings. Many studies have examined the thermomechanical deformation of the PTH structure during the initial soldering thermal transient; however, little attention has been given to the effects of long term thermal cycling on the PTH integrity.

Various methods have been developed for monitoring PTH barrel cracking, which have yielded varied success. Although some attention has been given to the thermomechanical debonding of the copper barrel from the epoxy-glass matrix, these studies have used post-mortem examinations of the interface to elucidate information regarding the debonding process.

There is much disagreement in the literature as to the origin of the reported low ductility of electroless copper. Numerous studies have identified various possible sources for this lower ductility and the elimination of these sources has yielded slightly improved properties. However, in some cases these ductilities have remained considerably lower than those reported for electroplated copper.

The objectives of this thesis are as follows:

1. Analyze the thermomechanical deformation of the PTH structure using analytical and finite element techniques.

2. Develop a suitable test methodology and failure criterion for evaluating the cyclic fatigue life of electroless copper in PTH applications.

3. Having established a test methodology, evaluate the influence of certain design, processing, and material parameters on the cyclic fatigue life of plated-through-holes.

4. Evaluate the usefulness of acoustic emission techniques for monitoring the failure mechanisms during cyclic fatigue testing.

5. Investigate the origin of the low reported ductility of electroless copper in PTHs.

III. EXPERIMENTAL AND ANALYTICAL PROCEDURES

3.1 PTH STRESS ANALYSES

3.1.1. Analytical Approach

In order to develop a better understanding of the PTH stress-strain relationship as a function of temperature, a simple, two-dimensional linear elastic stress analysis of the PTH structure was conducted. This stress analysis is an expansion of Oien's model and includes geometrical consideration of the PTH barrel-external land structure. The basic assumptions used in this analysis have been presented elsewhere [30], but will be restated below for clarity.

Assumptions:

1. The proportional limits of the materials involved are not exceeded (i.e. only elastic strains are allowed).

2. Thermal coefficient mismatch in the "Z" (thickness) direction is the primary cause of PTH stress with thermal effects of coefficient mismatch in the X and Y directions being minimal. Delamination between PTH structure and the epoxy-glass material is not considered in this analysis (see Figure 7).

3. The displacement of the PTH terminal area (lands) increases linearly from an amount ε at the barrel to $\alpha_M \cdot \Delta T$ at the land end; the curvature of the terminal area, associated with its deflection, is assumed to be negligible (see Figure 8).

4. The stresses are distributed uniformly throughout the PTH cross section (i.e. no stress concentrations or asymmetry).

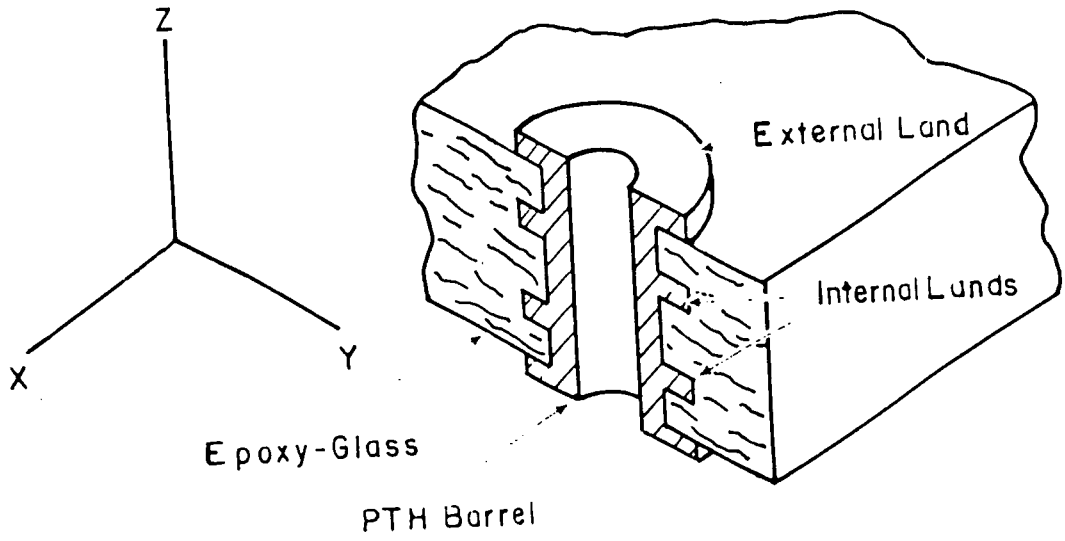

Figure 7: PTH cross section (after [30]).

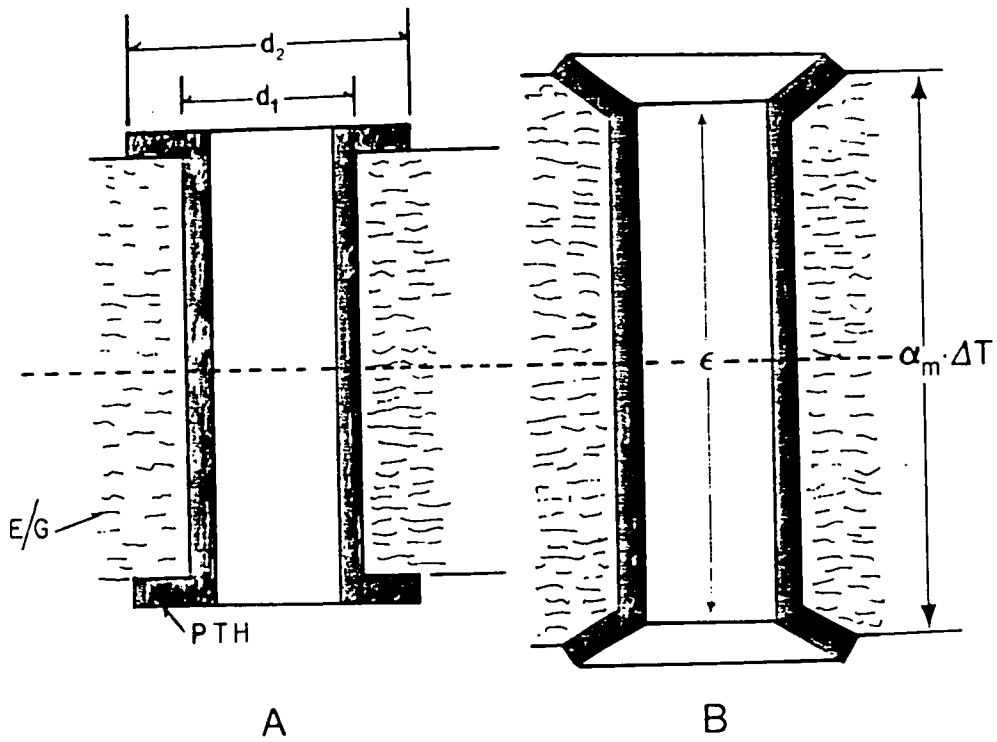

Figure 8: PTH deformation for a positive temperature change (after [30]).

Notation:

copper Barrel

A_b Area

Y_b Elastic modulus

α_b Thermal expansion coefficient

σ_b Elastic stress

ε_b Elastic strain

Epoxy-Glass Matrix

A_M Area

Y_M Elastic modulus

α_M Thermal expansion coefficient

σ_M Elastic stress

ε_M Elastic strain

Analysis

1. Assume barrel strain (thermal + elastic) = ε; free barrel strain would be $\alpha_b \cdot \Delta T$ (thermal only). Therefore, the barrel force (tension) = $Y_b A_b \{\varepsilon - \alpha_b \cdot \Delta T\}$

2. The matrix strain varies from the barrel strain (ε) near the barrel to $\alpha_M \cdot \Delta T$ at the end of the land; thus the average elastic matrix strain (ε_M) is:

$$\varepsilon_M = \{\alpha_M \Delta T - \underbrace{\frac{(\varepsilon + \alpha_M \cdot \Delta T)}{2}}_{\text{average total strain}}\} \tag{2}$$

$$\varepsilon_M = \{\frac{\alpha_M \cdot \Delta T}{2} - \frac{\varepsilon}{2}\} \tag{3}$$

$$\text{Matrix Force (compression)} = Y_M A_M \{\frac{\alpha_M \cdot \Delta T}{2} - \frac{\varepsilon}{2}\} \quad (4)$$

3. The forces are numerically equal:

$$Y_b A_b \{\varepsilon - \alpha_b \Delta T\} = Y_M A_M \frac{\alpha_M \Delta T}{2} - \frac{\varepsilon}{2} \quad (5)$$

leading to

$$\varepsilon = \frac{Y_M A_M \alpha_M + 2Y_b A_b \alpha_b}{Y_M A_M + 2Y_M A_M} \cdot \Delta T \quad (6)$$

Since $A_m >> A_b$ it can be assumed the area of the copper barrel is: (7)

$A_b \cong \pi dt$ and the area under the external land is:

$$A_M = \frac{\pi}{4} (\frac{d_2^2}{2} - \frac{d_1^2}{2})$$

4. Barrel Elastic Stress

$$\sigma_b = Y_b \{\varepsilon - \alpha_b \cdot \Delta T\}$$

$$\sigma_b = Y_b \frac{Y_M A_M \alpha_M + 2Y_b A_b \alpha_b \Delta T - Y_M A_M \alpha_b \Delta T - 2Y_b A_b \alpha_b}{Y_M A_M + 2Y_b A_b}$$

$$\sigma_b = Y_b \{\frac{(\alpha_M - \alpha_b) Y_M A_M}{Y_M A_M + 2Y_b A_b}\}$$

$$\sigma_b = Y_b \{\frac{(\alpha_M - \alpha_b) \Delta T}{1 + 2\frac{Y_b A_b}{Y_M A_M}}\} \quad (8)$$

$$\sigma_b / Y_b = \varepsilon_b$$

$$\varepsilon_b = \left\{\frac{(\alpha_M - \alpha_b)\Delta T}{1+2\frac{Y_b A_b}{Y_M A_M}}\right\} \qquad (9)$$

The total barrel strain is then shown to be equal to the elastic strain plus the free thermal expansion of the copper:

$$\varepsilon_{b_T} = \varepsilon_b + \alpha_b \Delta T \qquad (10)$$

This total copper barrel strain is plotted in Figure 16 against temperature change above ambient from 0 to 100°C.

3.1.2 Finite Element Analysis (FEA)

A more accurate stress analysis of the PTH structure and the cyclic strain fatigue specimen gage section was conducted using the APES [Axisymmetric/Planar Elastic Structures] finite element computer program. APES incorporates a high order isoparametric element with assumed bicubic displacements and can be used for plane strain, plane stress and axisymmetric structural behaviors. The program enables the solution of complex two-dimensional structural problems with less time and greater accuracy than most other public domain programs.

Idealizations of the PTH structure were developed for FEA. One PTH idealization shown in Figure 9 contains an external land, while the second idealization (Figure 10) contains both an external and internal land. Both idealizations model the PTH structure from the MIB midplane to one MIB surface.

Four basic assumptions are needed for the elastic stress analysis of the PTH structure by finite elements:

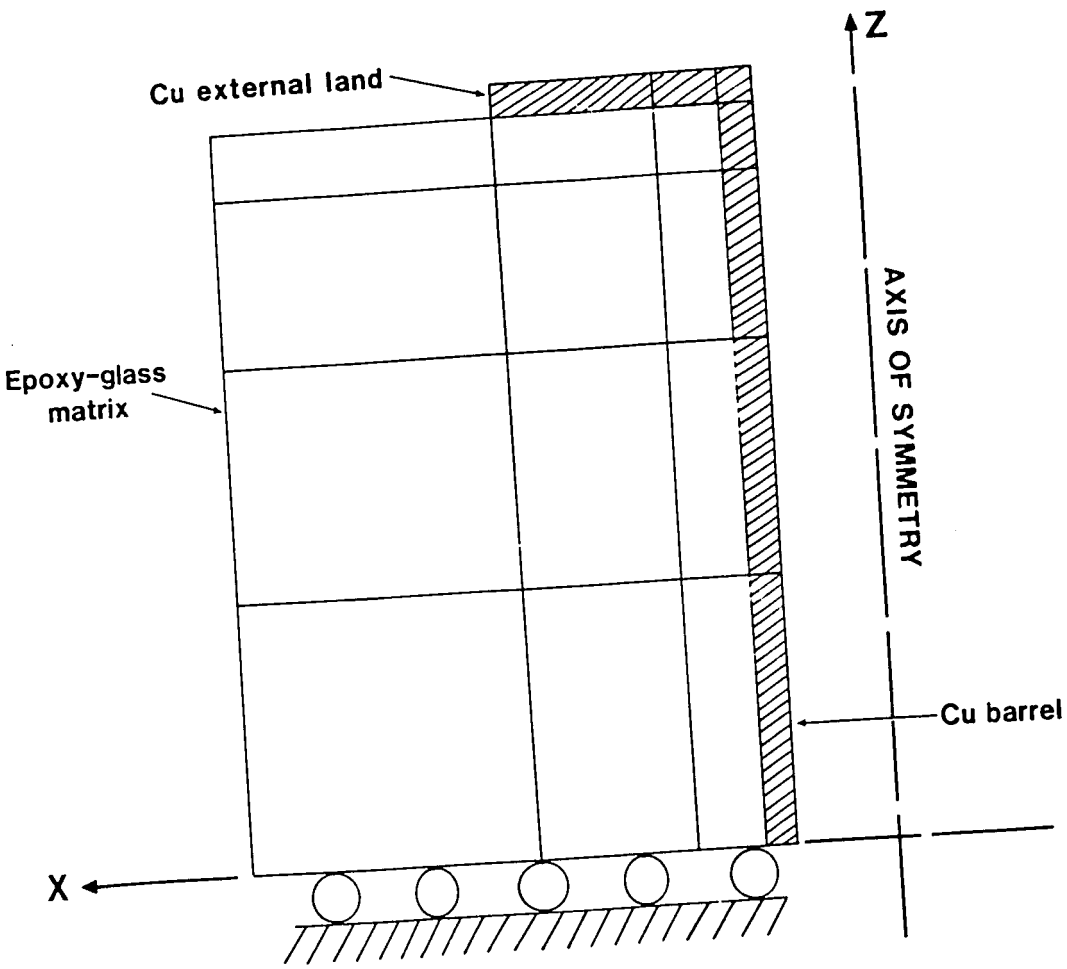

Figure 9: FEA PTH idealization #1 containing one external land.

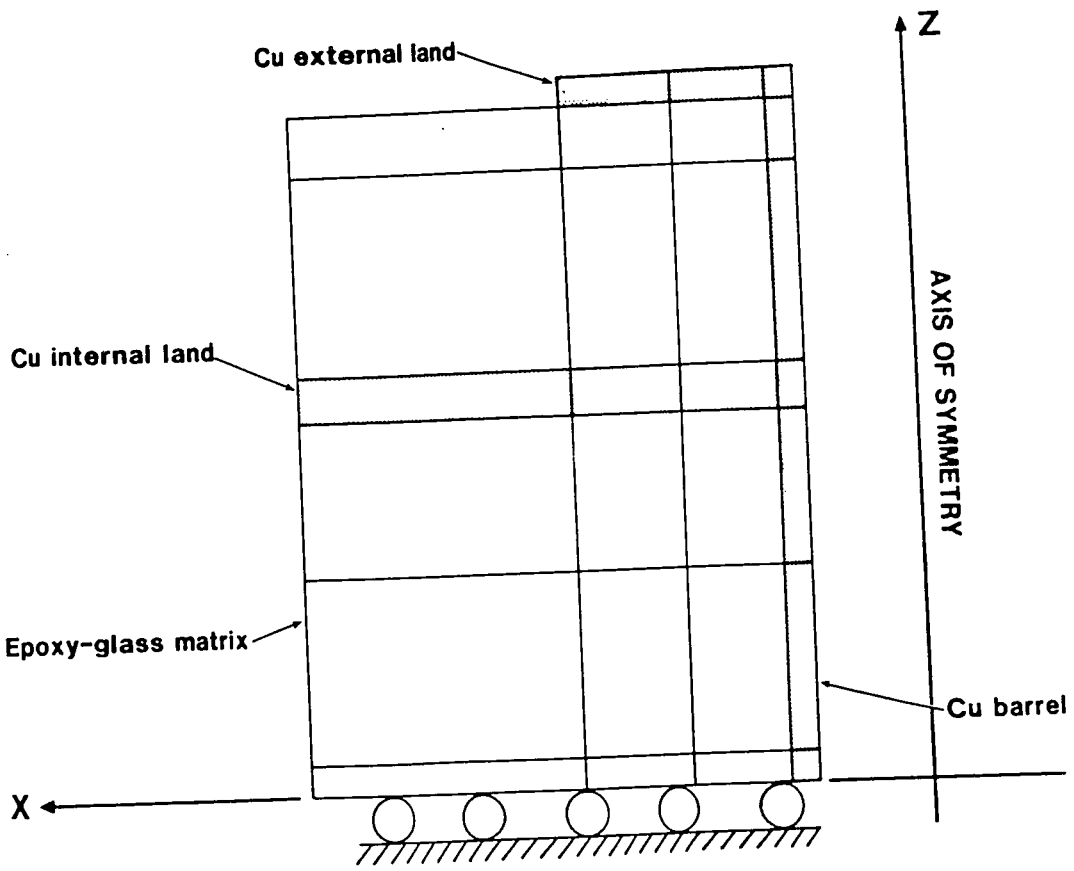

Figure 10: FEA PTH idealization #2 containing one external land and one internal land.

1. The material behavior is limited to linear elastic responses (i.e. no plasticity, an APES limitation).

2. Perfect adhesion exists between the PTH structure and the epoxy-glass matrix (i.e. no delamination).

3. The PTH wall is smooth and of uniform thickness (this assumption is for simplification of the analysis and is not a limitation of APES).

4. Thermal expansion is based on isotropic thermal expansion coefficients with the Z-direction* property being the primary cause of stresses within the PTH. (The need to consider an isotropic thermal expansion coefficient is a limitation of APES.)

Thermal loading was applied to the PTH idealized model by introducing a constant temperature for every element. Various results from the FEA can be graphically represented and superimposed on the idealized model such as x, y, and Von-Mises stresses, deflected structure, and strain energy density. The graphical representations of these results for both PTH idealizations, at various temperature changes in the MIB, appear in Appendix 1. Furthermore, the average and highest copper barrel y-strains for both idealized conditions are plotted versus temperature change (°C) in Figure 16.

*for the MIB, the through thickness direction corresponds to the Z-direction while in the FEA, it corresponds to the y-direction.

3.2 TENSILE AND CYCLIC STRAIN FATIGUE EXPERIMENTS

3.2.1 Monotonic Tensile Tests

Tension testing of the copper foils was conducted as prescribed by ASTM E345-81 for the testing of metallic foils in thicknesses of less than 0.150 mm (0.006 in). Type A specimens were used with a two inch gage length, and a nominal thickness of 0.0305 mm (0.0012 in). Load-displacement traces were recorded on a Linseis X-Y recorder and loading was conducted at 3 MPa/sec. The yield strength was determined by the 0.2% offset method from the resulting stress-strain curves. Representative stress-strain curves for the materials tested are shown in Figures 20 and 21, and the yield strengths, tensile strengths reduction in area, total elongation and true fracture strain are reported in Table 3.

3.2.2 Tension-Tension Fatigue Tests

The copper foils were tested in tension-tension fatigue on an Instron electrohydraulic closed loop test system. All tests were conducted under load control at a frequency of 20 Hz. The copper foils were tested at room temperature (approximately 70% relative humidity) and the test results are plotted in Figure 27.

3.2.3 Cyclic Strain Fatigue Tests

Specimen Development

One major aim of this research project was to develop a test methodology for the study of the cyclic strain fatigue properties of electroless copper. Information gathered from cyclic strain fatigue studies involving uniaxial, fully-reversed, strain controlled tests can be used to derive a relationship between total strain and life

similar to that of the Coffin-Manson Relationship. In such testing, a single fatigue cycle involves both tension and compression strain excursions of equal magnitude. The fact that the copper samples in this study take the form of 0.0305 mm thick foils, imposes significant experimental difficulties for cyclic strain fatigue testing since one must guard against the possibility of buckling. For this reason, reversed loading of the thin copper foils required the presence of some supporting substrate.

Several factors were considered in choosing the proper substrate material and are summarized as follows:

- substrate elongation
- electrical conductivity of the substrate
- acoustic properties (AE attenuation, AE event characteristics, etc.) of the substrate
- substrate similarity to PC board material
- copper/substrate plating compatibility
- mechanical surface properties of substrate

Since potential drop (ΔV) was to be monitored during the fatigue tests, for purposes of monitoring damage accumulation in the copper foil, the substrate choices were reduced to non-conductive materials (non-metallics); thus, polymer-type substrates were sought. The first substrates tested were Delrin and Nylon 6 with the copper being plated on the outside of round hour-glass shaped specimens. The mechanical properties of these substrate materials appeared adequate, except for the fact that the specimen geometry allowed for Poisson contractions so as to pull the substrate away from the copper plating. An analysis

of MIB geometry and its associated physical properties, reveals that when the MIB is thermally cycled, the Poisson contractions are small in directions within the plane of the board. From this analysis, it was seen that the PTH could be considered a cylindrical specimen for which the diameter could be approximated as the area under the surface lands (copper rounds plated on MIB surface). This analysis led to the development of the specimen shown in Figure 11. Note that the copper is plated on the specimen ends and on the surface of a hole drilled axially through the specimen center. The plating on the specimen ends has three important purposes: (1) it provides a site for acoustic coupling to the copper "barrel" during testing, (2) it provides a site for electrical coupling to the copper "barrel" during testing, and (3) it simulates the PTH external lands.

When the MIB is thermally cycled, stress is imparted to the PTH in the thickness direction by each of three means: (1) shear stresses between the substrate and copper, (2) tensile and bending stresses imparted by physical discontinuities at the copper/epoxy-glass interface, and (3) tensile and bending stresses from the PTH lands (both internal and external). The first two mechanisms for stress transmittal are very difficult to model and analyze. Therefore, it was desirable to match the specimen surface properties to the MIB matrix surface properties so as to eliminate this uncertainty. To this end, half inch diameter rods made of FR4 epoxy and chopped fiber glass were used as the substrate materials. These rods closely model the MIB matrix composition and morphology in that the fibers are largely oriented perpendicular to the rod length.

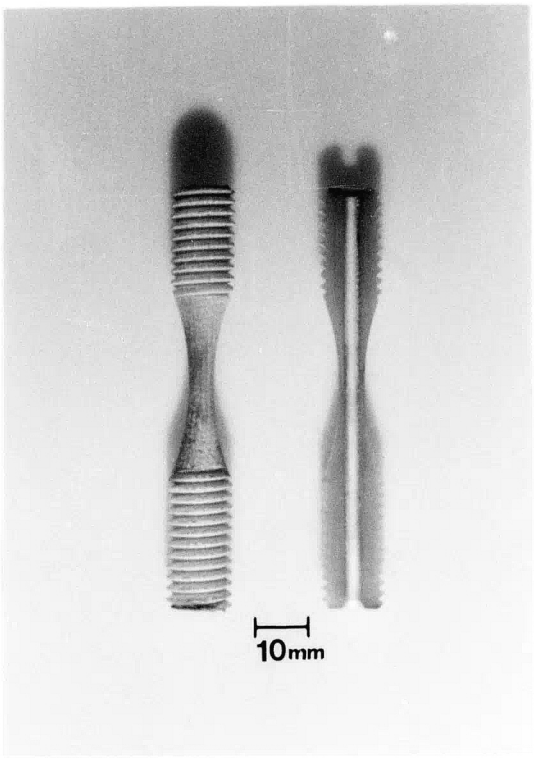

Figure 11: Strain cycle fatigue specimen with through hole and specimen ends having been plated with electroless Cu.

Test Variables

Several design and process variables used in the production of well-manufactured PTHs were investigated to assess their influence on cyclic fatigue lives. Fatigue specimens were produced to incorporate certain of these design and process variables with a control group being established to compare the relative influence of each variable. Table 1 contains the specimen preparations studied. An explanation of each variable studied follows:

Aspect Ratio (L/D): The ratio of the specimen gage length (L) to through hole diameter (D). The control aspect ratio was 10:1 and the variation was 6:1.

Surface Roughness: The finish on the through hole surface. The control finish was "as-drilled", with two variations, 6 μm and 1 μm polished surface being investigated.

Surface Activation: Prior to electroless plating the through hole was chemically treated to stimulate grain growth. The mechanism of this seeding operation is proprietory*; however, two types of seeding were investigated. The control seeding was termed "Activator 3" with the variation being referred to as "Activator 1".

Copper Quality: This refers to the type of copper plate. The control copper was uncontaminated electroless copper, with good ductility, while two variations, contaminated electroless copper (low ductility) and electroplated copper, were also produced.

*IBM Proprietary Information

Table 1

CSF Specimen Variables

Specimen Name	Aspect Ratio (L/D) 10:1	6:1	Surface Roughness As-drilled	6μm	1μm	Activation No. 3	No. 1	Copper Quality Uncontaminated (good ductility)	Contaminated (poor ductiility)
Control Group	X		X			X		X	
Aspect Ratio 6:1		X	X			X		X	
6 Micron	X			X		X		X	
1 Micron	X				X	X		X	
Activator #1	X		X				X	X	
"Contaminated" low ductility	X		X			X			X

Cyclic fatigue experiments were conducted on an Instron electro-hydraulic closed loop test system with each sample experiencing fully reversed loading. Strain control was monitored by a clip-in displacement gage which was mounted across the specimen gage section (Figure 12). All tests were performed at room temperature (approximately 70% relative humidity) and at a frequency of 0.35 Hz.

The strain in the specimen gage length was calibrated versus the clip-in gage for tensile and compressive loading by mounting a Micro-Measurements strain gage (Model #EA-09-125AD-120) at the gage center and loading the specimen in tension and compression. Clip-in gage and strain gage readings were recorded for several loading cycles and for several specimens. From Figure 13, it is seen that the clip-in gage strain was approximately an order of magnitude greater than the strain gage for the entire strain range (+/-). A finite element analysis was conducted on the cyclic strain fatigue specimen to establish a relationship between the average y-strain at the specimen mid-length for the outermost epoxy-glass element (A) and the copper element (B) shown in Figure 14. The same assumptions used for the PTH analysis are applicable; however, in the case of the fatigue sample thermal loading was replaced by a uniform stress applied at the specimen end. Copper barrel longitudinal strains were calculated using the strain calibration curve and the copper:epoxy-glass strain ratio from the FEA as follows:

$$\Delta\varepsilon_{copper} = \alpha\ \Delta\varepsilon_{sg} \tag{11}$$

Figure 12: Photograph showing cyclic strain fatigue set up.

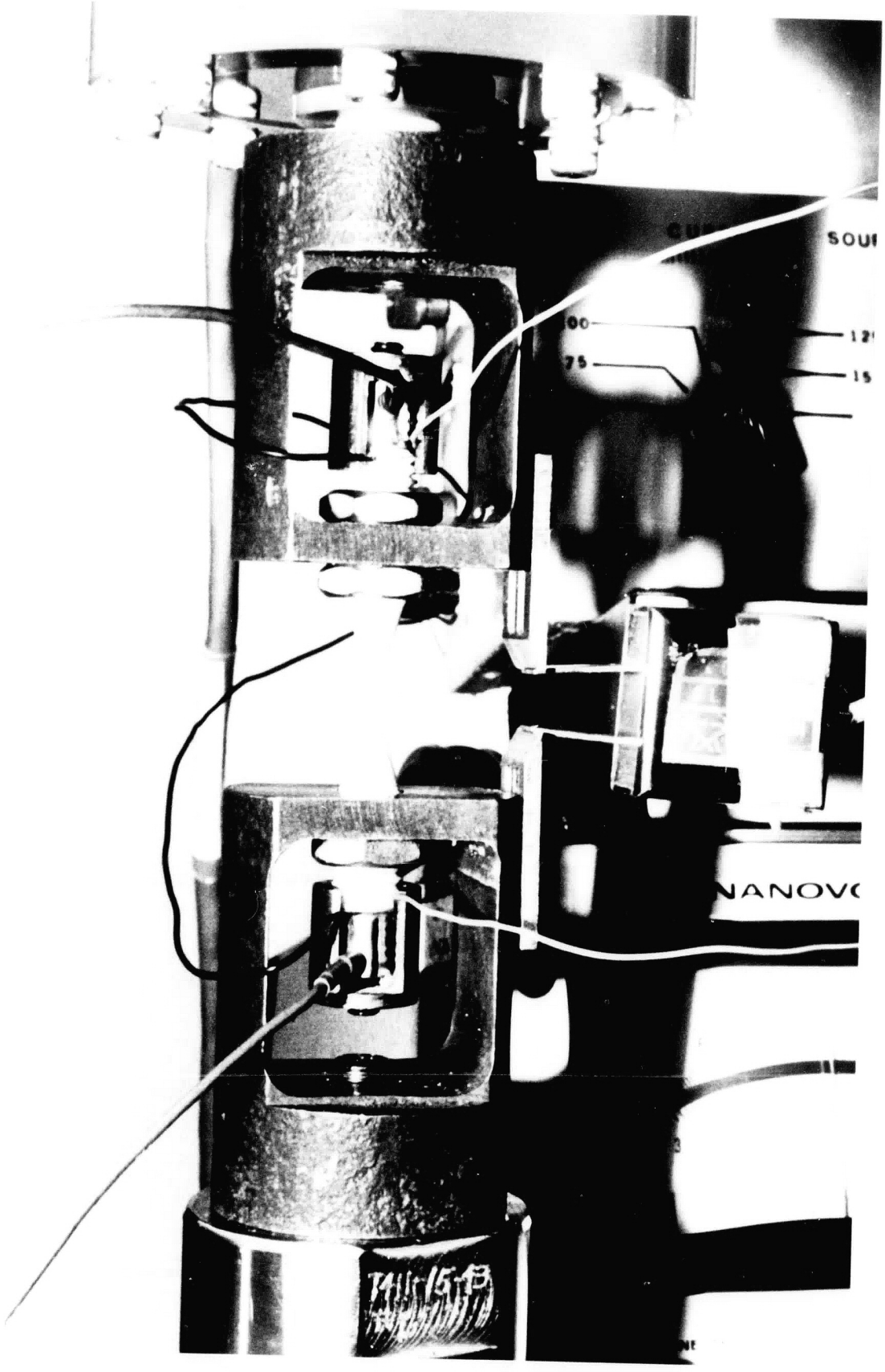
SOUI
NANOVO

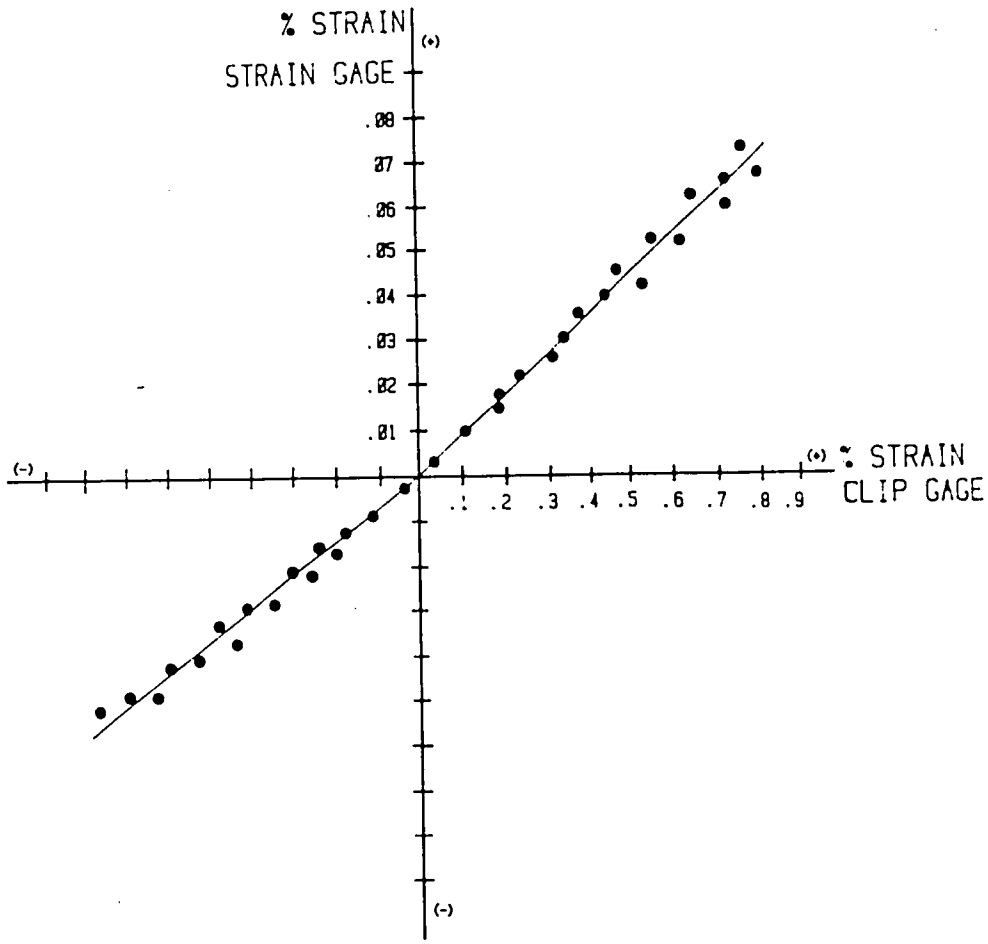

Figure 13: Calibration curve showing clip-in gage strain versus strain gage strain.

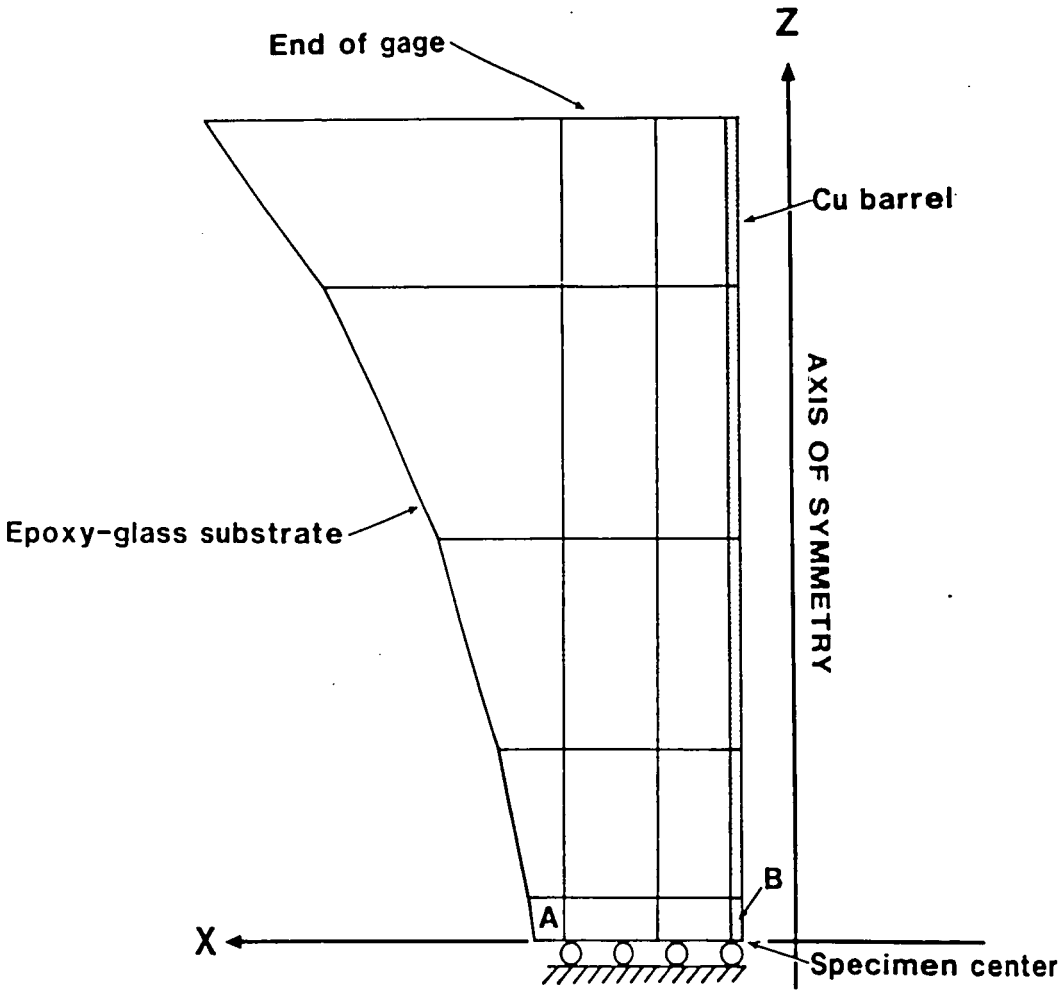

Figure 14: FEA specimen gage section used to determine average Y-strain relation between element A and element B.

where $\Delta\varepsilon_{copper}$ = nominal longitudinal copper strain, α = 0.5 from FEA and $\Delta\varepsilon_{sg}$ = strain gage strain.

Acoustic Emission Experiments

Acoustic emissions resulting from the fatigue tests were monitored with a Physical Acoustics Corporation (PAC) 3000/3004 Four Channel AE Analyzer. AE signals were detected with PAC μ30s transducers (resonant frequency of 300 kHz, signal to noise ratio of 23, and capacitance of 184 picofaraday), amplified 40dB by a PAC 1220A preamplifier and subsequently amplified 35dB by the 3004 analyzer. AE events were recorded with the PAC RT/DAS data acquisition software program and stored on floppy disks. Post analysis data discrimination was performed using the PAC RTPOST program and plotted using the PAC Superplot program.

From preliminary investigations aimed at identifying the different types of AE signals that one might expect to monitor during the fatigue tests, it was considered infeasible to characterize the numerous types of AE sources present. Therefore, acoustic emissions during the fatigue tests were recorded to compare the general trend from one test to another.

AE spectra for each of the tests were recorded with a total system gain of 75 dB and a threshold voltage of 0.1 volt giving an actual amplitude threshold of 45 dB. This threshold value eliminated all noise associated with the hydraulic system. The transducers were firmly attached to the ends of the specimen as shown in Figure 12. In order to ensure good acoustic coupling, a thin layer of Dow Corning High Vacuum grease was applied between the transducer and specimen

surface. Spectra for each test were plotted as AE events vs. event amplitude vs. cycles and are shown in Appendix 2.

Potential Drop Circuit

The extent of copper cracking was monitored during the fatigue tests by following the change in resistance of the copper plating as a function of loading cycles. A constant current source of 0.1 Ampere was applied across the specimen length, and the change in voltage across the specimen monitored on a Keithley Instruments 148 Nanovoltmeter. With a constant current applied to the specimen, a change in voltage can be directly converted into a change in resistance by Ohm's Law:

$$V = IR$$

Therefore,

$$\frac{\Delta V}{I} = \Delta R$$

In this investigation, four failure criteria were established:

(1) $\Delta V = 20\ \mu V \rightarrow \Delta R = 200\ \mu\Omega$

(2) $\Delta V = 50\ \mu V \rightarrow \Delta R = 500\ \mu\Omega$

(3) $\Delta V = 100\mu V \rightarrow \Delta R = 1000\mu\Omega$

(4) $\Delta V = 200\mu V \rightarrow \Delta R = 2000\mu\Omega$

During the tests, the voltage change was recorded at the fully unloaded portion of the cycle. This precludes resistance changes resulting from elastic straining and thus corresponds to changes in resistance associated with actual copper cracking and permanent plastic flow.

3.3 MICROSCOPY

3.3.1 Light Optical Microscopy

After the fatigue tests were conducted, the gage portion of the specimens were sectioned on a slow speed diamond saw, and the cross sections mounted in a standard cold mount. The mounts were then ground and polished to a 0.3 μm finish and examined on a Zeiss Inverted Light Microscope.

3.3.2 Scanning Electron Microscopy (SEM)

Scanning electron microscopy examinations were conducted on an ETEC Autoscan Scanning Electron Microscope operated at 20 kV. Stereomicroscopy was carried out using the technique described by Goldstein et al. [31] with 3D height measurements of the as-deposited surface roughness being calculated using the formula [32]:

$$Z_c = \frac{P}{M\ 2\sin(\alpha/2)} \tag{12}$$

Z_c is a height difference normal to a plane parallel with the half-way tilt position between left and right photos, M is the magnification, P is $x_L - x_R$ (where x_L and x_R are the distance between two points A and B in the left and right photos, respectively) and α is the difference in tilt angles.

3.3.3 Transmission Electron Microscopy (TEM)

Microstructural examination of electroless copper was carried out in the transmission electron microscope. Thin foils were prepared from 3 mm disks punched out of copper foils which were then mechanically thinned on 600 grit SiC paper to 40 μm. These disks were

ultrasonically cleaned in ethyl alcohol, and then jet-electropolished in a Struers Tenupol electropolishing unit. Electropolishing was carried out in a 66% phosphoric acid/water solution at 10°C with a polishing potential of 4 volts. The specimens were immediately cleaned in H_2O and rinsed in ethyl alcohol. Several specimens required ion-beam milling to produce sufficient thin area.

TEM examinations were conducted on a Philips 400T fitted with a LaB_6 electron source operated at an accelerating potential of 120kV. Both undeformed and deformed copper specimens were examined using the standard Philips single-tilt low background holder.

3.4 ANALYTICAL ELECTRON MICROSCOPY (AEM) AND DIFFRACTION ANALYSIS

Local chemistry of the grain boundaries in electroless copper was studied using the AEM through Energy Dispersive X-ray Spectroscopy (EDS) microanalysis. For the determination of qualitative levels of residual strain in the electroless copper, convergent beam electron diffraction (CBED) was used along with HOLZ Line position measurements.

3.4.1 EDS X-ray Microanalysis

The specimens for microanalysis were prepared by ion-beam thinning to avoid electropolishing effects which could interfere with the x-ray microanalysis [33]. The specimens were observed and x-ray spectra recorded with a Philips EM400T AEM equipped with an EDAX 20° take-off angle x-ray detector and a Tracor Northern 2000 multichannel analyzer. The specimens were held in a standard Philips double-tilt, low background specimen holder; analyses were conducted on grain boundaries which were tilted to be parallel to the electron beam. The direction of tilt was always toward the x-ray detector and the tilt angle never exceeded 15° in order to minimize any spurious x-ray signals. The electron beam was positioned on the grain boundary of interest and x-ray data collected for 300 seconds using a spot size of 5 nm and a 50 μm thick C_2 aperture. Since the purpose of this analysis was to merely assess whether any grain boundary contaminants were present in the electroless copper, no attempt was made to quantify the levels of any species found as has been done for bismuth segregation in copper [16,17]. When coherent bremsstrahlung (CB)[34] peaks were observed in the x-ray spectra, careful tilting of the

specimen was required in order to minimize the effects of CB before further microanalysis could be conducted.

3.4.2 Evaluation of Residual Strain Through Higher Order Laue Zone (HOLZ) Line Analysis

HOLZ line positions may be used to determine the lattice parameter to an accuracy of two parts in 10,000 (recall Section 2.3.2) Others [26,28,35,36] have shown that <111> zone axis CBED patterns are well suited for lattice parameter determination and are very sensitive to strain measurements in FCC materials due to the high symmetry of the HOLZ lines. The plated-through-hole specimen for CBED analysis was prepared by careful sectioning of the MIB and ion-beam thinning as shown in Figure 15.

CBED Analysis

The general procedure for producing the CBED patterns used in this study have been outlined by Williams [37]. The STEM mode technique was used for establishing the zone axis pattern (ZAP) of interest with the spot size being set to provide a focussed 40 nm probe at the specimen surface and a stationary beam placed on the area of interest. When the STEM detector was removed, the entire CBED pattern was observed at a camera length (CL) of 575 mm, while a CL of 1150 mm was used for viewing the HOLZ lines in the direct disk (transmitted beam). A 50 μm C_2 aperture was used to provide adequate convergence to obtain good HOLZ line patterns, while a 10 μm C_2 aperture was used to produce a low magnification CBED pattern with adequate spot separation for easy indexing. The CBED patterns were indexed as described by Williams [38].

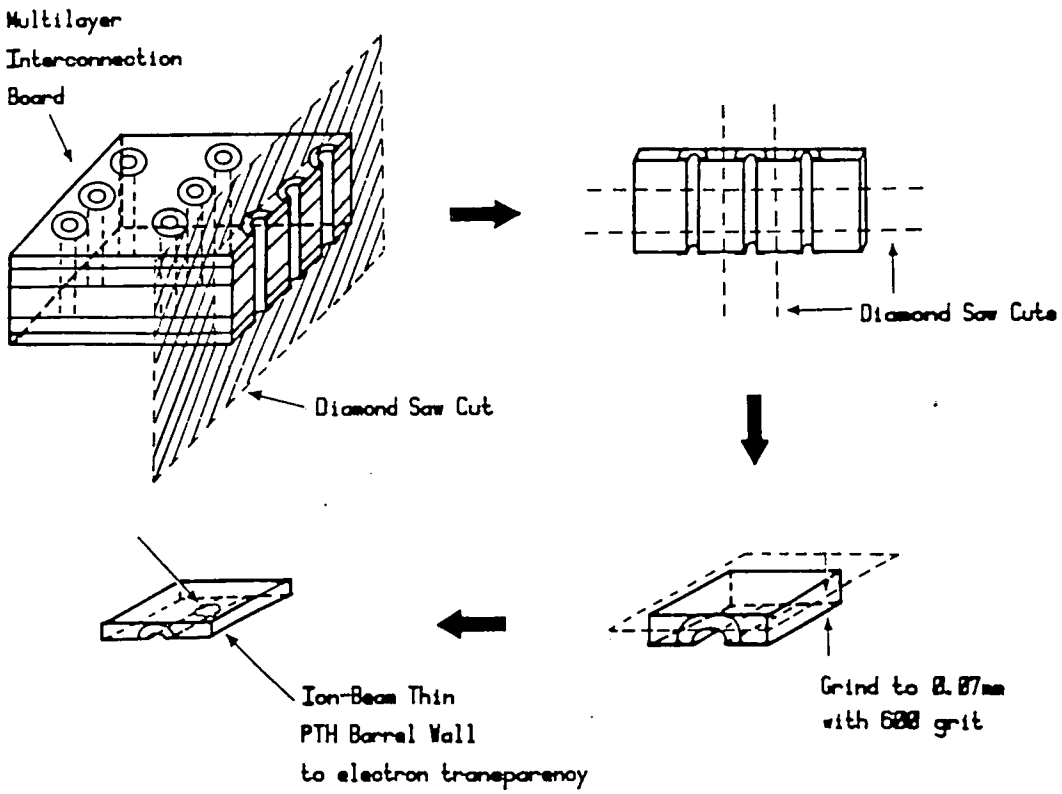

Figure 15: Schematic diagram showing MIB sectioning procedure to remove a PTH section for CBED analysis.

Simulation of HOLZ Line Patterns

The techniques for simulating the HOLZ line patterns in the direct disk of the CBED patterns have been described in depth by Ecob et al. [26] and thus only the necessary information with regard to this study will be discussed here.

The simulation procedure requires accurate indexing of the HOLZ lines in the CBED pattern. A computer program, which uses such information as the crystal structure, lattice parameter, electron wavelength, zone axis and geometrical considerations, calculates the positions of the HOLZ Lines in the direct disk and then transmits the results to a pen plotter.

Dispersion effects may create changes in the "effective" electron wavelength. Since the simulation technique does not take into account these effects, some type of calibration is necessary. For this calibration, well annealed pure copper sample <111> ZAP CBED patterns were obtained using the conditions described earlier. Simulations were carried out to determine the best agreement using a series of different wavelengths. Once the "effective" wavelength for the <111> direction was known, simulations using this wavelength could be conducted to match experimental HOLZ line patterns by varying the lattice parameter.

When the lattice parameter and/or the tetragonality of the pattern was different from the "standard", strain was considered to exist. Experimental HOLZ line patterns were obtained for various strain magnitudes by removing specimens from copper foils that had been strained in uniaxial tension to a known nominal elongation. CBED

patterns for at least 8-10 grains were recorded for each analysis; the most prevalent patterns were then simulated to infer lattice strain.

3.4.3 Auger Electron Spectroscopy (AES)

The elemental chemistry of copper foil fracture surfaces was determined using a Physical Electronics Auger Spectrometer. Auger spectroscopy was performed on both the uncontaminated (good ductility) and contaminated (low ductility) copper used in this study, and spectra were recorded at an accelerating potential of 5 kV and a voltage modulation of 3 eV. Specimens for analysis were ultrasonically cleaned in tricholoethylene, followed by ethyl alcohol. Due to the poor rigidity of foil specimens, in-situ fracturing was not possible; therefore, specimens were fractured in air and immediately placed into the Auger unit. Although surface oxidation and atmospheric contamination could not be completely avoided, all other contamination was minimized.

IV. RESULTS AND DISCUSSION

4.1 STRESS ANALYSES

Oien's analytical model [3] for understanding the thermomechanical deformation of the PTH structure represents a fairly simplistic approach which does not take into account the geometric effects of the actual PTH structure. Due to the simplicity of Oien's model it was considered important to develop a more accurate PTH model and stress-strain analysis for assessing the thermomechanical deformation of the PTH. To this end, an analytical model of the PTH structure including an external land was developed. The analytical model assumes a uniform stress-strain distribution across the PTH barrel which does not actually exist in the PTH due to (1) asymmetric loading, (2) stress concentrations along the PTH wall, and (3) local variations in copper ductility.

Finite element analysis (FEA) of the PTH structure was also conducted to provide information as to the stress-strain distributions within the copper barrel. The FEA allows for asymmetric loading of the PTH idealization as experienced by the actual PTH which results in variations of the stress-strain distribution within the copper barrel.

Neither the analytical or FEA models take into consideration the relatively rough PTH surface which acts to locally amplify stresses and strains. Furthermore, neither approach accounts for local variations in the copper ductility which act to locally amplify stresses. As a result of these two limitations, even with the improvements in the model and analyses, the results may underestimate the stresses and strains most important in assessing cracking

probability (i.e. local stresses and strains). However, both analyses assume that for $\Delta T = 0$ the stresses and strains are both zero. This assumption is probably invalid since during the initial through hole plating, the MIB is submerged in the plating bath held at a constant 73°C. After plating the through holes, the board is cooled to room temperature. Due to the thermal expansion coefficient mismatch, the PTH barrel experiences a state of residual compressive stress For this case, $\Delta T = -52°C$, assuming that room temperature is approximately 21°C. As a result, only temperature changes greater than 52°C should introduce tensile stresses into the barrel. The actual PTH barrel, however, is relatively rough which creates shear stresses in the barrel which are not accounted for. In either case, the time zero stress state is assumed to be zero for both analyses. The residual compressive stress state will be considered in further detail later. It should be noted here though that since the models ignore stress concentrations, the actual local strains are underestimated. On the other hand, the assumption of a zero strain at time zero overestimates the actual strains in the PTH since the beneficial influence of the residual compressive stress is not considered. Thus, the two simplifications noted above introduce errors that are at least partially offsetting.

4.1.1 Analytical Model

The basis for developing the analytical model of the PTH was to establish a relationship between nominal stresses and strains and a temperature change introduced into the MIB. The analytical model was designed to incorporate the geometrical effects of an external land.

The relationship for the average elastic stress in the PTH barrel is given by

$$\sigma_b = Y_b \frac{(\alpha_M - \alpha_b) \cdot \Delta T}{1+2\,\frac{Y_b\,A_b}{Y_M\,A_M}} \tag{8}$$

and the total average barrel strain is given by

$$\varepsilon_b = \frac{(\alpha_M - \alpha_b)\ \Delta T}{1+2\,\frac{Y_b\,A_b}{Y_M\,A_M}} + \alpha_b \Delta T \tag{9}$$

The values for the various material properties are given in Table 2.

Before discussing the numerical results obtained for equation (8), the validity of the equations will be assessed by examining the boundary limits to the equations. This will be done for the stress equation but the results can be interpreted for the strain equation by simple analogy.

1. As $\Delta T \to 0$ the stress $\sigma_b \to 0$. This follows directly from the analysis.

2. As $\alpha_M \to \alpha_b$ the stress $\sigma_b \to 0$. This is valid since if there is no thermal expansion coefficient mismatch no stresses should be introduced (i.e. free thermal expansion).

3. $Y_M A_M >> Y_b A_b$ (i.e. the stiffer matrix forces the copper barrel to take up the full matrix strain) then $\sigma_b = Y_b\ (\alpha_M - \alpha_b)\ \Delta T$

Table 2

Material Properties

	Poisson's Ratio		Elastic Modulus				Thermal Expansion Coefficient $(x10^{-6})°C^{-1}$			
	YX	XY	EY	EX	EZ	GXY	X	Y	Z	
Copper	.343	.343	129.8	129.8	129.8	48.3	16.6	16.6	16.6	
Epoxy-Glass	.0964	.0657	4.8	6.9	3.4	0.62	21.3	19.8	86.5	(40-90°C)
							18.0	16.8	60.2	(30-40°C)
							17.5	14.7	42.6	(18-30°C)

since $Y_b A_b / Y_M A_M \to 0$. This seems to be valid since it would be expected that the barrel strain should become the same as the matrix strain.

4. $Y_b A_b >> Y_M A_M$ (i.e. the stiffer barrel forces the matrix to take up the expanded barrel dimensions), therefore $Y_b A_b / Y_M A_M \to \infty$ resulting in:

$$\sigma_b \to \frac{Y_M A_M}{2 A} (\alpha_M - \alpha_b) \cdot \Delta T \qquad (13)$$

This result seems questionable since you would expect $\sigma_b \to 0$ (i.e. to take up its fully expanded length). On closer inspection, it appears that this result may be an artifact due to the assumption that the matrix strain increases linearly from the barrel strain along the barrel wall to $\alpha_m \cdot \Delta T$ at the end of the land. Consequently, however high the barrel stiffness becomes, the matrix strain is $\frac{\alpha_M - \alpha_b}{2} \Delta T$ with the elastic component averaging $\frac{\alpha_M - \alpha_b}{2} \Delta T$. This results in a force of $Y_M A_M \frac{\alpha_M - \alpha_b}{2} \Delta T$ on the barrel Mand an elastic stress of $\sigma = \frac{Y_M A_M}{2 A_b} (\alpha_M - \alpha_b) \Delta T$ as found earlier.

The barrel stiffness, however, is only ∿3 times greater than the matrix stiffness. Therefore, the elastic barrel stress may be given by equation (8) and the total barrel strain by equation (10).

Figure 16 presents a plot of the PTH barrel strain versus temperature change as computed from equation 10. Included in Figure 16 are curves representing the free thermal expansion of the PTH copper and the epoxy-glass matrix. The elastic strain component for the PTH copper may be computed by subtracting the free thermal expansion of

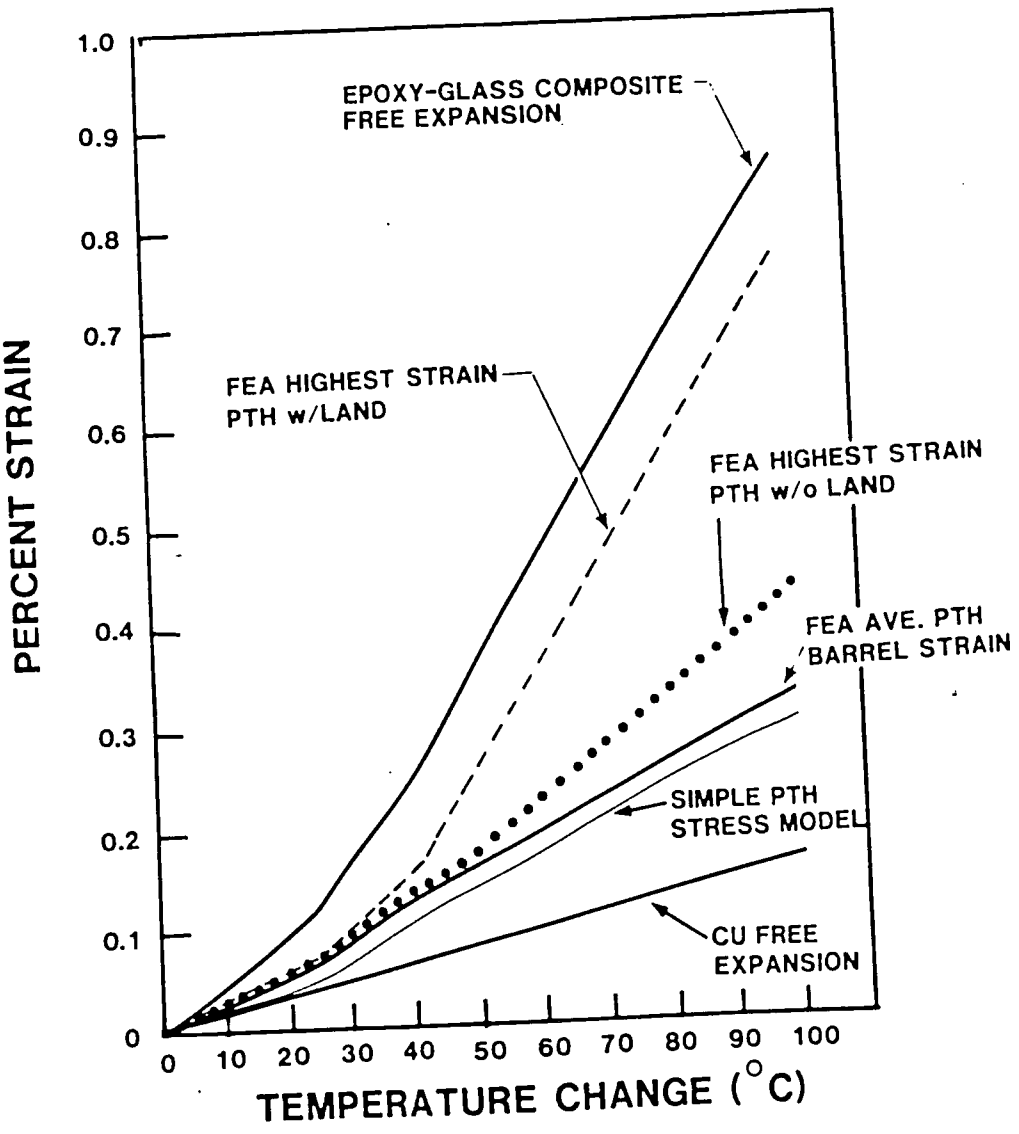

Figure 16: Plot of PTH barrel strain versus temperature change.

the copper from the curve for the PTH model. The general shape of the PTH model strain curve is governed by the differential rate of expansion of the epoxy-glass matrix. Even for temperatures well below the glass transition temperature of the epoxy, the thermal expansion coefficient changes with temperature. Once again it should be pointed out that the analysis is performed based on linear material response. If any plastic deformation of the PTH copper were to occur, the effective stiffness of the copper barrel to resist further deformation would be significantly reduced, thereby resulting in larger PTH copper strains.

By comparison of equation 10 to Oien's strain equation (1), it can be seen that Oien's model overestimates nominal strains by ∿1.7 times those computed by the presented analytical model. This result seems reasonable since the current model allows for the rotation of the surface land which effectively relieves some of the barrel strain. This result is important because significantly lower strains are predicted from this analytical model compared to Oien's model which should result in reasonable improvement in predicted reliability.

4.1.2 Finite Element Analyses

Two finite element idealizations were developed for a typical PTH such as in Figure 2. The idealizations model the PTH structure from the MIB centerline to one MIB surface. Idealization 1 (Figure 9) takes into account one external land but no internal lands; idealization 2 (Figure 10) takes into consideration the addition of one internal land. The axis of symmetry for the idealizations is located at the center of the PTH as shown in Figures 9 and 10. Due to

the geometric symmetry of the PTH structure and the incorporation of thermal loading, the finite element program APES was used throughout the entire analysis. APES is well-suited for the analysis of two-dimensional axisymmetric models for which linear elastic assumption are necessary. One limitation of APES is that isotropic thermal expansion coefficients must be used for thermal loading analysis. Because of the greater thermal expansion of the epoxy-glass in the through-thickness direction (Z-direction) of the MIB, the Z-direction thermal expansion coefficient was considered most significant and was employed throughout the analysis. However, since APES is a two-dimensional program, the through-thickness direction (Z) corresponds to the Y-direction analysis results. The stress and strain distributions were calculated in 10°C temperature increments from 0°C to 100°C. The maximum tensile stress for both idealizations was located at the MIB centerline along the PTH inside diameter. For PTH idealization 1, the maximum tensile stress is approximately 15 MPa for the first 10°C temperature change from room temperature , 21 MPa for each 10°C from ΔT = 10°C to ΔT = 30°C and 29 MPa for each 10°C from ΔT = 30° to ΔT = 100°C. For PTH idealization 2, the maximum tensile stresses are 30 MPa, 42 MPa and 58 MPa per 10°C for each temperature interval. A series of stress distributions for each idealization and at several ΔTs are given in Appendix 1.

Figure 16 reveals the FEA results for both idealizations along with the previously reported results of the analytical model. The first curve to discuss is labeled "FEA Ave. PTH Barrel Strain" which is the curve of the Y-direction copper barrel strains averaged over

the barrel length. The averaged strains from both idealizations fall on one curve and suggest that some regions of the copper barrel are subjected to lower stresses when an internal land is incorporated into the structure; in this case, the maximum tensile stress at the MIB centerline is twice as great as in idealization 2. From the FEA stress results it was determined that the barrel region just below the internal land junction goes into compression along the inside diameter of the PTH. This is the consequence of the bending moment on the internal land which is imposed by the epoxy-glass expansion in the region below the land. The deflected structure diagrams for idealization 2 (Figure 17) shows the effect of the deflected internal land on the PTH barrel; by comparison with Figure 18 (the deflected structure for idealization 1), the deflection introduced by the internal land can be seen clearly.

The FEA curve for the average Y-direction barrel strain lies $\sim$0.02% strain above that obtained from the analytical model. The slightly smaller strains from the analytical approach are primarily the consequence of the limitations in the analytical model to accurately describe the displacements of the PTH barrel-land structure.

Since the average Y-direction barrel strains from the two idealizations are approximately the same, and recognizing that the maximum tensile stress for idealization 2 is a factor of two greater than idealization 1, the maximum Y-direction strain in the PTH barrel was considered more important for the purpose of predicting barrel damage. Once again, the maximum tensile stress and strain of the

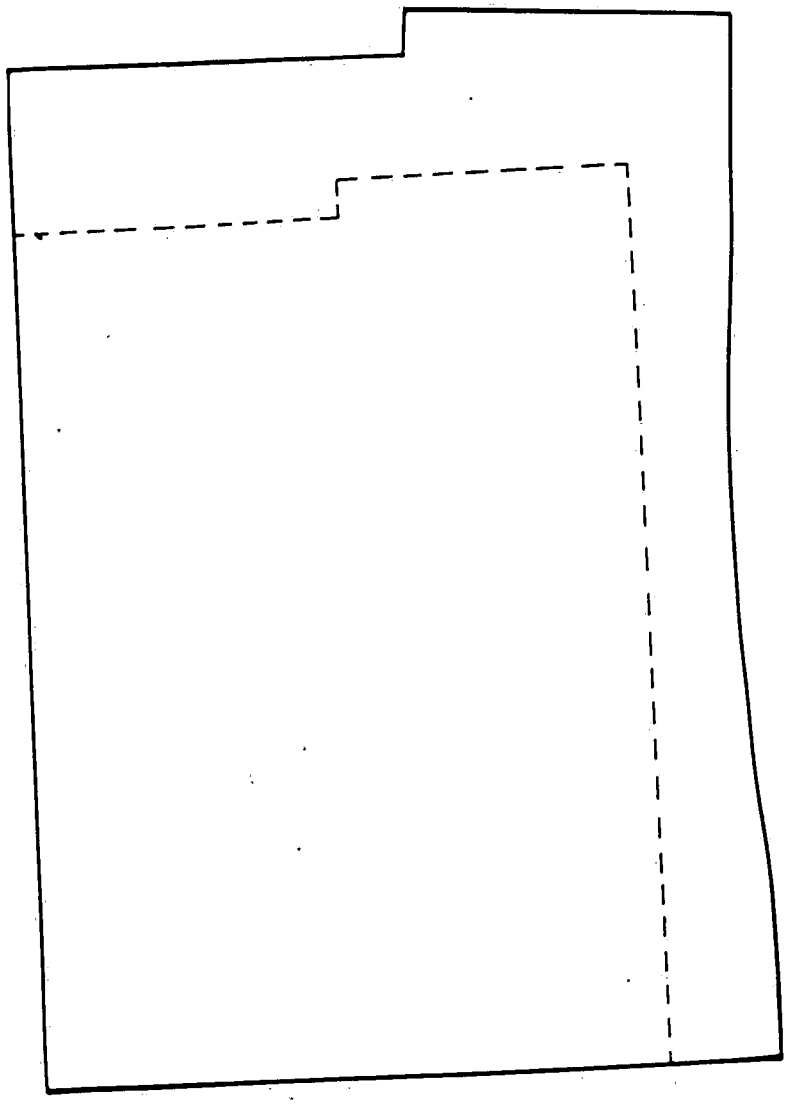

Figure 17: Deflected structure for idealization 2.

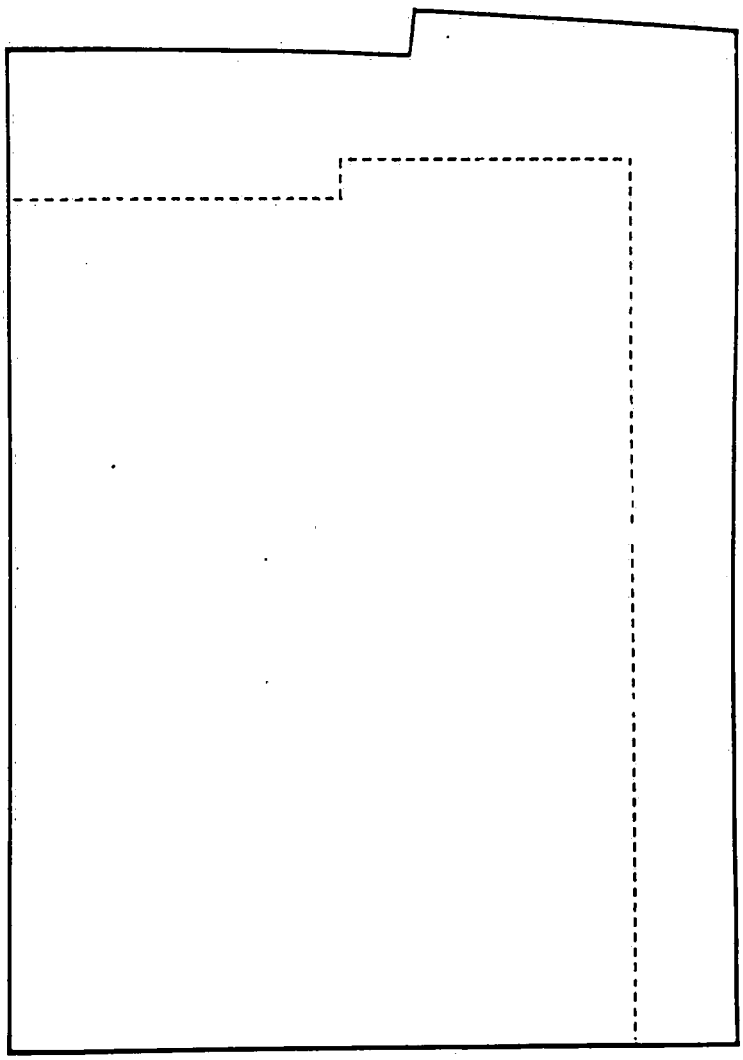

Figure 18: Deflection structure for idealization 1.

barrel is located along the inside diameter at the MIB centerline. The highest strain from idealization 1 (curve labeled "PTH w/o Land") and the highest strain from idealization 2 (curve labeled "PTH w/Land") are also plotted in Figure 16. For both idealizations, these curves are significantly higher than the average barrel strains. It should be noted that for the case when an internal land is incorporated (idealization 2), the highest barrel strain increases at about the same rate as the free expansion of the epoxy-glass composite, although the actual strain lags slightly behind the free expansion of the barrel.

The finite element technique also allows for easy determination of the initial PTH barrel stress distribution as a result of the plating process. The plating bath temperature is 73°C. Therefore, a MIB PTH plated at this temperature would develop residual compressive stresses upon cooling to room temperature (21°C), (i.e. for a ΔT = -52°C). Thus, the initial stress state of the PTH structure is assumed to be determinable from FEA by introducing a temperature change of -52°C. For idealization 1, the maximum compressive stress is $\sim$154 MPa and the average compressive stress is $\sim$70 MPa. For idealization 2, the maximum compressive stress is $\sim$320MPa and the average compressive stress is $\sim$144 MPa.

Although the actual compressive stresses are likely to be only a fraction of these calculated stresses, they represent a significant portion of the ultimate tensile strength of the electroless copper, (see section 4.2.1). This analysis suggests that temperature changes

greater than 52°C would be required in order to introduce tensile stresses which can contribute to PTH failure.

The finite element technique is also very useful for determining the effect of delamination along the copper/epoxy-glass interface on the PTH barrel stress distribution. From the stress contour plots in Appendix 1, it can be seen that a large stress gradient exists at the interface between the PTH copper barrel and the epoxy-glass matrix. This large stress gradient has a significant influence on the adhesion along the copper/epoxy-glass interface in an actual PTH. Large stress gradients were observed for both X and Y(Z) directions which would tend to delaminate the interface. The effect of a interfacial delamination on the stress distribution was investigated by introducing a region of delamination along the interface by breaking nodal continuity along an element adjacent to the interface (Figure 19). The delamination resulted in a 30% increase in the PTH barrel stresses along the delaminated region as compared to an undelaminated interface. Thus, interfacial delamination should significantly reduce the life of a PTH structure.

Having gained insight into the nature of the thermal response of a PTH structure based on a simple analytical model as well as finite element models, attention is now given to an evaluation of the tensile and fatigue test results.

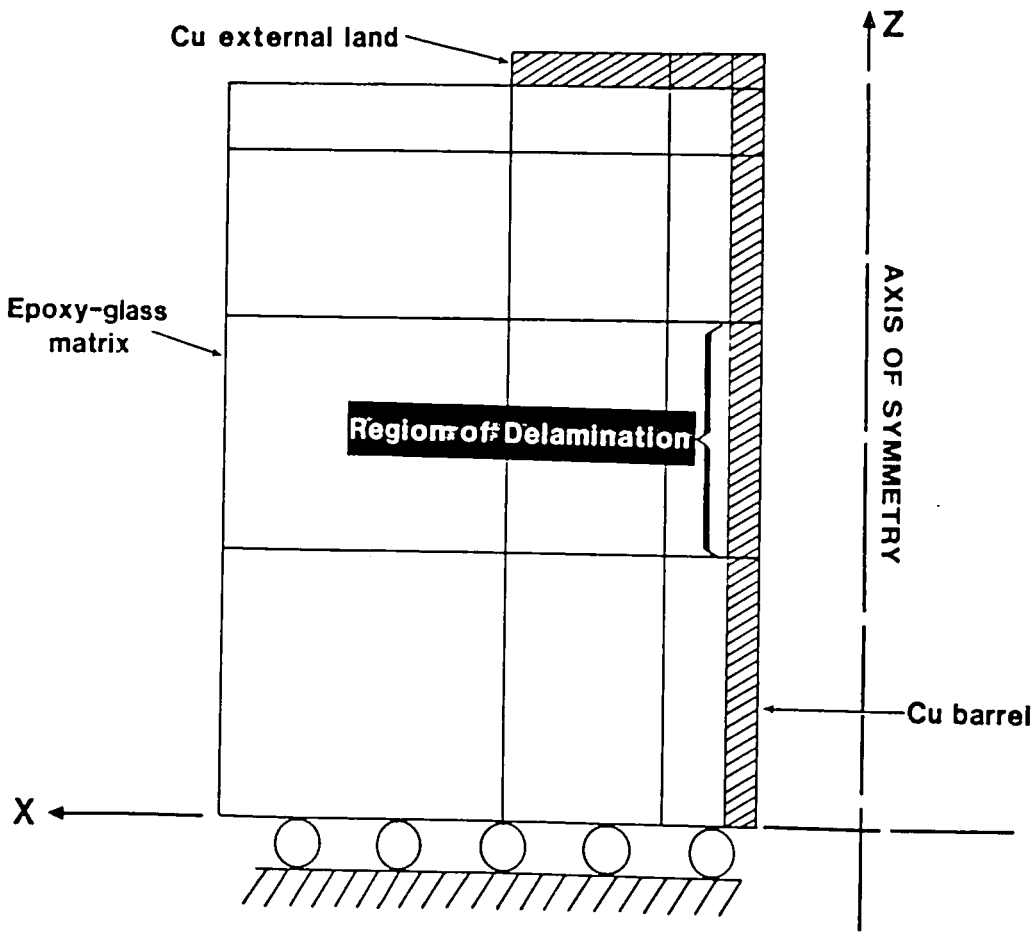

Figure 19: FEA PTH Idealization 1 with a region of delamination introduced along the copper/epoxy-glass interface.

4.2 TENSILE AND FATIGUE EXPERIMENTS

4.2.1 Monotonic Tests

Tensile tests were conducted on three foil preparations. Tensile stress-strain curves are shown in Figure 20 for tensile foils of "good quality" electroless copper that were prepared from two different plating baths. Tensile foils were also prepared from a plating bath with contaminants intentionally added to produce copper foils of lower ductility; the stress-strain curves for these foils appear in Figure 21. The microstructures of the uncontaminated and contaminated bath foils are shown in Figures 22 and 23, respectively. The tensile results for the three specimen groups are summarized in Table 3. It is seen that a large difference in tensile properties exists from one plating bath to another, and that in all cases the contaminated bath foils possessed lower ductility based on elongation to failure measurements. The lower ductility of the contaminated bath foils is due to the large concentration of point defects present in the microstructure, Figure 23, as compared to that of the uncontaminated bath foils.

Calculating ductility from elongation to failure data, however, may not be a good measure of local ductility since some necking may occur prior to failure. A better indication of localized ductility is reduction in area at fracture. For the thin foils, the area of the fracture surface was determined by measuring the width of the fracture surface from scanning electron micrographs. Figures 24-26 reveal the fracture surfaces of tensile foils prepared from the uncontaminated baths A and B and the contaminated bath, respectively. The drawn

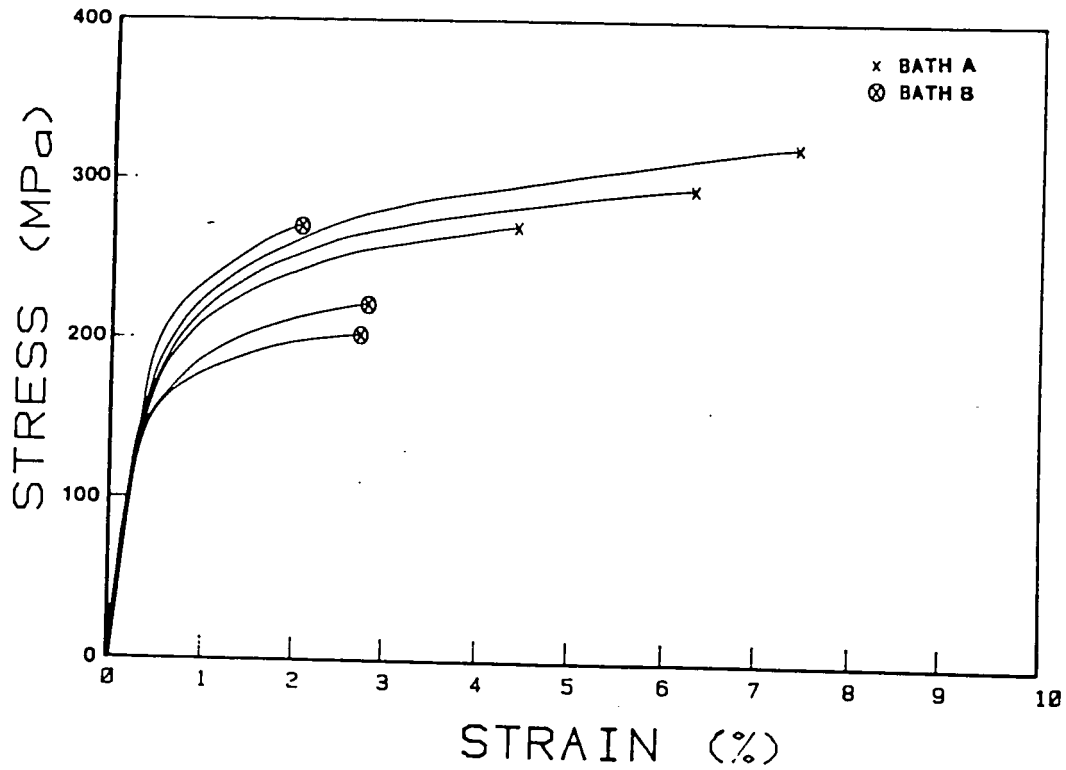

Figure 20: Stress-strain curves for "good quality" electroless copper foils.

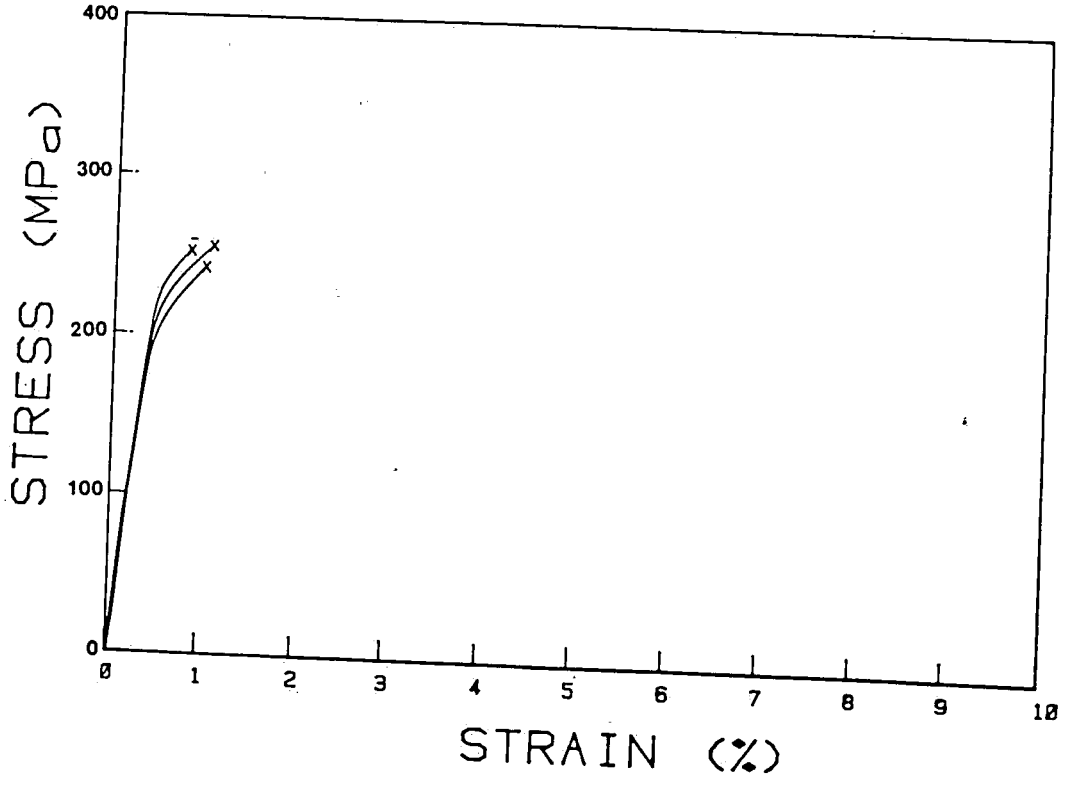

Figure 21: Stress-strain curves for contaminated, "low ductility" electroless copper foils.

Table 3

Electroless Copper Tensile Properties

Copper Quality	Specimen Number	0.2% Yield Strength (MPa)	Ultimate Tensile Strength (MPa)	Percent Reduction in Area	Percent Elongation (in 50 mm)	True Fracture Strain
Uncontaminated (Bath A)	1	176.0	260.0	58.2	4.3	0.87
	2	180.0	284.0	58.8	6.3	0.89
	3	192.0	316.0	59.6	7.5	0.91
Uncontaminated (Bath B)	1	156.0	200.0	53.2	2.7	0.76
	2	158.0	220.0	54.4	2.8	0.78
	3	212.0	272.0	52.7	2.1	0.75
Contaminated	1	224.0	242.0	46.0	1.1	0.62
	2	242.0	256.0	46.2	1.15	0.62
	3	248.0	250.0	45.6	0.85	0.61

Figure 22: TEM micrograph of as-received "good quality" electroless copper.

Figure 23: TEM micrograph of as-received contaminated "low ductility" electroless copper.

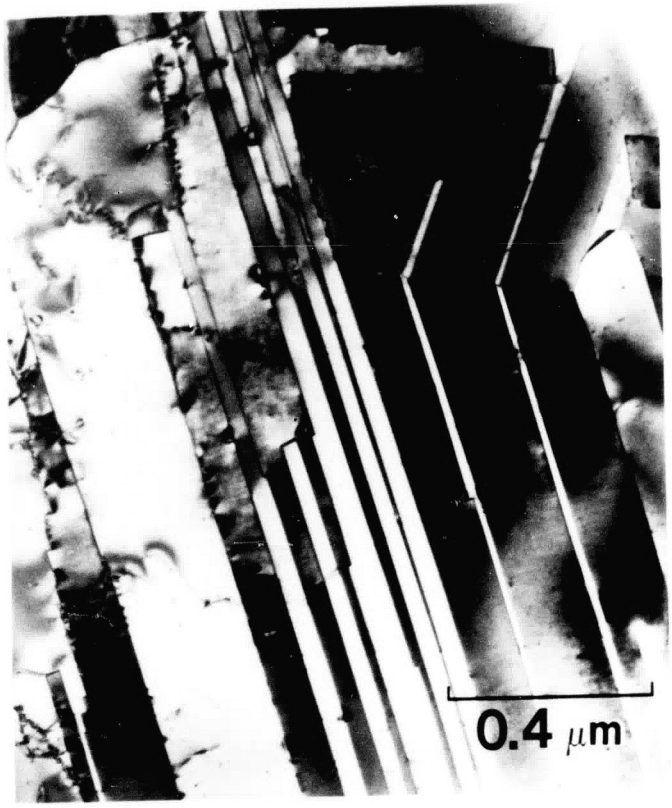
0.4 μm

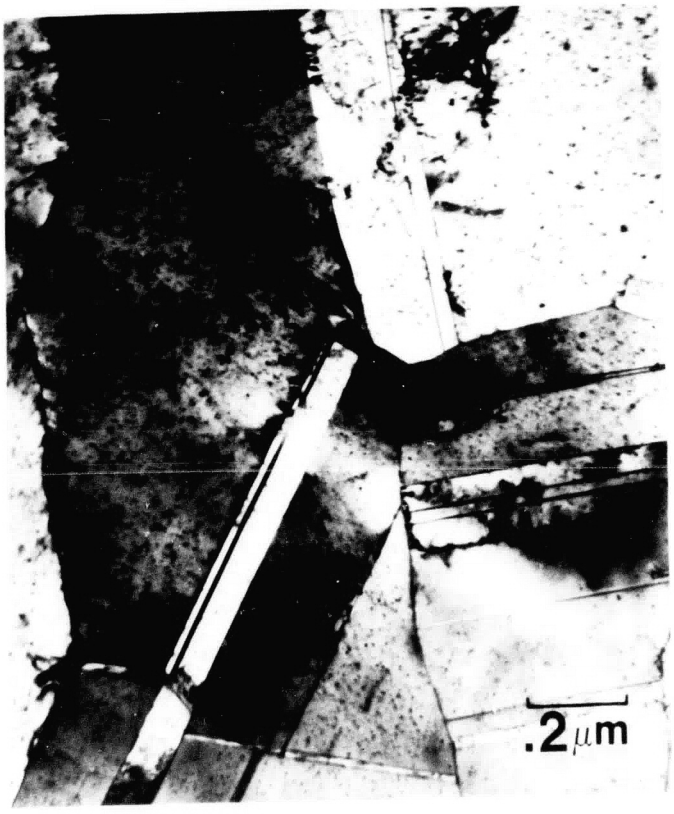
.2μm

Figure 24: SEM micrograph of the fracture surface of uncontaminated Bath A electroless copper foils.

Figure 25: SEM micrograph of the fracture surface of uncontaminated Bath B electroless copper foils.

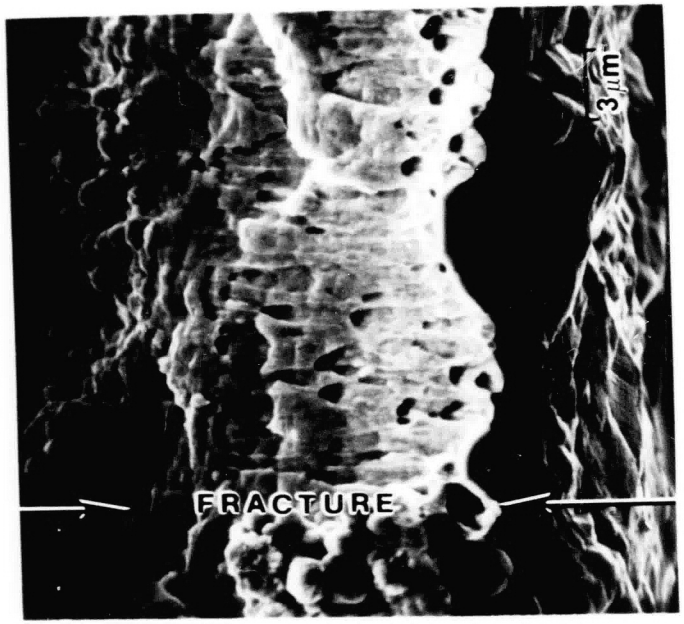
3 μm
FRACTURE

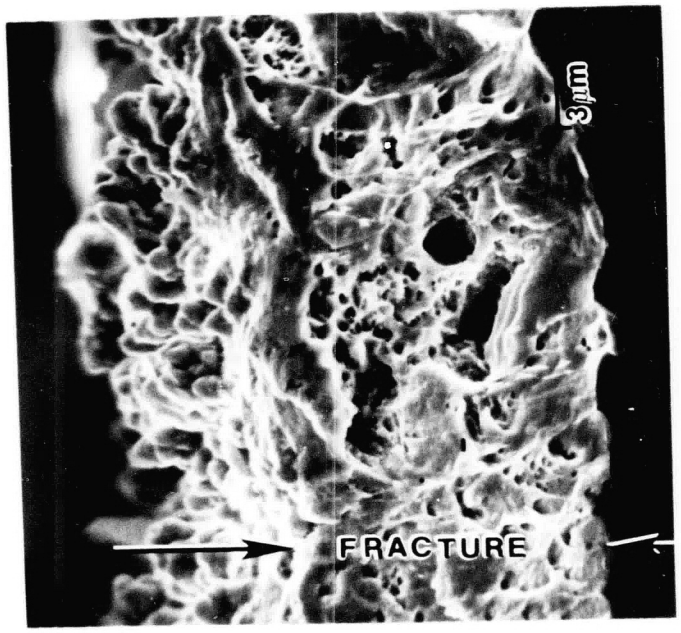
3 μm
FRACTURE

Figure 26: SEM micrograph of the fracture surface of contaminated electroless copper foils.

Fracture
4 μm

appearance of the fracture away from this rough deposit surface suggests that the surface roughness acts as stress concentrations which causes localized straining, and the fractures initiate at the surface from which the deposit grows. Once localized straining occurs, the remaining gage length is essentially stress relieved resulting in low elongations to failure, and high reductions in area. It follows then that if the ratio of surface roughness to foil thickness is reduced, elongation to failure should increase. Further discussion of surface roughness and microstructural effects on foil ductility will be presented in Section 4.3.

4.2.2 Tension-Tension Fatigue

Fatigue tests were performed on "good quality" electroless copper by cycling tensile foils under load control at a load ratio of $P_{min}/P_{max} = 0.1$. The results of these tests are plotted in Figure 27 with cycles to failure being plotted as a function of the stress range to tensile strength ratio. These results indicate that for tension-tension fatigue, electroless copper has good resistance to fatigue damage, particularly at stress ranges less than 50% of the tensile strength.

The fracture surfaces of the fatigue foils were examined in the scanning electron microscope in order to characterize the crack growth morphology. Figures 28a and 28b are micrographs of the fracture surface of a foil tested at a stress range ~80% of the tensile strength. The micrographs show fatigue striations eminating from the initial surface of deposition. From striation spacing measurements, the fatigue crack growth rate in this region is approximately 1×10^{-7}

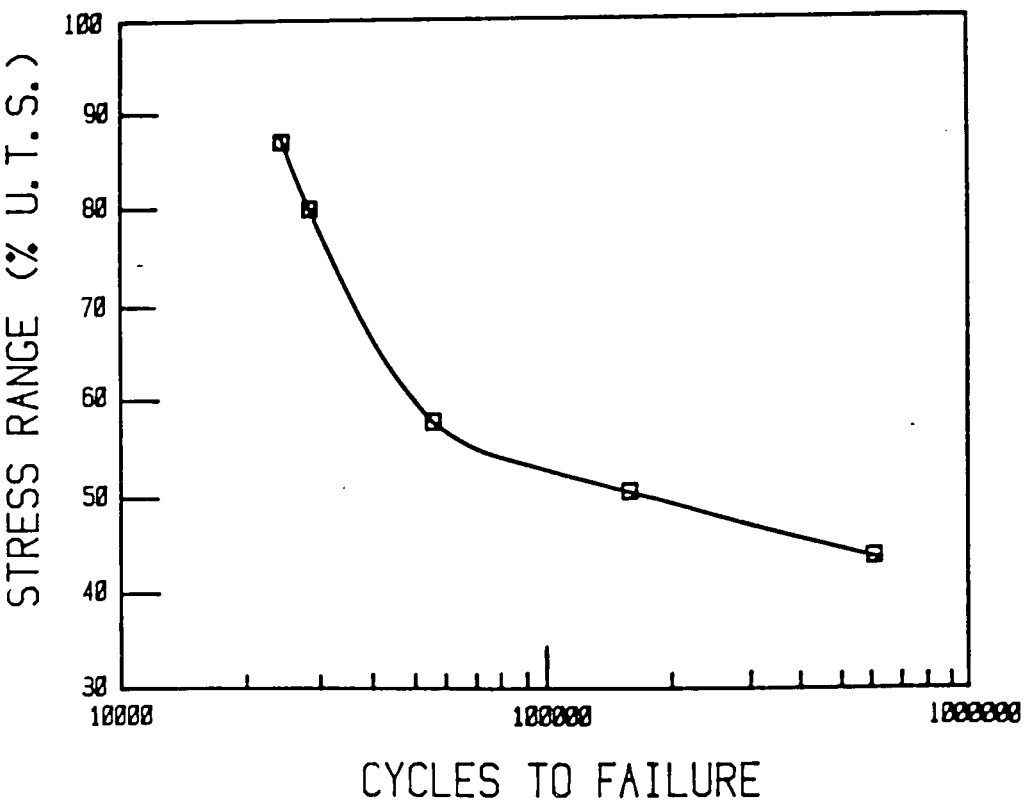

Figure 27: Plot of tension-tension fatigue and results for "good quality" electroless copper.

Figure 28a,b: SEM micrographs of fracture surface of electroless copper foil tested in tension-tension fatigue at ~80% of its tensile strength. Note fatigue striations oriented normal to the direction of crack propagation (arrow).

a

b

m/cycle. From the Bates and Clark [39] empirical correlation relating striation spacing to the stress intensity factor range,

$$\text{striation spacing} \sim 6 \left(\frac{\Delta K}{E}\right)^2 \tag{14}$$

where ΔK = stress intensity factor range

E = modulus of elasticity.

the stress intensity factor range was calculated to be $\sim$20 MPa$\sqrt{m}$. Figure 29 shows another region where the striation spacing was measured to be approximately 7×10^{-7} m/cycle. In this regime, the Bates and Clark correlation yields $\Delta K \sim 40$ MPa$\sqrt{m}$. Both of these results agree well with the fatigue crack growth rate data of Speidel [40] for commercial copper alloys. The results from both the monotonic and cyclic tests of the "good quality" electroless copper foils indicate that if elongation to failure data is excluded, the mechanical properties are similar to those of electroplated and wrought copper. For the contaminated copper deposits, the lower ductility and higher yield strength are primarily due to the high concentration of point defects in the microstructure. Further discussion of foil ductility and of microstructural changes due to fatigue deformation will be given in Section 4.3.

4.2.3 Cyclic Strain Fatigue (CSF) Experiments

CSF Specimen Development and Analysis

Of particular interest to this research project was the evaluation of the long term thermal cyclic life of electroless copper in MIB-PTH applications. In order to evaluate the cyclic life of

Figure 29: SEM micrographs of fracture surface of electroless copper foil tested in tension-tension fatigue at ~80% of its tensile strength. Note fatigue striations oriented normal to the direction of crack propagation (arrow).

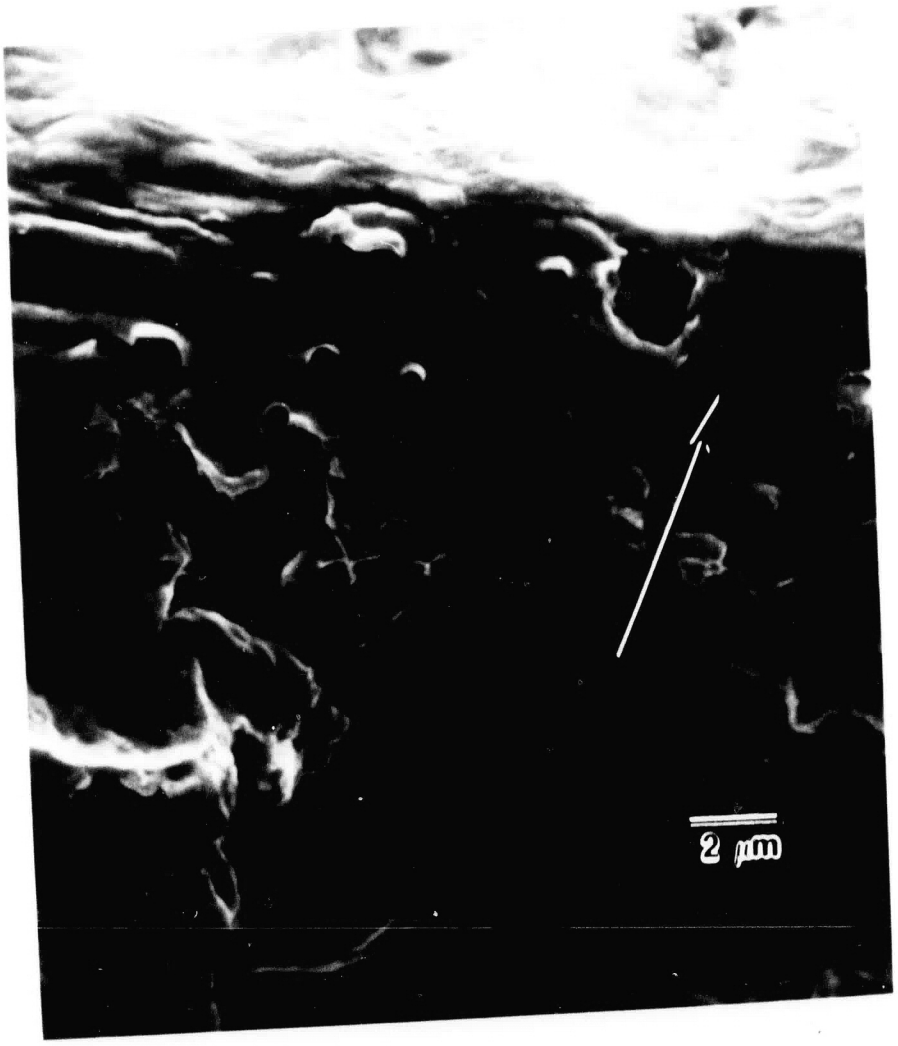
2 μm

electroless copper in MIB-PTH applications, it is imperative to determine several factors which directly affect the PTH structure; these variables include:

- the initial stress state of the PTH barrel
- the stress-strain distribution within the PTH structure as a function of temperature change in the MIB
- the effect and relevance of the copper/epoxy-glass interface adhesion
- the mechanical properties of the materials used in the MIB-PTH structure.

For the most part, the stress-strain information pertaining to the PTH was obtained through the finite element analyses of Section 4.1.2, while the mechanical properties of the electroless copper were obtained from the tensile tests as described in Section 4.2.1. From the information gathered in the above sections it was possible to design a specimen which possessed many of the properties of the PTH structure. The specimen developed, shown in Figure 11, allows the copper plated along the through hole wall to undergo compression without buckling, so as to simulate service conditions associated with fully-reversed strain cycling.

Finite element analysis of the gage section of the CSF specimen (Figure 14) revealed that for a uniform load, the strain in the copper barrel (B) was one-half the strain in the epoxy-glass, located at the specimen center along the outside diameter (A). Therefore, the strain in the copper barrel was computed by multiplying the specimen strain, (calculated from the calibration procedure) by the strain ratio of 0.5

as determined from FEA of the gage section. No attempt to evaluate local stress concentrations was included in any of the analyses.

Data Analysis

The CSF properties were obtained for 4 failure criteria based on the resistance change in the copper barrel (200, 500, 1000, and 2000 μΩ) at each of three copper barrel nominal strains (0.01%, 0.023%, and 0.035%). The data for each failure criterion are given in Tables 4 to 7.

Figures 30a-d are plots of the cyclic strain versus cycles to failure for each of the four failure criteria. The results indicate that for each failure criterion, 1 and 6 micron polished specimens exhibited the greatest fatigue resistance. The shortest fatigue life was exhibit by the "low ductility" contaminated electroless copper. The 6:1 aspect ratio specimens appeared to have better life as compared with the control group. This improvement in life is probably due to reduced copper barrel strains resulting from the change in sample geometry. No significant change in fatigue life was observed for the activation processes used in initiating the deposit's growth. It is interesting to note here that the most significant improvement in fatigue life was achieved by reducing the surface roughness of the drilled hole. It should be noted that this also serves to reduce the level of mechanical adhesion along the copper/epoxy-glass interface (e.g. 1 and 6 micron polished). By contrast, the lowest fatigue life occurs in samples containing the lowest ductility of the electroless copper.

Table 4

Cycles to Failure 200 μΩ Resistance Change

Specimen Classification	0.010% Strain	0.023% Strain	0.035% Strain
Control Group	340 747	259 160	74 67
Aspect Ratio 6:1	1854	223	130
6 Micron Polished	1540	197	50
1 Micron Polished	2540	275	102
Contaminated low ductility	181	103	16
Activator #1	428	148	60

Table 5

Cycles to Failure 500 μΩ Resistance Change

Specimen Classification	0.010% Strain	0.023% Strain	0.035% Strain
Control Group	493 1371	332 240	109 94
Aspect Ratio 6:1	2780	223	190
6 Micron Polished	2606	277	76
1 Micron Polished	3810	432	143
Contaminated low ductility	424	208	30
Activator #1	808	204	60

Table 6

Cycles to Failure 1000μΩ Resistance Change

Specimen Classification	0.010% Strain	0.023% Strain	0.035% Strain
Control Group	655	428	74
	2718	338	131
Aspect Ratio 6:1	3465	451	262
6 Micron Polished	4270	373	114
1 Micron Polished	5570	648	195
Contaminated low ductility	836	322	46
Activator #1	1340	256	102

Table 7

Cycles to Failure 2000 μΩ Resistance Change

Specimen Classification	0.010% Strain	0.023% Strain	0.035% Strain
Control Group	1787	598	231
	4598	489	180
Aspect Ratio 6:1	6186	754	425
6 Micron Polished	7540	547	180
1 Micron Polished	9862	1014	280
Contaminated low ductility	1678	511	57
Activator #1	2417	360	143

Figure 30: Plot of the cyclic strain versus cycles to failure for each of the four failure criterion (a) 200 μΩ, (b) 500 μΩ, (c) 1000 μΩ, and (d) 2000 μΩ.

a

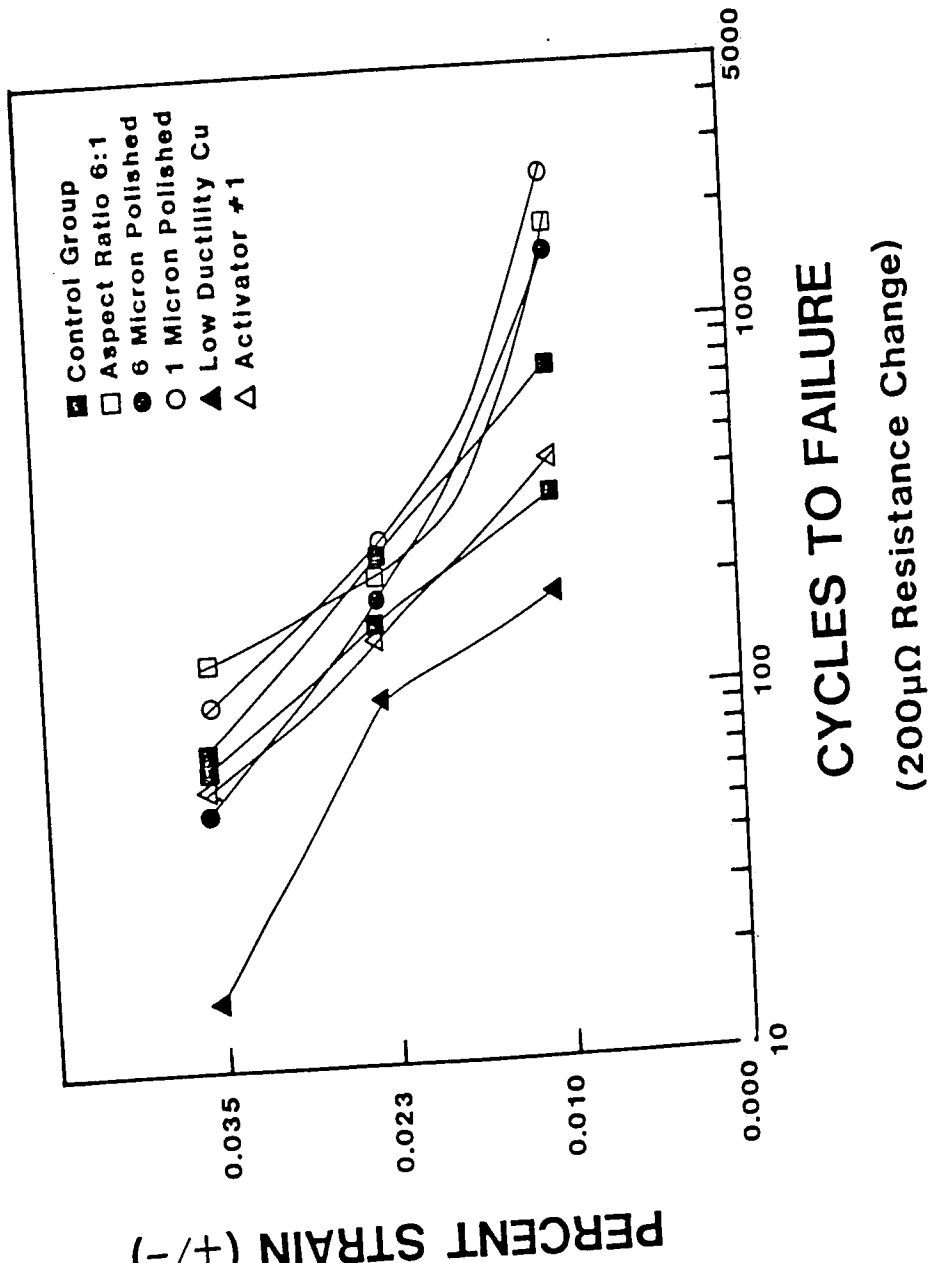
Control Group
Aspect Ratio 6:1
6 Micron Polished
1 Micron Polished
Low Ductility Cu
Activator #1
PERCENT STRAIN (+/-)
0.035
0.023
0.010
0.000
10
100
1000
5000
CYCLES TO FAILURE
(200μΩ Resistance Change)

Control Group
Aspect Ratio 6:1
6 Micron Polished
1 Micron Polished
Low Ductility Cu
Activator #1
PERCENT STRAIN (+/-)
0.035
0.023
0.010
0.000
10
100
1000
5000
CYCLES TO FAILURE
(500μΩ Resistance Change)

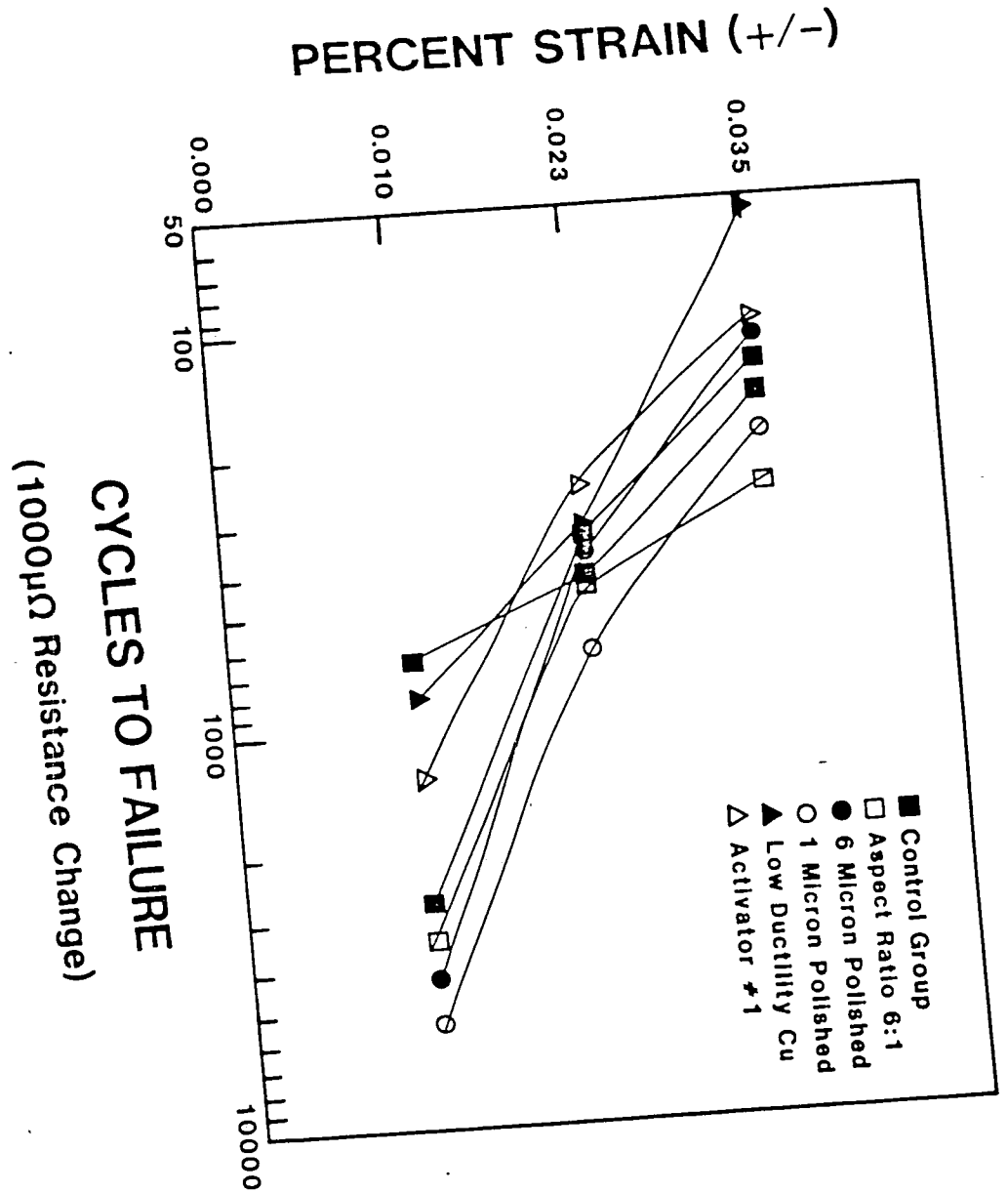
PERCENT STRAIN (+/-)
0.035
0.023
0.010
0.000
50
100
1000
10000
CYCLES TO FAILURE
(1000μΩ Resistance Change)
Control Group
Aspect Ratio 6:1
6 Micron Polished
1 Micron Polished
Low Ductility Cu
Activator #1

C

Control Group
Aspect Ratio 6:1
6 Micron Polished
1 Micron Polished
Low Ductility Cu
Activator #1
PERCENT STRAIN (+/-)
0.035
0.023
0.010
0.000
50
100
1000
10000
CYCLES TO FAILURE
(2000μΩ Resistance Change)

A separate plot can be generated for each strain range of testing by plotting the number of cycles required to change the copper barrel resistance by the amount of each failure criteria versus the resistance change (see Figures 31a-c). From these plots it appears that the data fall along approximately parallel curves. Since the curves are displaced vertically from one another by an amount corresponding to the number of cycles which changes the resistance by 200 μΩ, it is suggested that once cracking has begun the rate of subsequent cracking is independent of specimen preparation. However, it is clearly evident that specimen preparation influences the initiation process at each cyclic strain range. Therefore, reducing the surface roughness (i.e. stress concentrations) increases the cyclic strain fatigue life because the presence of significant stress concentrations essentially bypasses the initiation process. In addition, reducing the ductility of the material (i.e. by using contaminated, low ductility copper) reduces the fatigue life because less plastic deformation is available to resist crack formation. Though neither of these results are surprising, the importance of these observations will become more evident in light of the acoustic emission results.

A Coffin-Manson relationship based on the 2000 μΩ failure criterion is presented in Figure 32. By plotting the log $\Delta\varepsilon/2$ vs. $2N_f$, where $\Delta\varepsilon$ is the total barrel strain, and $2N_f$ is the total number strain reversals, a straight line relationship of the form:

$$\Delta\varepsilon/2 = 0.4\ (2N_f)^{-0.45} \tag{15}$$

Figure 31a-c: Plot of the number of cycles required to change the copper barrel resistance by the amount of each failure criterion versus the resistance change for each strain range (a) 0.035%, (b) 0.023% and (c) 0.010%.

a

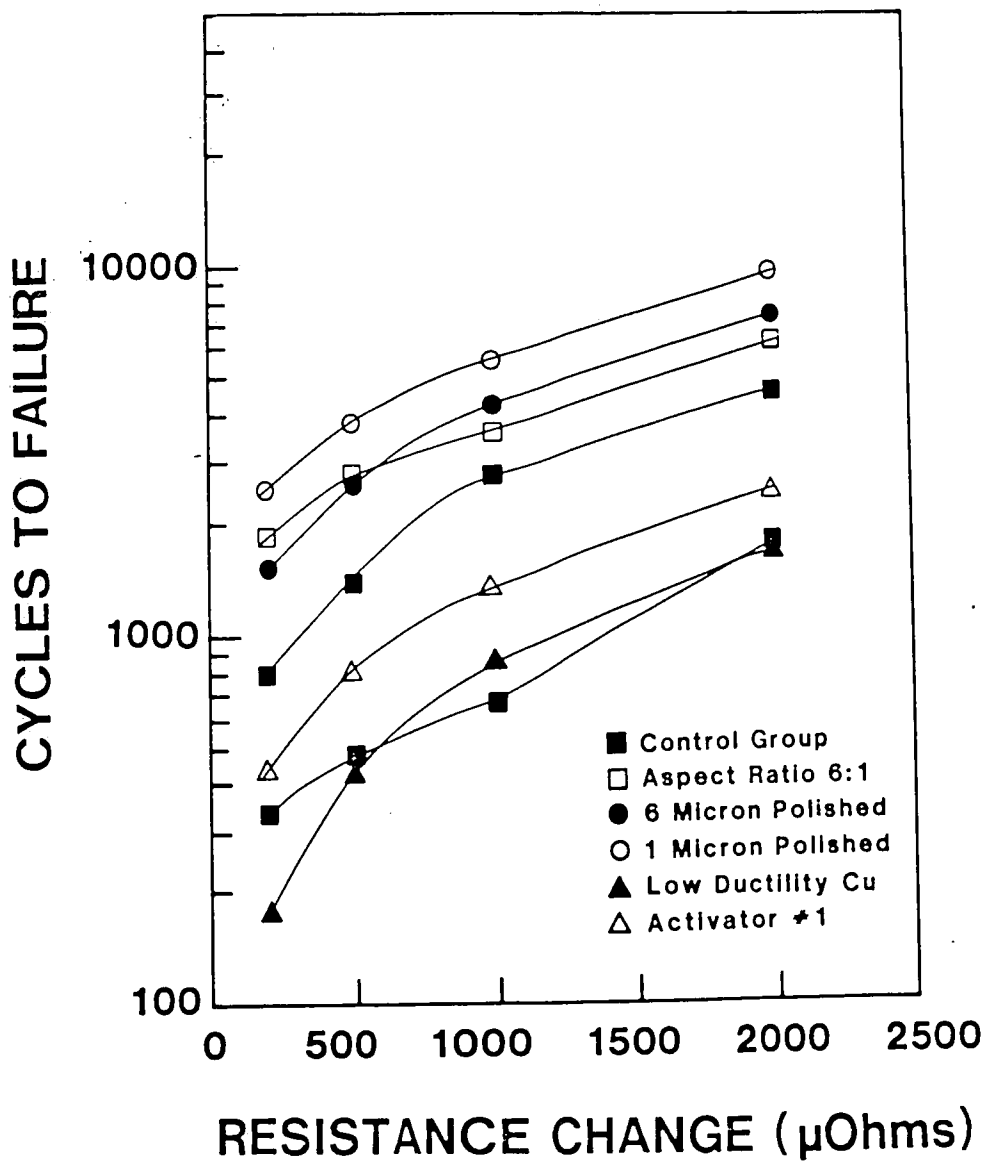
CYCLES TO FAILURE
10000
1000
100
0
500
1000
1500
2000
2500
RESISTANCE CHANGE (μOhms)
Control Group
Aspect Ratio 6:1
6 Micron Polished
1 Micron Polished
Low Ductility Cu
Activator #1

b

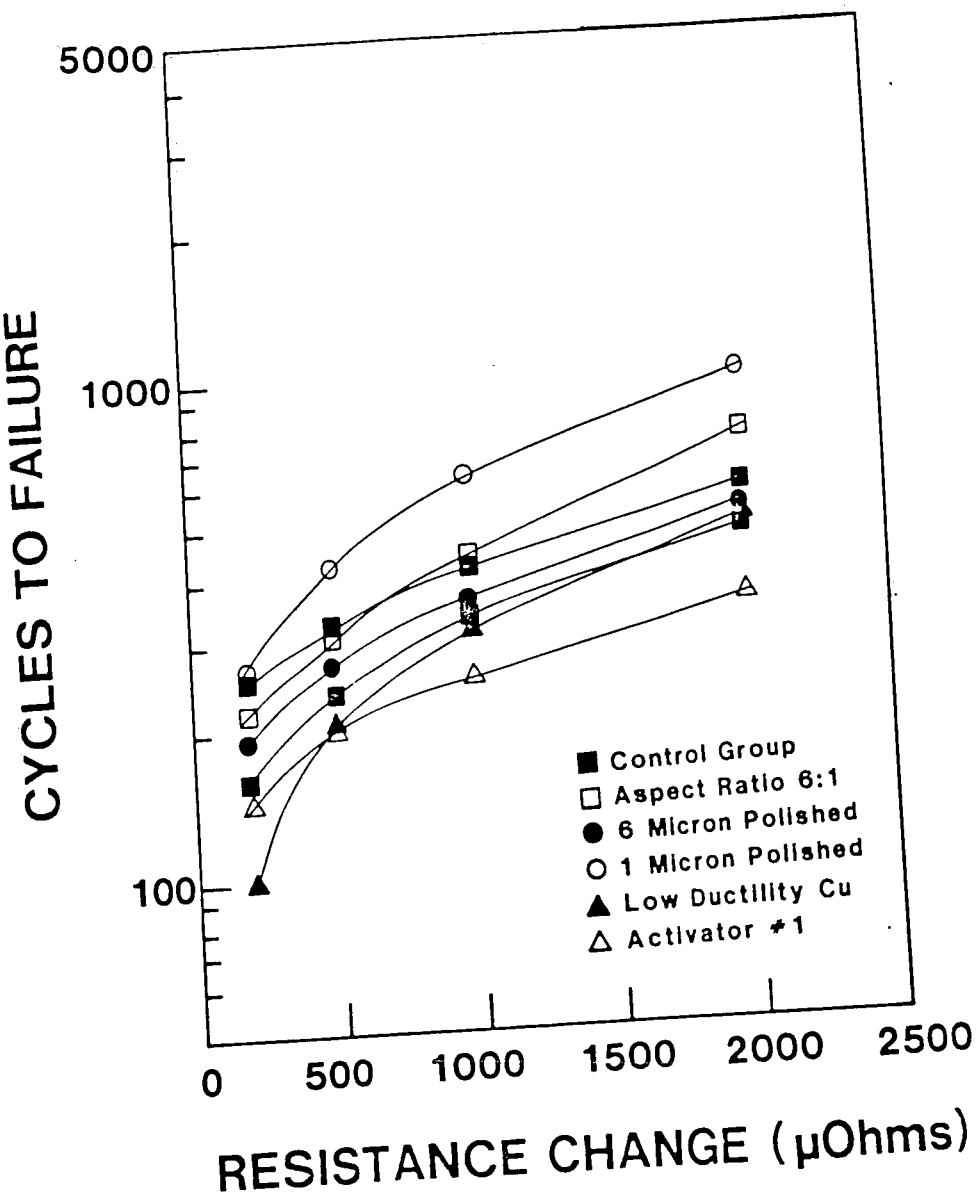
5000
1000
100
CYCLES TO FAILURE
0
500
1000
1500
2000
2500
RESISTANCE CHANGE (μOhms)
Control Group
Aspect Ratio 6:1
6 Micron Polished
1 Micron Polished
Low Ductility Cu
Activator #1

C

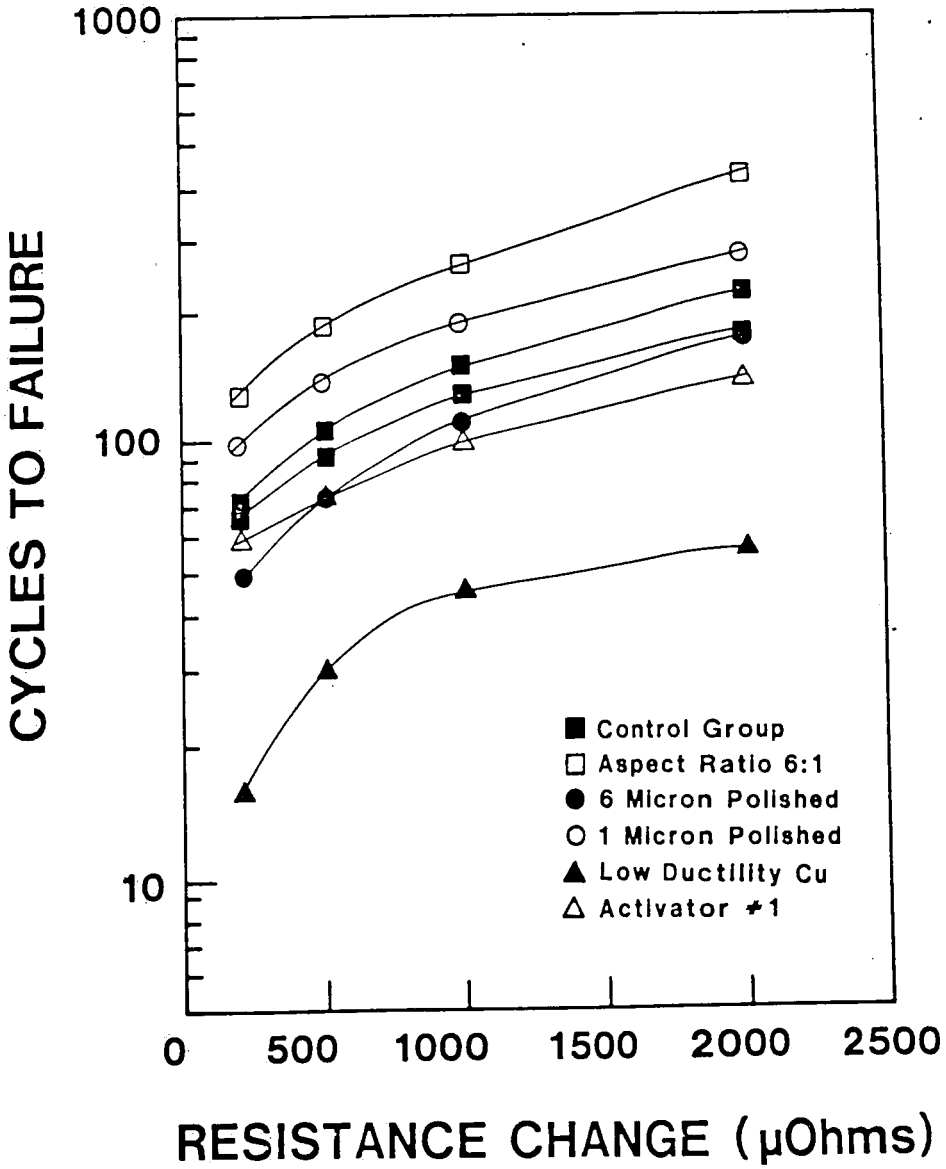
1000
100
10
CYCLES TO FAILURE
0
500
1000
1500
2000
2500
RESISTANCE CHANGE (μOhms)
Control Group
Aspect Ratio 6:1
6 Micron Polished
1 Micron Polished
Low Ductility Cu
Activator #1

can be described. The fatigue ductility coefficient of 0.4 was determined by extrapolating the curve to the strain intercept at one load reversal ($2N_f = 1$).

Acoustic Emission Analysis

Acoustic Emissions (AE) were recorded for each CSF (cyclic strain fatigue) specimen tested to provide information that would reveal the mechanisms associated with the specimen failure. Figure 33 is a plot of the AE data and resistance change data for the 0.035% strain range test of a control group specimen. The figure reveals the number of AE events versus the AE event amplitude versus the number of cycles (the representative third dimension); also shown is the resistance change versus cycles on a fourth axis. A good correlation exists between the rapid increase in AE events and the increased rate of resistance change. Thus, it would appear that the mechanism responsible for generating the AE is likely to be linked to the mechanism creating the changes in resistance. Since the test frequency was only 0.35 Hz at the strain range 0.035%, for which the largest number of events was recorded for all specimen preparations, direct observation of the sequence of events leading to failure could be made. Figure 34 shows a schematic diagram of the strain cycles, resistance change, and AE events observed during testing. The diagram illustrates that most of the AE events occur during the loading portion of the strain curve during which time little or no resistance change occurs. Shortly after the maximum tensile strain is achieved, a sharp decrease in AE events was observed. Following this sequence, a sudden burst of AE was detected which was associated with a

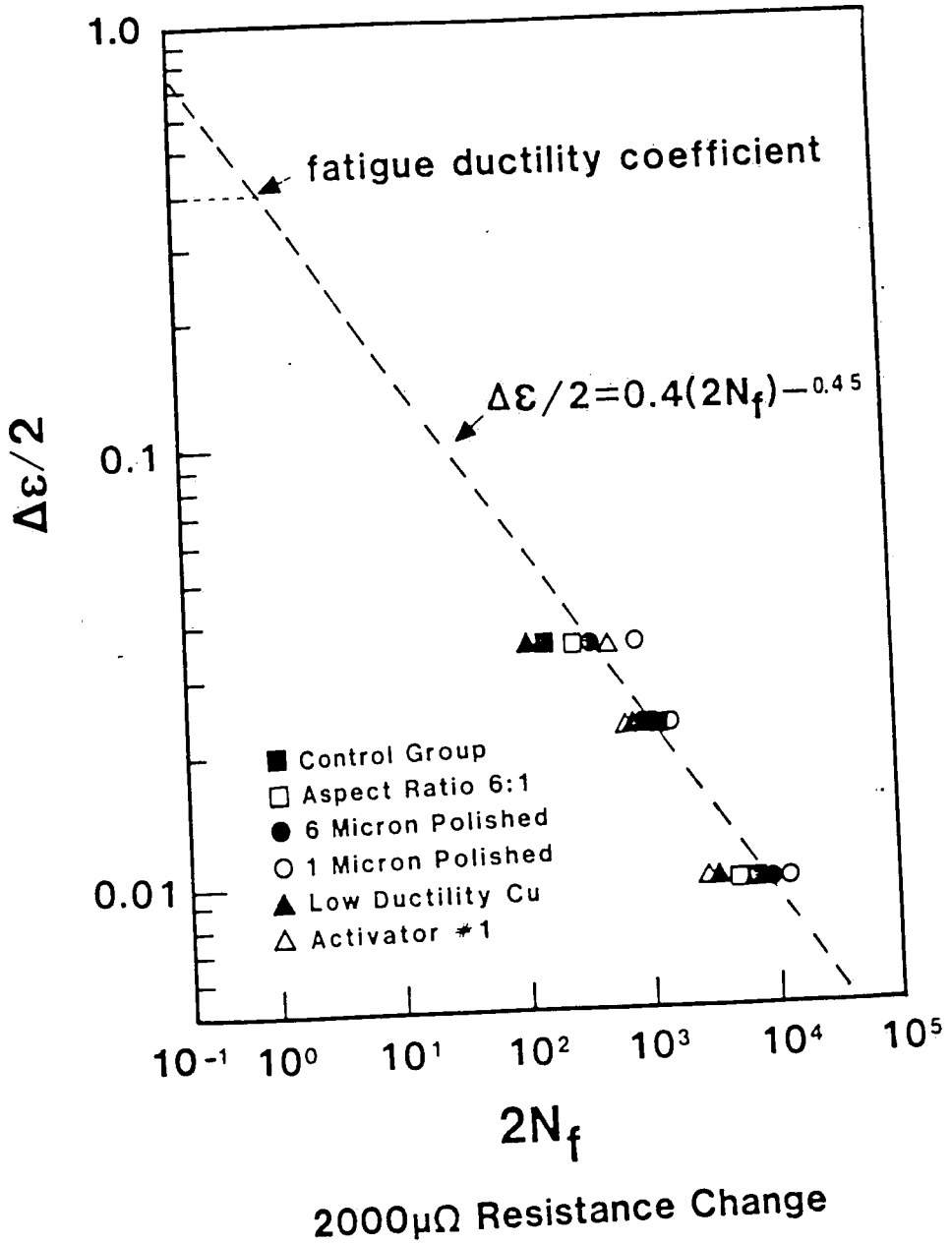

Figure 32: Coffin-Manson type plot for 2000 μΩ resistance change results. Extrapolating the data to one cycle yield a fatigue ductility coefficient of 0.4%.

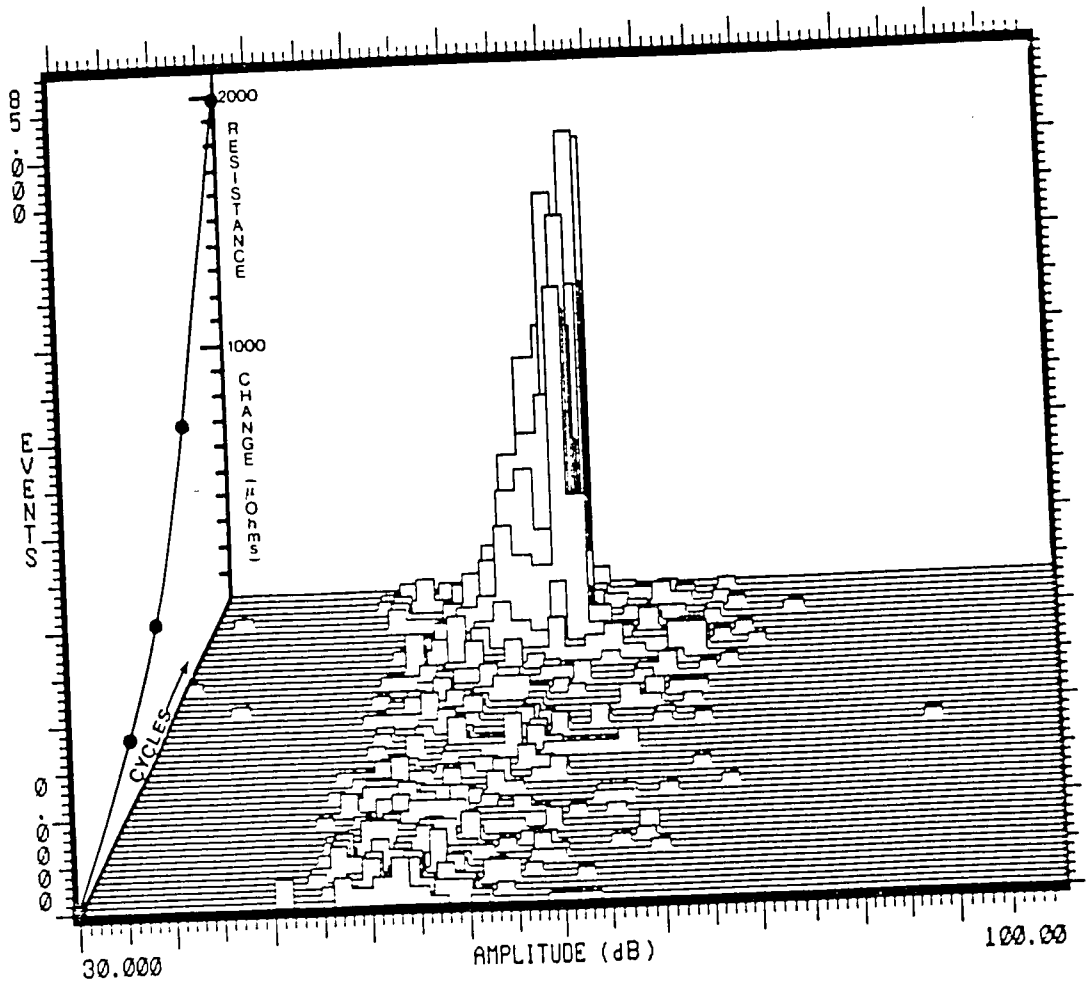

Figure 33: Two-dimensional representation of a three-dimension plot with four-labeled-axes for the AE and resistance change data for the 0.035% strain range control group specimen. Note the rapid increase in AE event corresponds to a sharp increase in resistance.

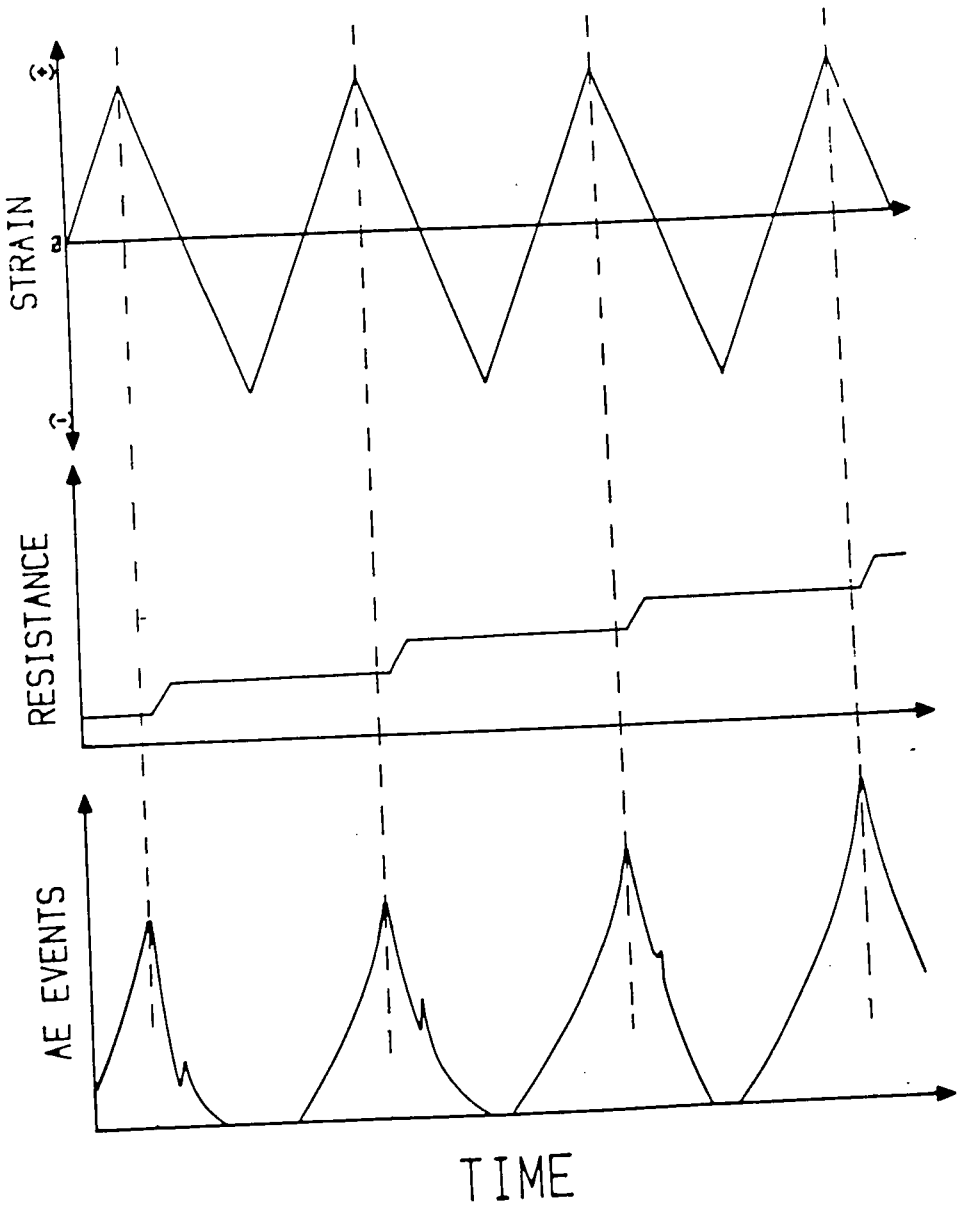

Figure 34: Schematic diagram showing the correlation of strain resistance change, and AE observed during CSF tests.

corresponding jump in resistance. After passing through the compressive strain region, the sequence was repeated on the following cycle.

The following model has been postulated to describe the sequence of deformation leading to failure in the 0.035% strain range tests. During tensile loading, the copper barrel begins to delaminate from the epoxy-glass along the copper/epoxy-glass interface. Shortly after unloading begins, the now plastically elongated and delaminated copper barrel begins to buckle; the associated bending stresses then lead to copper cracking at the center and ends of the delaminated portion of the copper barrel. It was found earlier from finite element analysis that when delamination occurs, the stresses at the center and ends of the delaminated region are significantly larger than those experienced over the majority of the barrel. Thus, when delamination occurs, the fatigue life would be expected to decrease.

A comparison of the AE results for each CSF test, given in Appendix 2, reveals that in almost every case in which the fatigue life of one specimen was shorter than that of another, the number of AE events was observably greater. For example, the number of AE events at each strain level recorded for the control group specimens (Figure 35a-c) was significantly greater than the number of AE events recorded for the 1 micron polished specimens (Figures 36 a-c). Correspondingly, the CSF life of the control group specimens was significantly shorter than the 1 micron polished specimens at all strain levels.

Figure 35a-c: Plots of AE data for control group specimens at each strain range tested, (a) 0.010%, (b) 0.02%, (c) 0.035%.

a

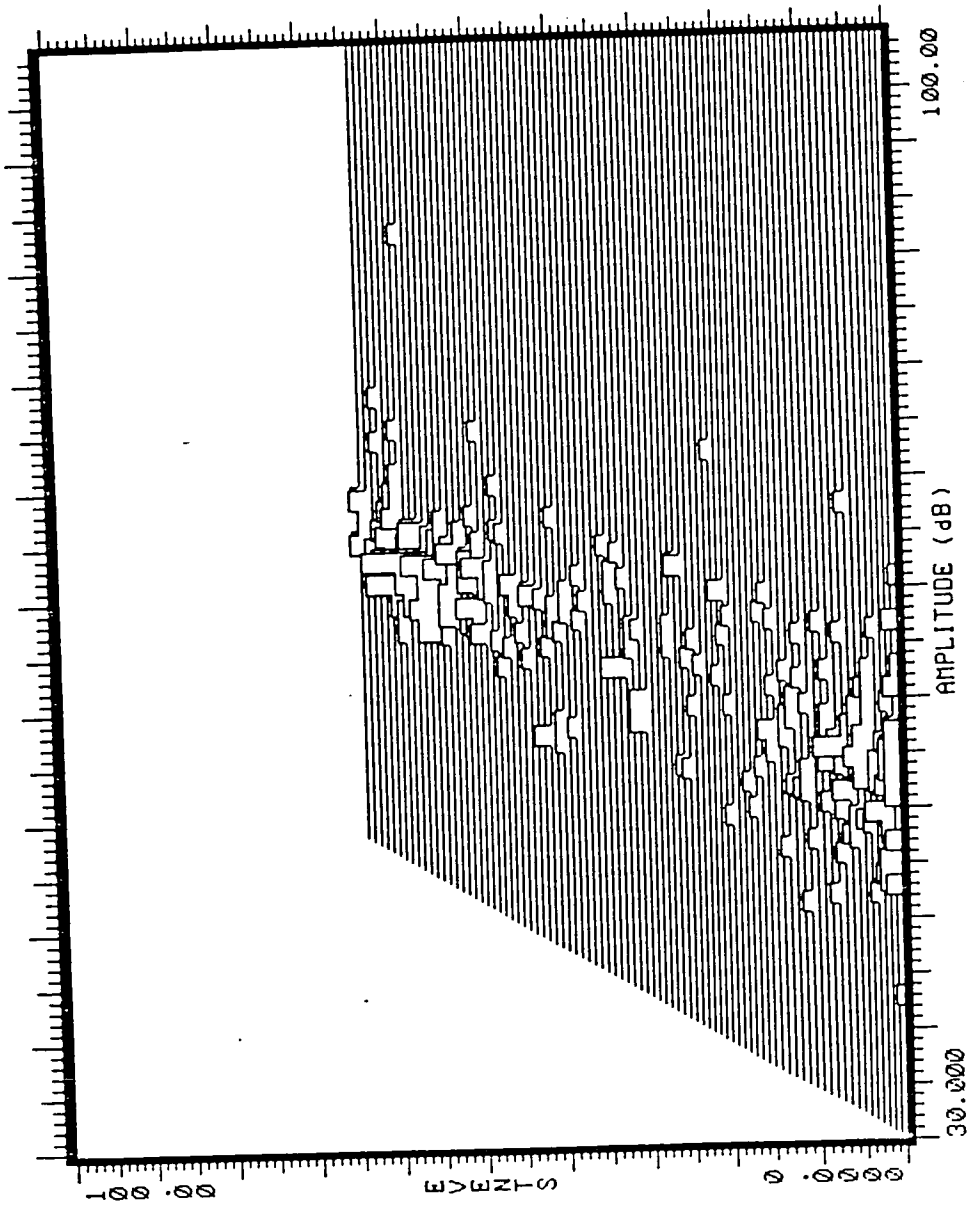

b

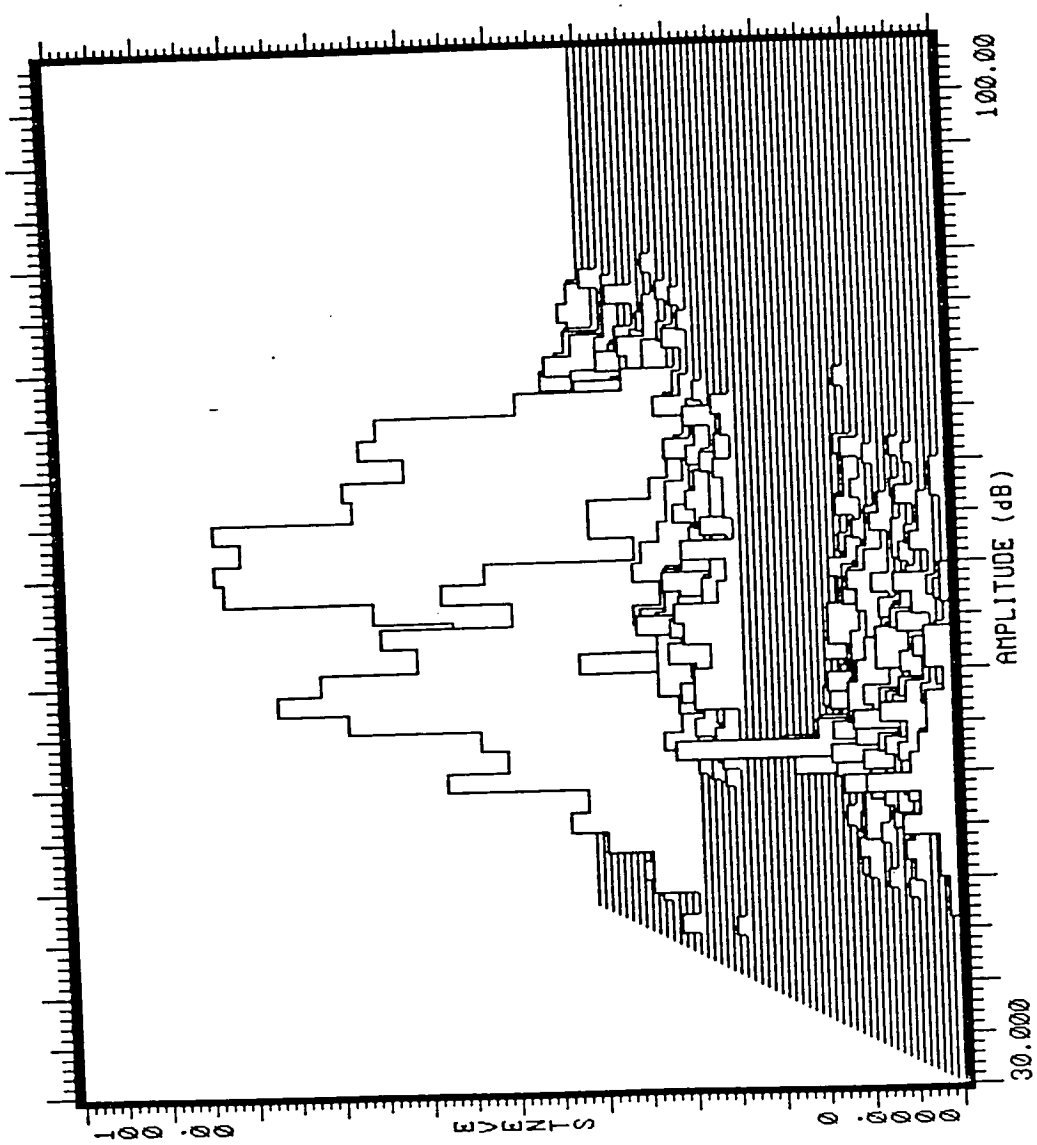

C

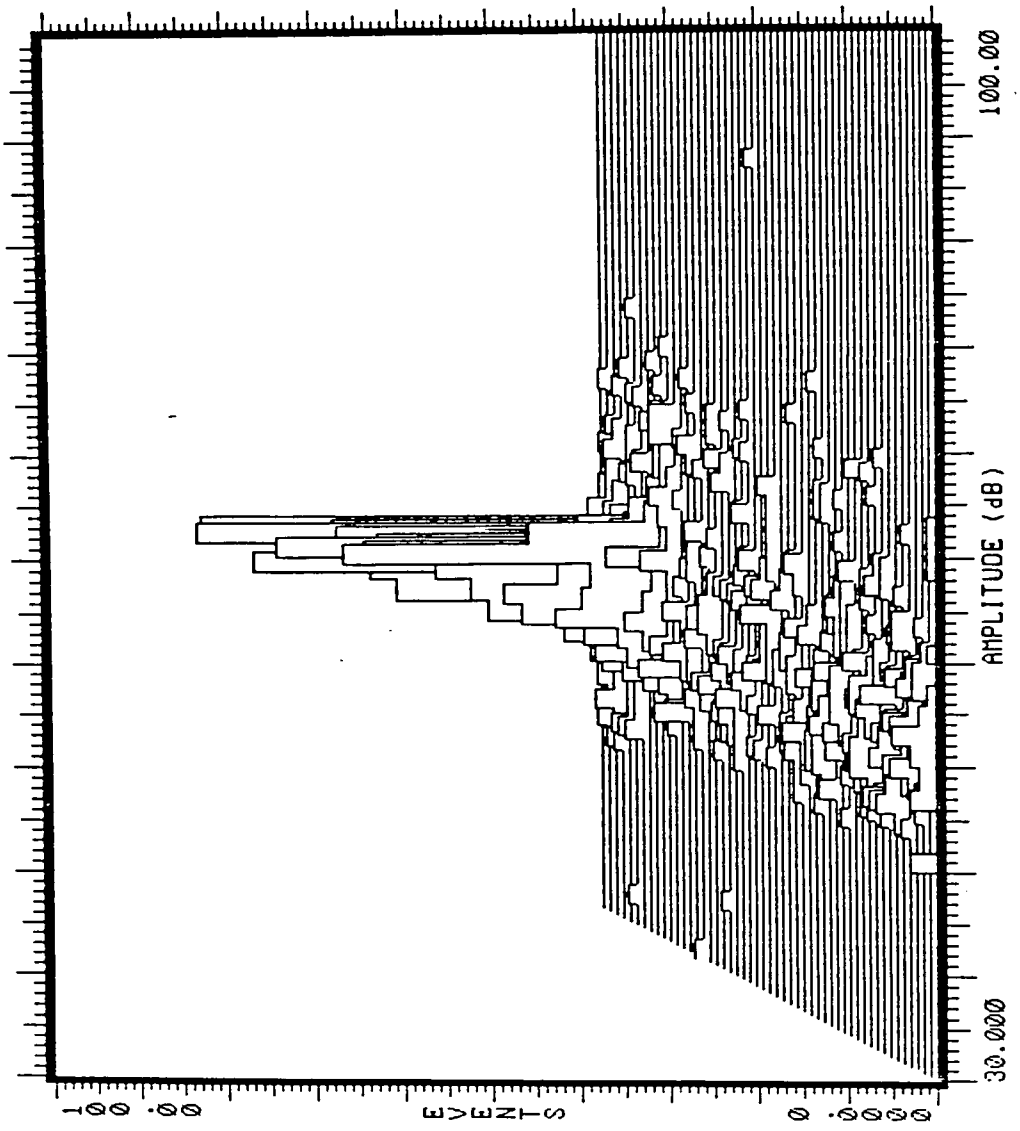

Metallographic examination of the gage sections of the CSF specimens revealed that significant delamination of copper/epoxy-glass interface was present in every sample that exhibited a large number of AE events. Conversely, when relatively few AE events were recorded, the gage section exhibited little or no delamination. Figures 37 and 38 show micrographs of portions of the copper/epoxy-glass interface in the 0.035% strain range specimens of the control group and 1-micron polished, respectively. It is evident from these micrographs that significant interfacial delamination occurred in the control group specimen, while little or no delamination was observed in the 1-micron polished specimen. In both cases, copper barrel cracks are clearly evident, the development of which were responsible for the observed resistance changes.

The observations described above indicate that reduction in the surface roughness along the copper/epoxy-glass interface reduces the tendency for the copper barrel to delaminate. These results are in contradiction to the peel test results of Lee et al. [41] where interface strength was seen to increase by increasing surface roughness. It was postulated that mechanical interlocking along the interface was primarily responsible for the interface strength. This may be true for the stress situation involved in the peel test; however, for the stress state of the CSF specimens used in this study, this is clearly not the case. Since the stress state in an actual PTH is more similar to that of the CSF specimen employed here, it is believed that mechanical interlocking is not an important mechanism in preventing interface delamination. Furthermore, reducing the

Figure 36a-c: Plots of AE data for 1 micron polished specimens at each strain range tested, (a) 0.010%, (b) 0.023%, (c) 0.035%.

a

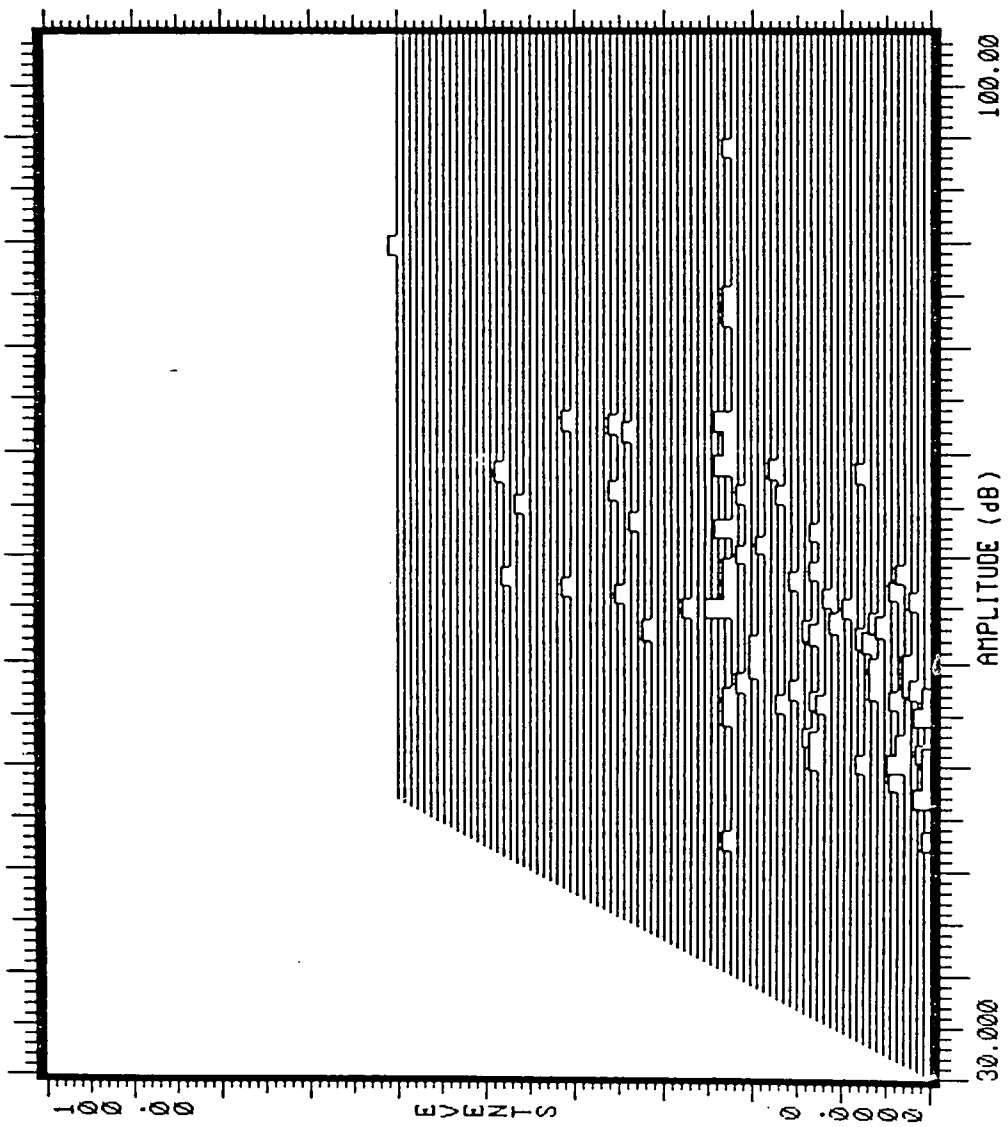

b

C

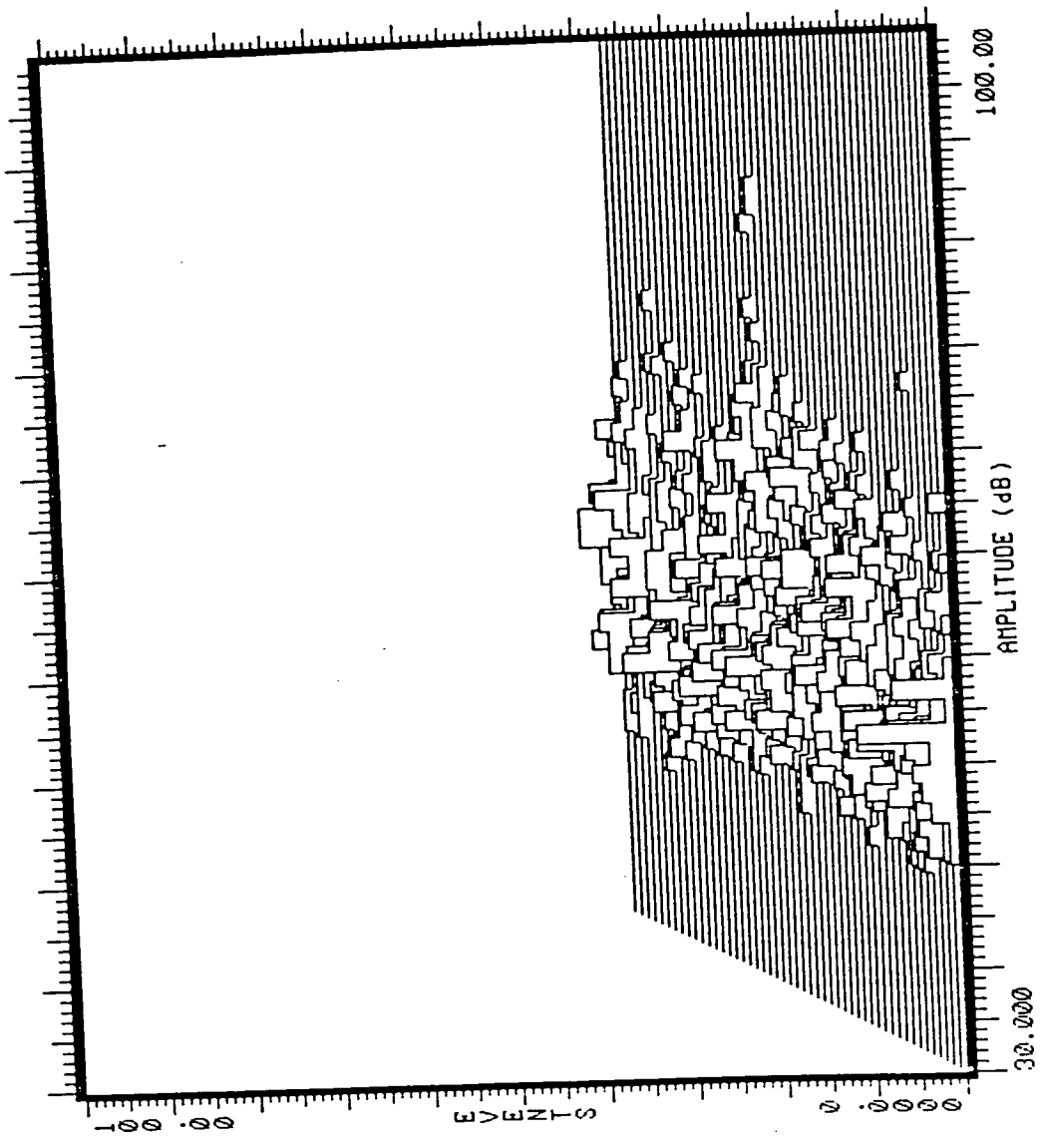

interface surface roughness results in reduced stress concentrations and improved fatigue life.

The gage section of each CSF specimen was also examined in the scanning electron microscope to determine the nature and extent of the copper barrel cracking. In all specimens examined, numerous cracks were observed along the gage length and these cracks were predominantly oriented normal to the loading direction (Figure 39). Furthermore these cracks appear to develop along the grain boundaries and propagate intergranularly (Figure 40). It is believed that these cracks initiate at columnar grain boundaries which coincide with the stress concentrations introduced by the rough interface.

Figure 37: Optical photomicrograph of the gage section of the 0.035% strain control group specimen. Note the separation along the copper/epoxy-glass interface as well as the copper barrel crack.

Figure 38: Optical photomicrograph of the gage section of the 0.035% strain 1 micron polished specimen. Note the good adhesion along the copper/epoxy-glass interface along with the copper barrel crack.

20 μm

20 μm

Figure 39: SEM micrograph showing numerous cracks (arrows) observed along the CSF specimen gage sections in all specimens tested. The cracks are oriented approximately normal to the loading direction.

Figure 40: SEM micrograph of a crack in the gage section of a CSF specimen. Note the intergranular path of the crack.


10 μm

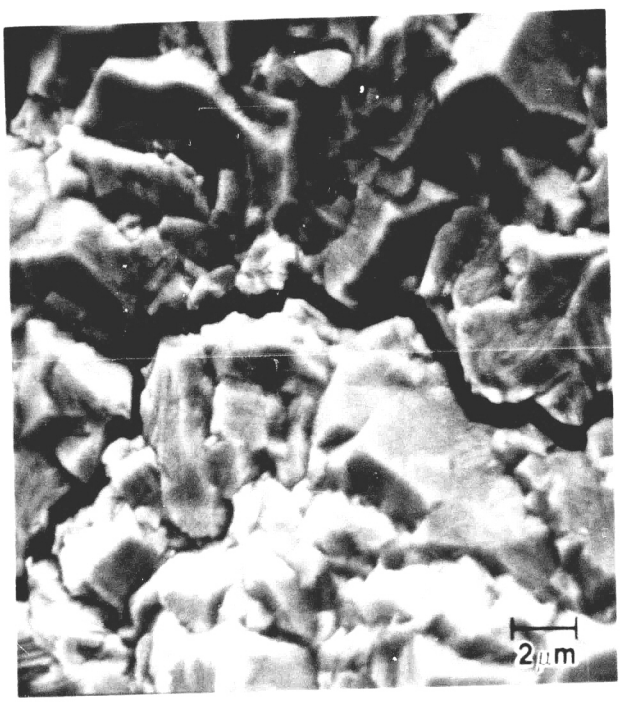
2 μm

4.3 MICROSCOPY

4.3.1 Surface Roughness

Numerous component failures can be attributed to stress concentrations associated with surface defects, large changes in cross-sectional area, and material processing defects. Such stress concentrations result in local amplification of stresses and lead to catastrophic failure or subcritical crack growth.

The stress concentrations associated with electroless copper in MIB and PTH applications have a significant effect on the mechanical behavior and component reliability. Although the size of these defects may be minute compared to those commonly encountered in larger-sized components, it is the relative size of these defects to the foil thicknesses that makes these stress concentrations so important.

The determination of the size of the surface defects in electroless copper in MIBs was conducted with the aid of a scanning electron microscope. The first method involved examining the electroless copper layers within the multilayer interconnection board. Figure 41 shows a portion of a copper interconnection plane revealing numerous defects along the copper surface which is deposited first. These defects develop because the copper first deposits and then grows with good parallelism to the roughness of the surface onto which it is deposited. It appears that the defects may penetrate up to 10 μm into the foil. Since foil thicknesses are approximately 40 μm, these defects may penetrate 25% into the foil thickness.

Figure 41: SEM micrograph of a portion of a copper interconnection plane in an actual MIB. Note the numerous stress concentrations along the copper/epoxy-glass interface.

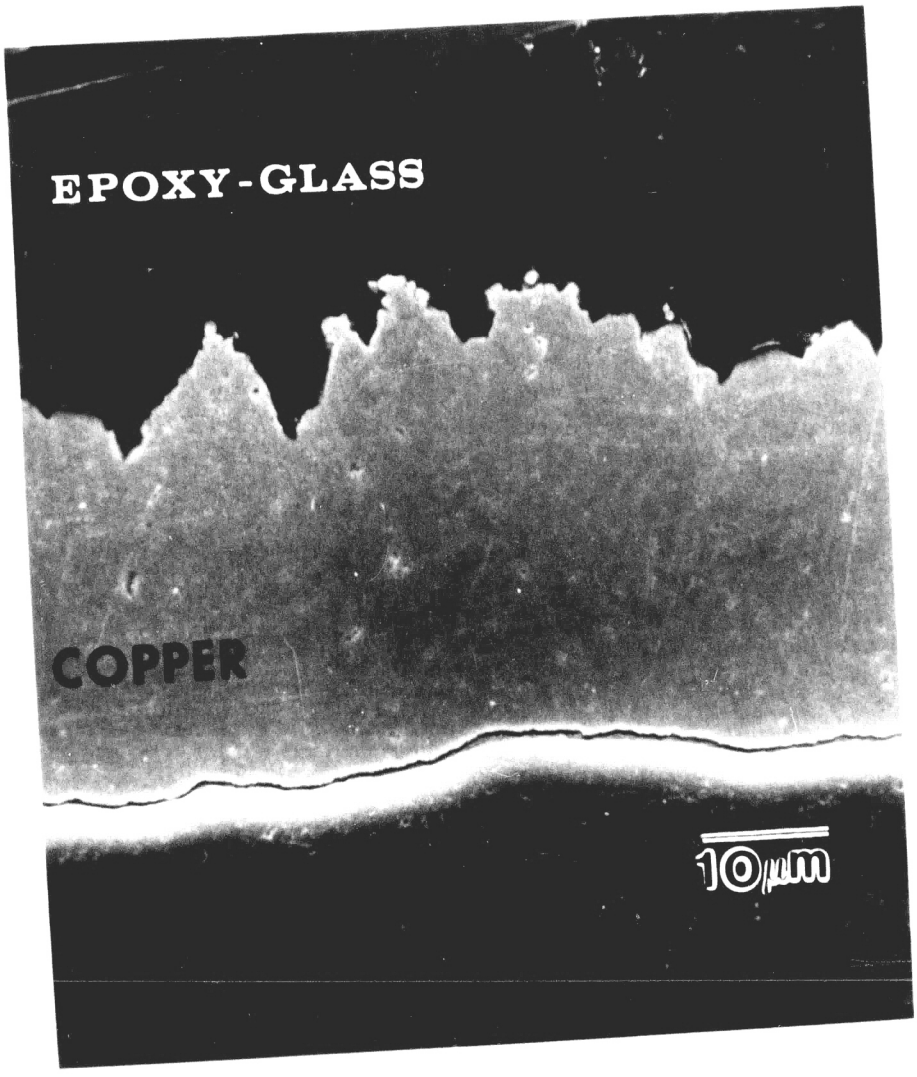
EPOXY-GLASS
COPPER
10 μm

The second method of examining the nature of these defects involved the use of stereomicroscopic analysis of the deposited surface. Stereomicroscopy allows the depth of the defects to be calculated from the stereo pair by the equation:

$$Z_c = \frac{P}{M\ 2\ \sin\ (\alpha/2)} \tag{12}$$

This technique also allows the width of defects to be determined to see how far across the foil width they extend. Figure 42a and 42b are a stereo pair of the deposit surface of the electroless copper foils. The height difference between certain points on the surface were calculated to determine the surface roughness (see Table 8). The results show good agreement with the values from the previous method; however, a single defect does not extend across the full width of the foil. Therefore, the stress concentrations are less ominous than that implied from the cross-sectional view of the foil as shown in Figure 41. However, the influence of this rough surface on the mechanical properties of the copper foils should not be underestimated. In section 4.2.1, the fracture surfaces of the tensile foils indicated that the fractures initiated from this rough surface, and low elongations to failure resulted. In addition, the tension-tension fatigue tests (Section 4.2.2) indicated that the fatigue cracks initiated along the rough deposit surface, and the subsequent crack growth was away from this surface. From the above discussion it would appear that the scatter in the results of the tensile tests (i.e. yield and ultimate tensile strengths and elongation to failure) are

Table 8

Stereomicroscopy Surface Roughness Determination

Positions	Z_c (μm)
1-5	4
4-6	6
2-8	8
3-9	8
3-6	6
2-5	10
1-9	6

Ave. = 6.8 μm

Figure 42: Stereo pair of the deposited surface of electroless copper foils. The numbered points indicate locations used for height difference determinations, the results of which appear in Table 8. [$\alpha=32°-25°=7°$]

a

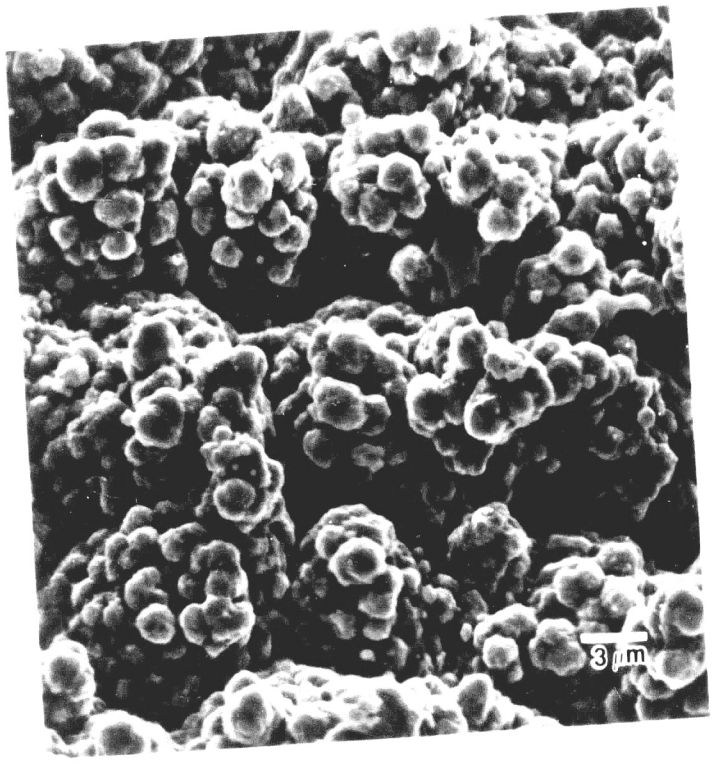

b

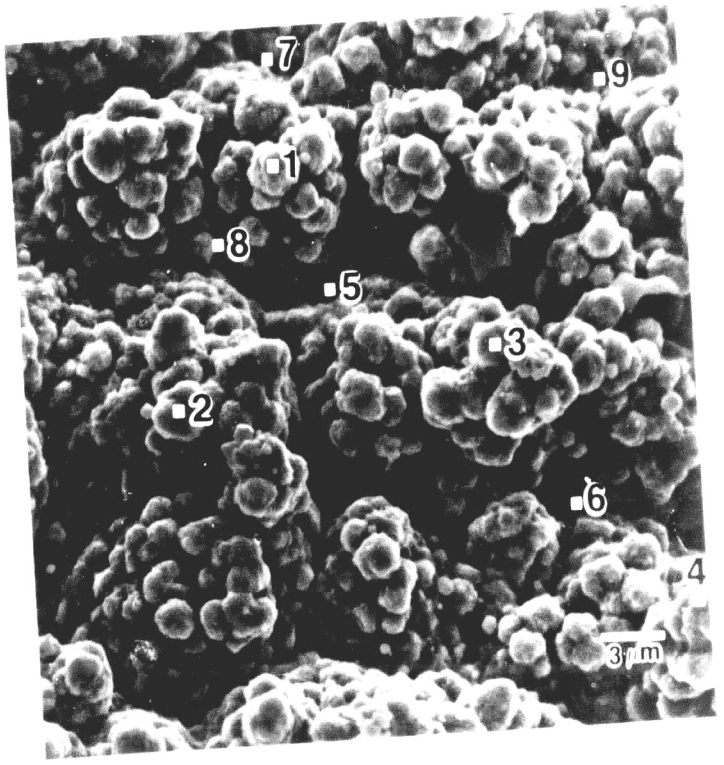

attributable to the variation in surface roughness from one foil to another.

The results of the cyclic strain fatigue experiments reinforce the importance of the surface roughness in determining the mechanical behavior of electroless copper. Clearly, the specimens for which the surface roughness was reduced (one and six micron polished) exhibited the best fatigue lives at all strain levels. Since all the other specimen parameters were unchanged from the control group preparation, the reduced surface roughness was considered to be solely responsible for the improved cyclic life.

4.3.2 Fatigue-Dislocation Arrangements

Three mm diameter discs were punched out of the gage centers of the electroless copper foils tested to 10^1, 10^2, 10^3 and 10^4 tension-tension cycles at a stress range of 80% of their tensile strength. These discs were examined in the TEM to observe the dislocation arrangements resulting from the cyclic deformation.

The dislocation arrangement after 10 cycles is shown in Figure 43 as an inhomogeneous distribution with dislocation free grain interiors and dislocation enriched grain boundary regions. Since more slip systems are usually operative near grain boundaries, the dislocation density near grain boundaries increases faster than in grain interior. After 100 cycles, the dislocation distribution becomes more homogeneous (Figures 44a and b) as dislocations move across the entire grains, thereby increasing the lattice strain in the grain interiors. The dislocation density significantly increases after 1000 cycles, Figure 45, with the distribution becoming more

Figure 43: TEM micrograph of electroless copper showing dislocation arrangement after 10 tension-tension fatigue cycles.


1 μm

Figure 44a,b: TEM micrographs of electroless copper showing dislocation arrangement after 100 tension-tension fatigue cycles.

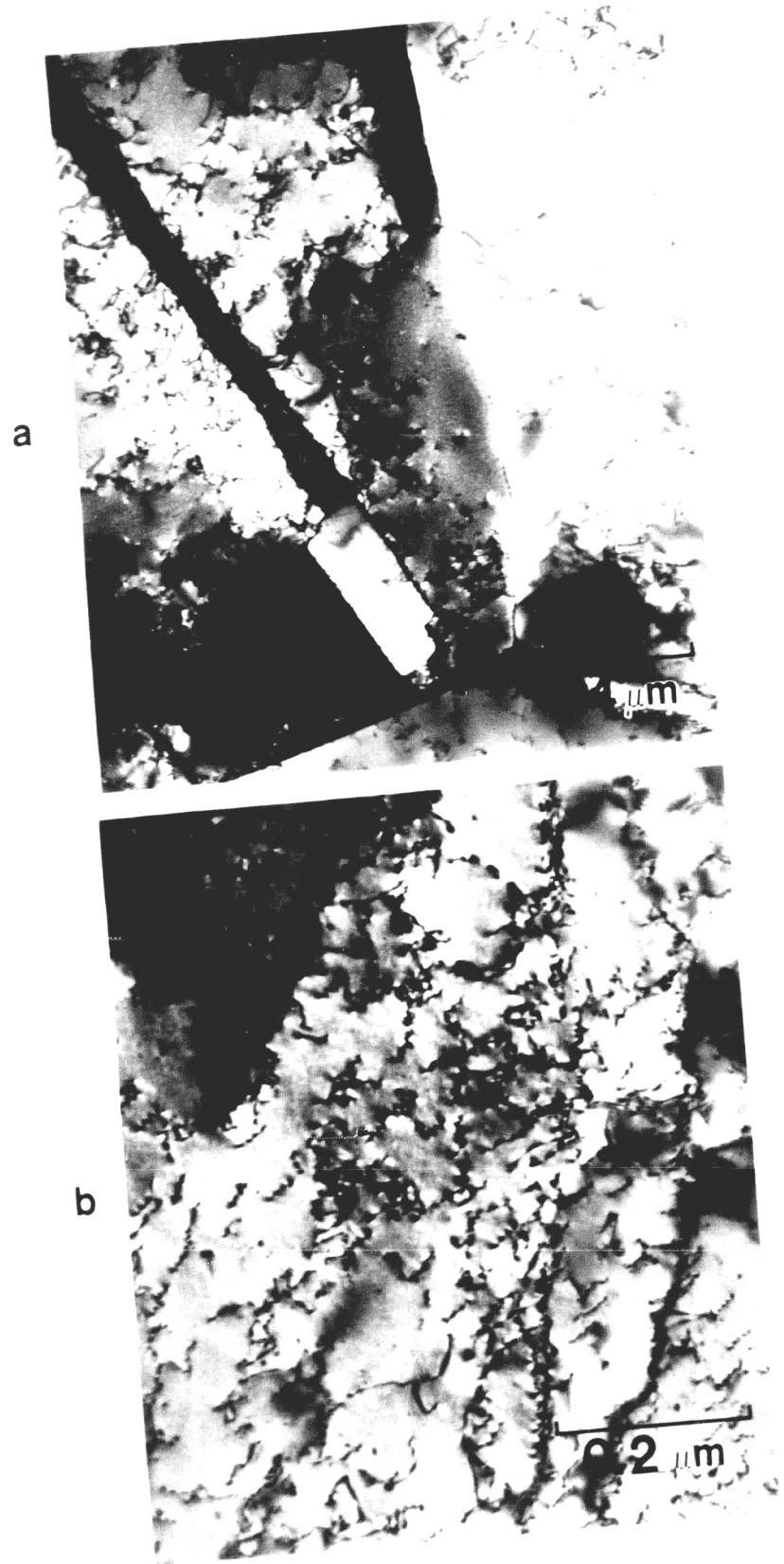
a
0.2 μm
b
0.2 μm

inhomogeneous as dislocations begin to become tangled and pile-up along grain and twin boundaries (Figure 46). After 10,000 cycles, the dislocations have arranged themselves into well-defined cells (Figure 47a,b), and the dislocation density has only increased slightly from that associated with 1000 loading cycles.

It has been previously reported that the formation of dislocation tangles is important in the stabilization of cyclic hardening [42], as dislocation tangles behave as sources of mobile dislocations as well as obstacles to dislocation movement. The observation of twin boundaries impeding the motion of dislocations and creating dislocation tangles in electroless cooper suggests that when numerous annealing twins are present in the microstructure, the twin spacing is likely to play a dominant role in the mechanical behavior of the material. The dislocation arrangements observed resulting from fatigue deformation are similar to those previously reported for FCC single crystals and polycrystalline specimens [43,44] and show that cyclic hardening occurs in electroless copper when subjected to large cyclic stresses.

4.3.3 Analytical Electron Microscopy (AEM)

EDS X-ray Microanalysis

X-ray microanalysis of grain boundaries in electroless copper foils was carried out in the AEM to determine whether any impurity elements were segregated to the boundaries thereby embrittling them. It is postulated that if segregation is to exist in this material, the segregant species is likely to be sulfur since the plating bath is replenished with a copper sulfate solution.

Figure 45: TEM micrograph of electroless copper showing dislocation arrangement after 1000 tension-tension cycles.

Figure 46: TEM micrograph of electroless copper showing dislocatoin pile-ups along twin boundaries evident after 1000 tension-tension cycles.

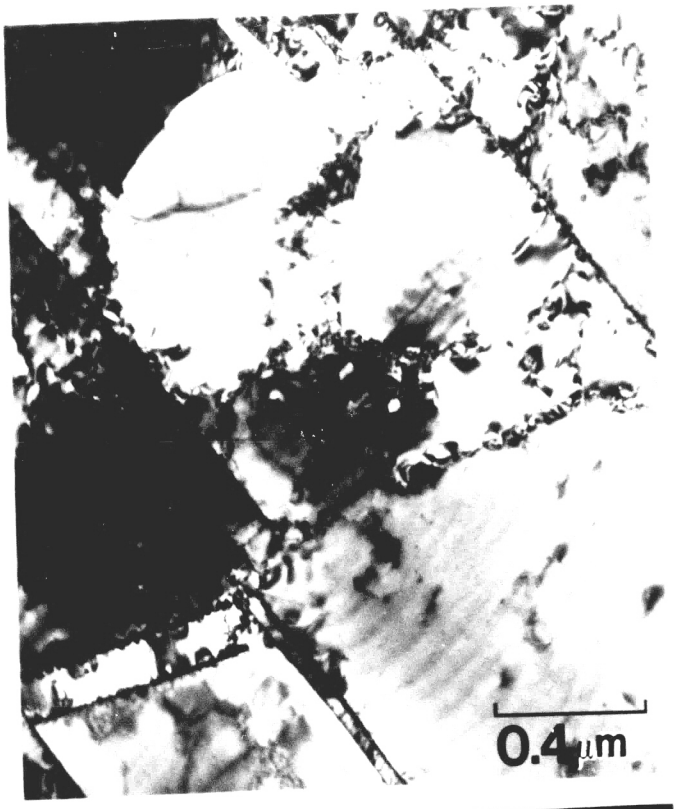
0.4 μm

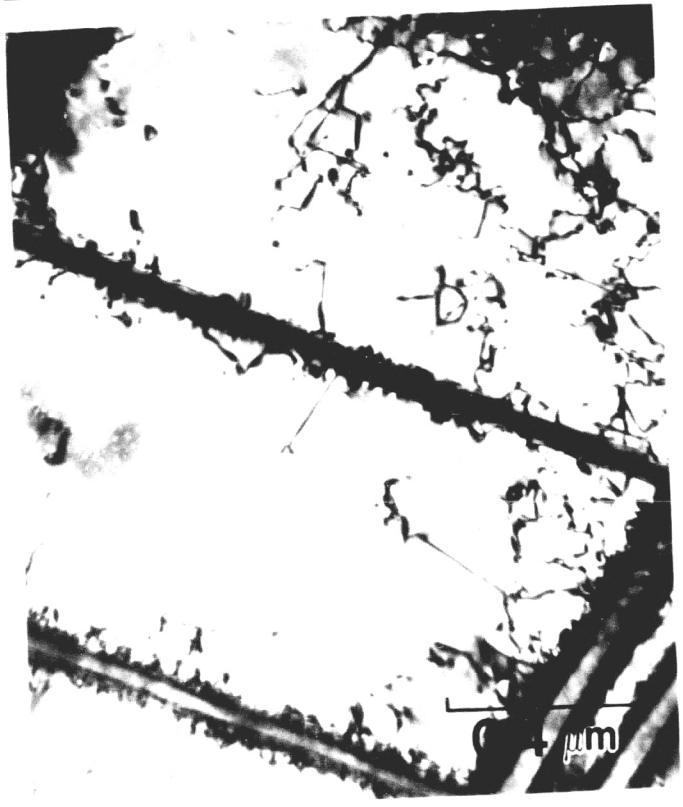

Figure 47a,b: TEM micrographs of electroless copper showing dislocation arrangement after 10,000 tension-tension cycles, (a) overall dislocation distribution, (b) dislocation cells.

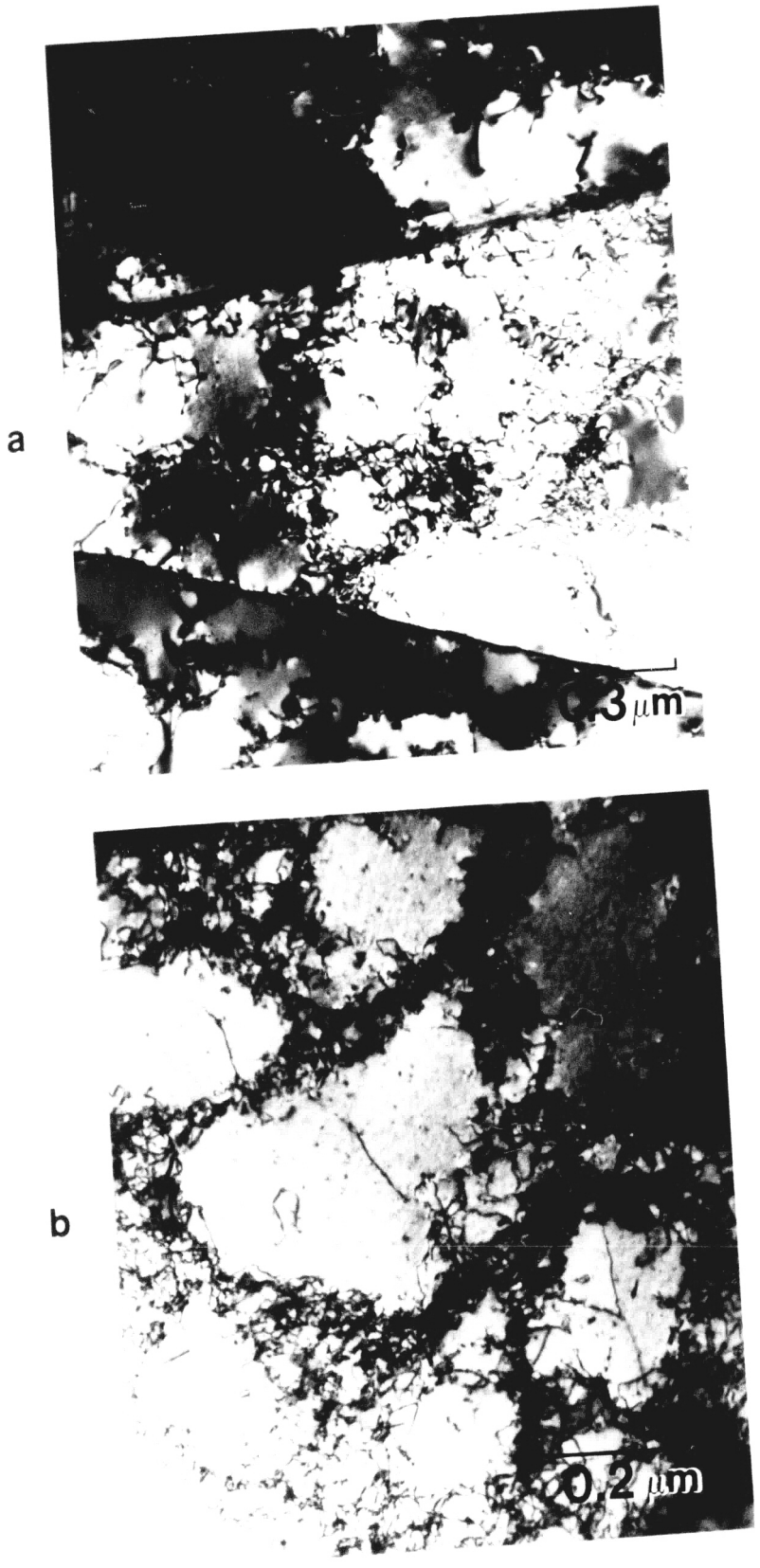
a
3 μm
b
0.2 μm

Furthermore, since the solubility of sulfur in copper is negligibly small at the plating bath temperature, any sulfur that might be dissolved in the electroless copper foils would likely be located at grain boundaries.

It is important now to consider the detectability limit of sulfur in copper when analysis of grain boundaries is performed. Since the interaction volume of the electron beam contains only a small volume of the grain boundary, even when significant segregation exists, the number of x-rays generated by the segregant is small compared to the number generated by the bulk material. Therefore, a minimum amount of segregant must exist on the boundary in order for it to be detectable above the continuum x-ray background. Michael [45] has determined the detectability limit of several segregants in copper to be as low as 0.067 wt% in the interaction volume. If the detectability limit for sulfur is assumed to be 0.1 wt% conservatively larger than that found by Michael, the minimum detectable grain boundary sulfur composition is 1.14 wt%, for a foil thickness of 1000A, and operating conditions of 120 kV and a 50Å beam size. These detectability limits were determined using the interaction model of Baumann and Williams [16] assuming a 10Å thick boundary.

Figure 48 shows a typical grain boundary observed in electroless copper. The boundary has been tilted to be parallel to the incident beam, and analyses were conducted by positioning the beam along the boundary plane.

Numerous boundaries in each of several thin foils were analyzed, the majority of which showed no impurities to be present. However,

Figure 48: TEM micrograph of a typical grain boundary which has been oriented parallel to the electron beam.

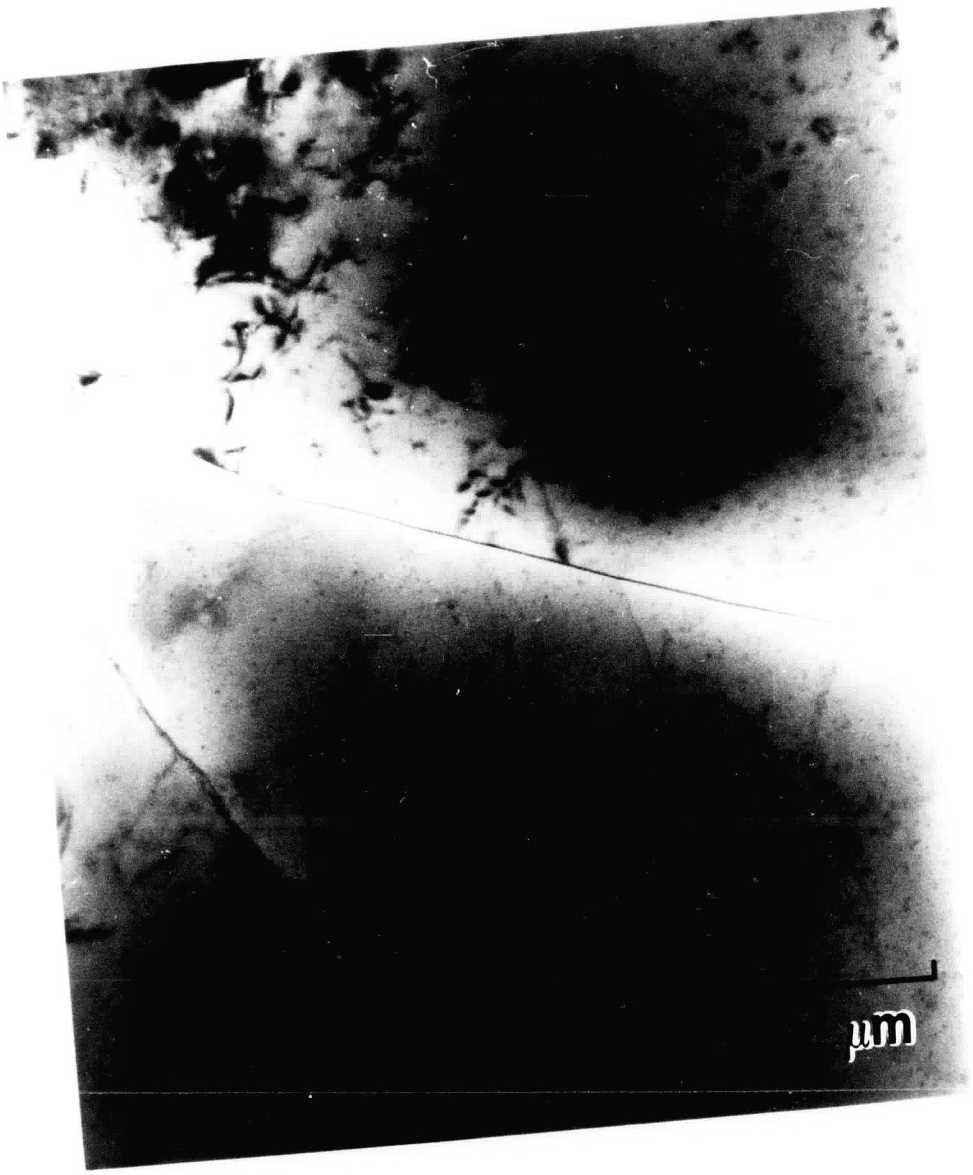
µm

during several analyses, small x-ray peaks appeared in the 1-5 keV energy range of the spectra. The centroids of these x-ray peaks did not necessarily coincide with the characteristic x-ray peaks for elements in this region; however, the peak widths often overlapped different elemental x-ray energies. It was considered necessary to determine the origin of these peaks before they could be attributed to impurity elements. Similar peaks have recently been detected in x-ray spectra in the AEM by Reese, et al. [46] and Spence, et al. [47]. It is theorized that these peaks, termed coherent bremsstrahlung (CB) peaks, arise due to an electron energy loss effects when analyses are carried out close to exact zone axes where a distinct periodicity in the lattice exists. It has been suggested that CB peaks, which are Gaussian, may either mask, or be misinterpreted as elemental peaks in x-ray spectra. A method for identifying and isolating these peaks has been presented by Spence et al. [47]. The problem of CB peaks is particularly severe in AEM grain boundary segregation studies because the amount of segregant in the interaction volume is small ($<\sim 3$ wt%), and the x-ray counting times are long; as a result, the CB peak intensities can approximate to the expected segregant peak intensity. The misleading effects of CB can be either the production of pseudo-element peaks close to true element peak positions, or the overestimation of the true element peak intensity when the CB peaks are superimposed on the x-ray peak of the segregant.

A unified theory predicting CB developed by Kurizki and McIver [48] has been used to interpret CB spectra [46]. A simplified expression for the coherent bremsstrahlung energy is [49]:

$$E(kv) = 12.48\beta/L(1-\beta \cos(90+\theta) \quad (16)$$

where $\beta = v/c$, θ is the detector take-off angle, and L is the atomic spacing in the beam direction ($1/L=g_z$ in zone axis orientation). L can be experimentally determined from convergent beam diffraction patterns containing high order Laue zone rings. Since L values can be determined for each high order Laue zone, it is expected that individual CB peaks will be generated from each high order Laue zone. For common accelerating voltages used in AEMs ($\sim$100 kV) and at typical atomic spacings ($d\sim0.3$ nm) in many important metals, CB peaks occur at energies from $\sim$1-8 keV. Specifically, at 120 keV, Equation (16) predicts that CB peaks will overlap within (+/- 100 eV) the primary x-ray peaks from S and bismuth segregants in copper, and P and Sn segregants in Fe, when analysis is carried out close to any of several major zones. For example, sulphur K_α (2.308 keV) is overlapped by CB peaks from copper when close to orientations of [110], [012], [114] and [122].

The predicted overlaps from Equation (16) were sought by observing CB peaks from commercially pure sample of copper and Fe. The spectra shown in Figures 49 and 50 were recorded employing a constant x-ray count rate into an EDAX energy-dispersive x-ray spectrometer ($\theta=20°$). Figure 49 shows spectra from copper in the [111] zone axis orientation as recorded at 120, 100, 80 and 60 kV. Figure 50 shows spectra from Fe recorded at 120 kV for zone axis orientations of [111], [110] and [210]. Note that the CB peak positions vary with kV for a given zone axis, and also vary with zone axis for a given kV. True elemental x-ray peaks do not vary as a

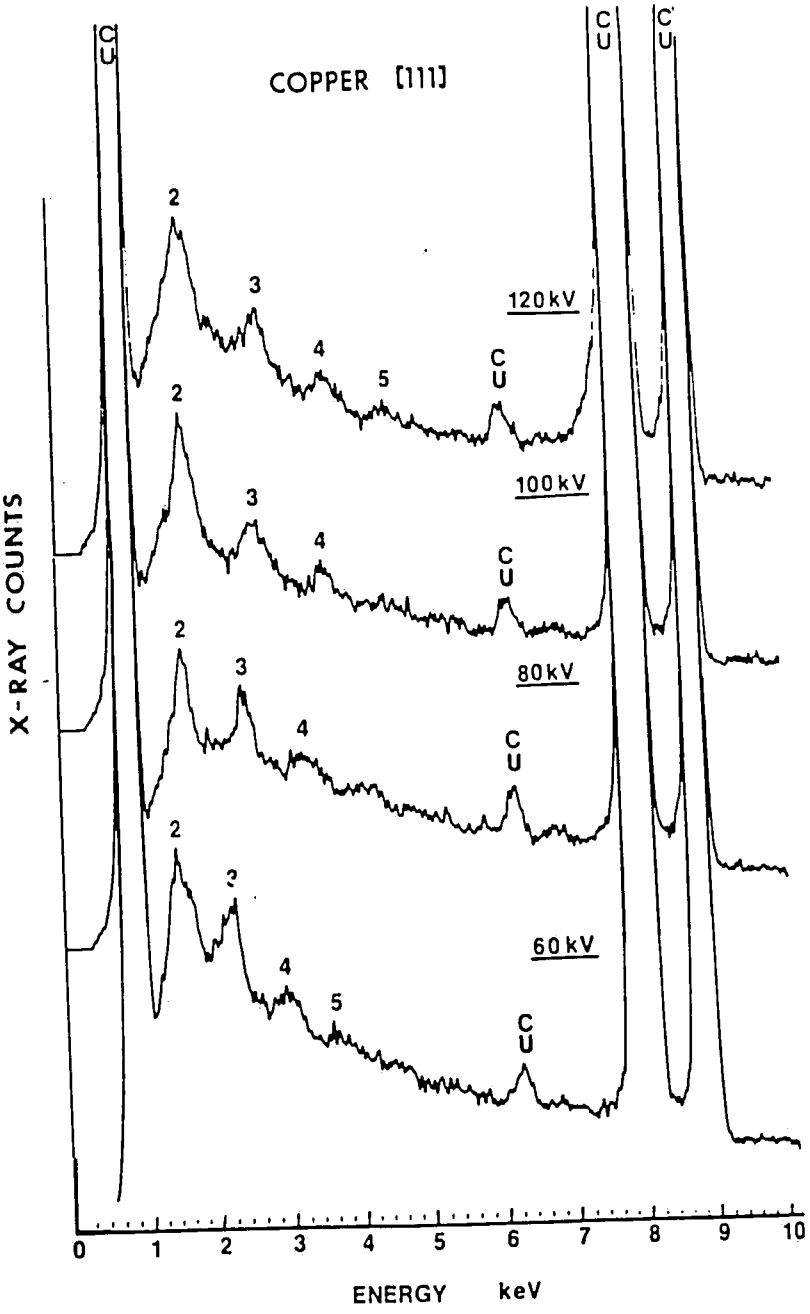

Figure 49: Copper [111] zone axis CB spectra for 120, 100, 80, 60 and kV. Integers above peaks correspond to the Laue zone from which they originate.

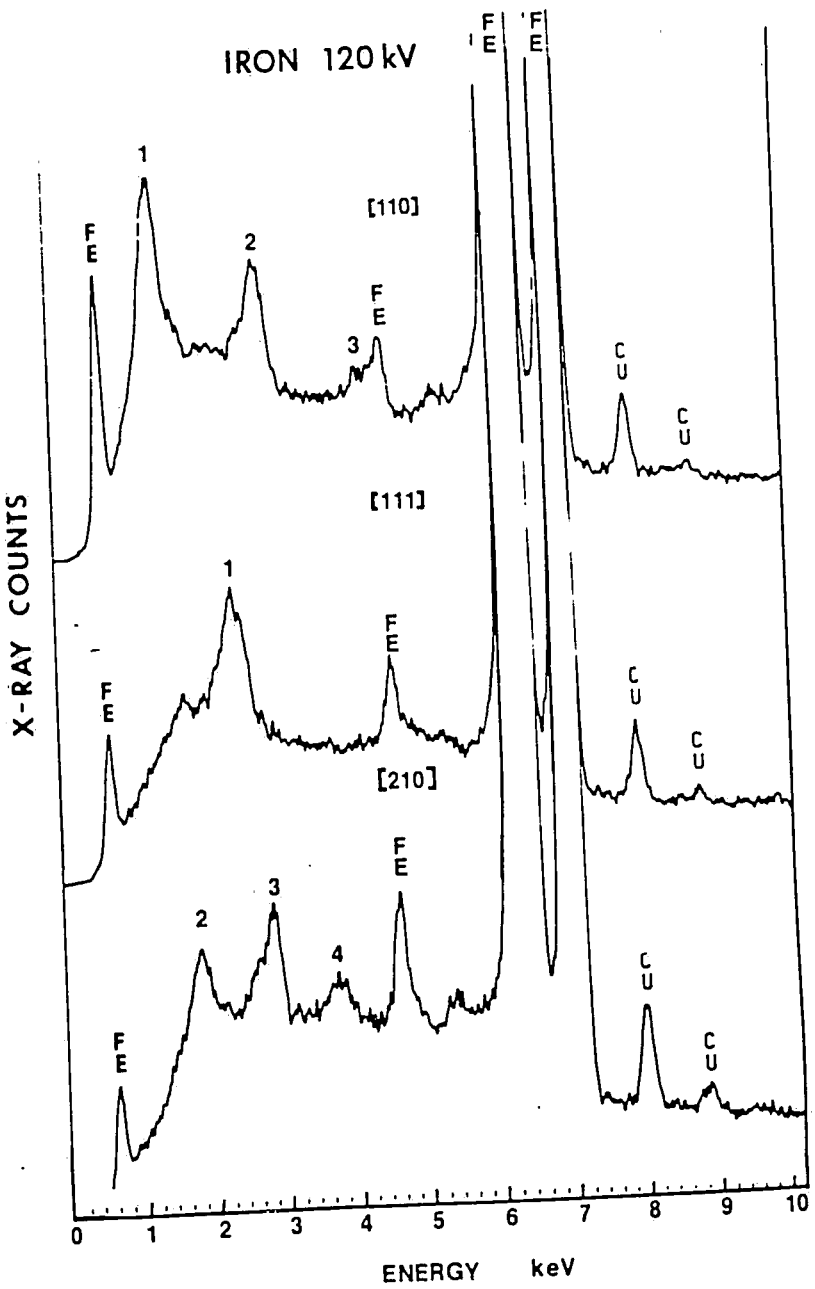

Figure 50: Iron CB spectra at 120 kV for zone axis orientations [110], [111] and [210].

function of either kV or orientation. All the peaks in Figures 49 and 50 coincide with peaks predicted from Equation (16). The segregation studies entail a further complication; the electron beam interacts with two grains, each of which generates its own CB peaks. Although AEM x-ray studies are not usually conducted under exact zone orientations, distinct CB peaks are observed as far as 6° away from exact zone. Figure 51 demonstrates the effect of tilting away from the exact [114] orientation on CB peak intensities in copper.

From the above evidence it may appear that CB peaks will almost always be expected in grain boundary studies. However, it is possible to choose analysis conditions (kV and orientation) such that segregant peaks may be observed unmasked by CB peaks. CB peaks are effectively absent far enough away from certain zones, and masked peaks can be verified if the segregant produces other x-ray lines (e.g., bismuth L_α (10.836 kV) is not masked by CB peaks in copper while bismuth M_α (2.423 keV) is often masked.

Having identified the origin of the peaks observed in the x-ray spectra obtained during the grain boundary segregation studies further analyses was carried out under operating conditions such that CB peaks would not develop. When the previously examined grain boundaries were reexamined, no peaks other than those corresponding to copper were observed. The results of the AEM grain boundary study indicates that impurity segregation is not a significant factor affecting the ductility of these electroless copper foils. However, due to the large variability in the electroless copper plating process these

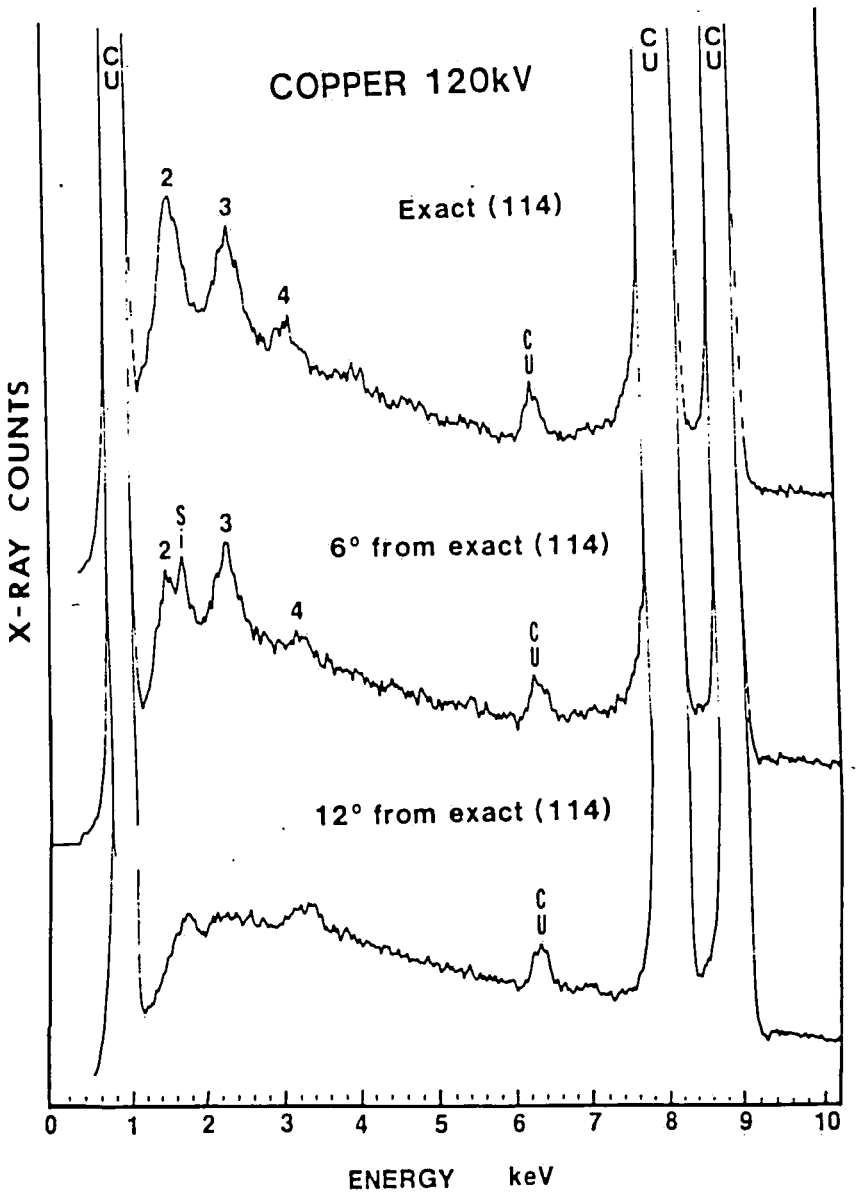

Figure 51: Copper CB spectra at 120 kV for three tilt positions: exact [114], 6° and 12° from exact [114]. Note that at 12° no CB peaks are apparent, although the overall background intensity is increased.

results can only be applied to the electroless copper used in this study.

4.3.4 Auger Electron Spectroscopy

From the appearance of the fracture surface of "good quality" electroless copper foils (Figure 24) it is difficult to assess whether the fracture occurs along a transgranular or intergranular path. The semi-flat nature of the surface as a whole suggests that fracture propagates along the relatively large columnar grain boundaries. It was of interest to determine whether these columnar grain boundaries or other fracture surface regions were associated with any significant impurity concentration. If impurity segregation is a significant factor affecting the mechanical behavior of the copper, the fracture path should be associated with the more highly segregated regions. Since AES is well suited for determining the elements associated with the fracture surface due to the high surface sensitivity of the AES technique, fracture surfaces were examined with the aid of this instrument.

To avoid contamination of the fracture surface, in-situ fracturing of the specimen of interest is generally conducted under the ultra high vacuum of the Auger instrument. In this study, in-situ fracturing of the electroless copper foils was not possible due to the low rigidity of the thin foils. As a result, specimen fracturing took place in open air and the specimens were quickly placed within the instrument. As a result oxidation and contamination of the fracture surfaces could not be completely avoided.

A typical AES scan of the fracture is shown in Figure 52. Present in the spectra are C and O peaks which can be attributed to atmospheric contamination, and a Cl peak due to the trichloroethylene cleaning solution in the specimen preparation. The N peak results from the epoxy substrate. In addition to the large expected copper peaks in the spectra, a small sulfur peak is also present. This peak is the largest sulfur peak observed in any of the AES scans. Even a conservatively large estimate of the amount of sulfur present results in less than 10 ppm wt.

The results of the AES study reveal that the fracture surfaces are not associated with any significant impurity segregation. The only possible exception to this may be the presence of $copper_2O$. However, if this oxide was present in large quantity, the oxygen peak would be expected to be significantly larger, as $copper_2O$ contains ~33 at% oxygen.

4.3.5 Residual Strain Evaluation Through Convergent Beam Electron Diffraction

Convergent Beam Electron Diffraction (CBED) was used to evaluate residual strain possessed by electroless copper in MIB applications. In ductile materials, such as copper, strain is not linearly proportional to stress over the major portion of its stress-strain response; in fact, strain increases at a much faster rate than stress. Therefore, residual strain will be evaluated with no direct relation to residual stress level being implied. Residual strain was evaluated by comparing the absolute lattice parameters determined from HOLZ line positions obtained from the electroless

Figure 52: An AES scan of a fracture surface of an electroless copper foil showing the presence of Cu, S, Cl, C, N and O. The C and O peaks can be attributed to fracturing the foil in the atmosphere. The Cl peak is the result of cleaning the foil in trichloroethylene, while the N peak is due to the epoxy substrate. The S peak represents the largest amount of S detected anywhere across the fracture surface.

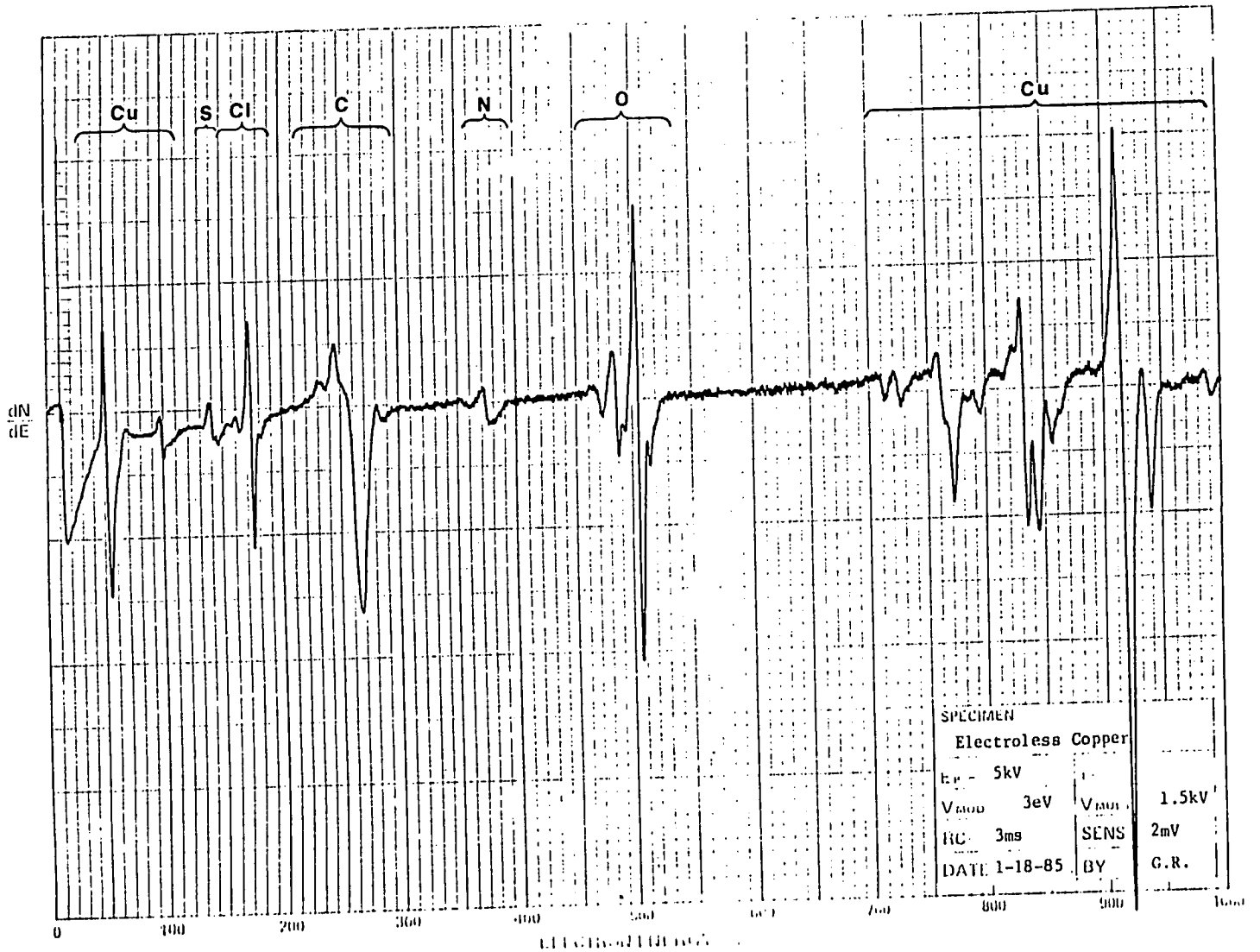
Cu
S
Cl
C
N
O
Cu
dN
dE
0
100
200
300
400
500
600
700
800
900
1000
SPECIMEN
Electroless Copper
5kV
3eV
1.5kV
3ms
2mV
DATE 1-18-85
BY
G.R.

plated copper to the HOLZ line positions from a commercially pure, annealed copper specimen. A relative change in HOLZ line position was considered to represent a measure of the residual strain. It should be noted that residual elastic strains cannot be evaluated from this technique as the procedure for producing thin foils is likely to relieve most elastic strains. However, any plastic strain introduced into the copper lattice will be evident as HOLZ line shifts.

In addition to determining whether a particular grain exhibited residual strains through HOLZ line shifts, a qualitative measure of the amount of residual strain in a particular specimen was made by observing the frequency of residually strained grains. This frequency was determined from the ratio of grains exhibiting residual strain (X) to the number of grains observed (N) in a certain sample, where $X \leq N$.

Calibration of the CBED Technique

The HOLZ line technique may be used for absolute lattice parameter determination if a calibration is initially carried out using a specimen of known lattice parameter close to that of the unknown specimens. For this purpose, pure, annealed copper was selected as the calibration standard. All CBED patterns were recorded at room temperature for which the lattice parameter of copper is 0.36150 nm.

CBED [111] zone axis patterns containing HOLZ lines were obtained using the conditions described earlier. [111] patterns possess a high degree of symmetry which allows small changes in lattice parameter to result in measurable HOLZ line shifts. Figure 53 is a low magnification CBED pattern of pure copper indexed as [111]. A high

Figure 53: A low magnification [111] CBED pattern of pure annealed copper with the HOLZ ring indexed.

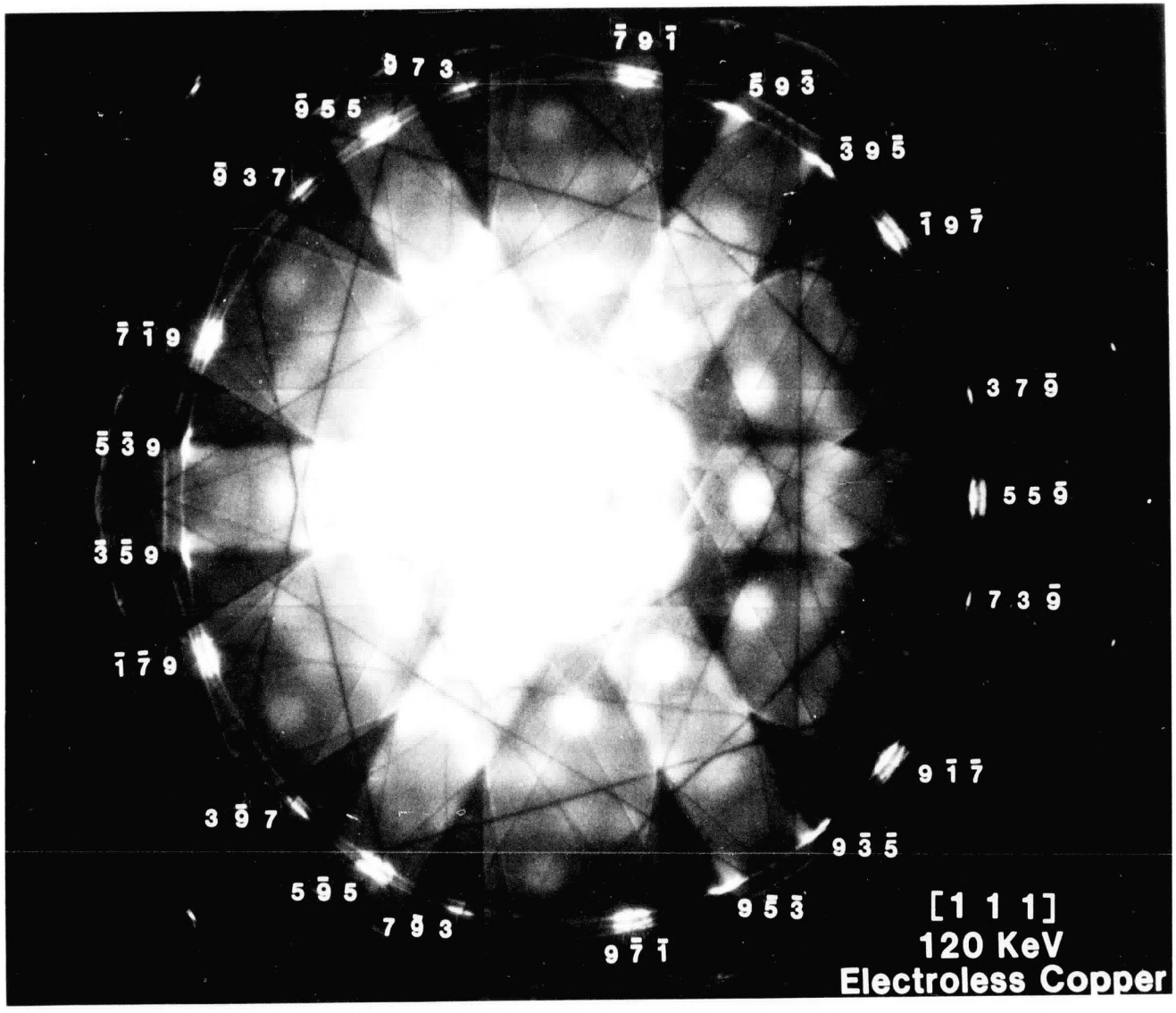
$\bar{7}\,9\,\bar{1}$
$9\,7\,3$
$\bar{5}\,9\,\bar{3}$
$\bar{9}\,5\,5$
$\bar{3}\,9\,\bar{5}$
$\bar{9}\,3\,7$
$\bar{1}\,9\,\bar{7}$
$\bar{7}\,\bar{1}\,9$
$3\,7\,\bar{9}$
$\bar{5}\,\bar{3}\,9$
$5\,5\,\bar{9}$
$\bar{3}\,\bar{5}\,9$
$7\,3\,\bar{9}$
$\bar{1}\,\bar{7}\,9$
$9\,\bar{1}\,\bar{7}$
$3\,\bar{9}\,7$
$9\,\bar{3}\,\bar{5}$
$5\,\bar{9}\,5$
$9\,5\,\bar{3}$
$7\,9\,3$
$9\,7\,\bar{1}$
[1 1 1]
120 KeV
Electroless Copper

magnification image of the central disk of Figure 53 showing the HOLZ lines found in the direct beam of the pattern is shown in Figure 54. Figure 55 is an indexed example of the [111] HOLZ pattern as simulated by a computer.

The lattice parameter of the material, as well as the electron wavelength must be known in order to simulate the HOLZ patterns. From x-ray data, the lattice parameter of copper at room temperature is known to be 0.36150 nm, and this lattice parameter was subsequently used in all simulations for pure copper. The position of the HOLZ lines is dependent on the electron wavelength; since the "effective" electron wavelength varies as a function of crystal orientation, the "effective" electron wavelength for the [111] direction in copper must be determined through simulations. Figures 56a-f are simulated HOLZ patterns for a series of wavelengths ranging from 0.00333 nm to 0.00336 nm. These wavelengths correspond to accelerating voltages of 121.5 kV down to 119.5 kV. Figure 56c is considered most to be similar to the HOLZ pattern for pure copper, therefore, a wavelength of 0.003345 nm, corresponding to an accelerating voltage of 120375 volts, was used in the following simulated [111] patterns for electroless copper specimens.

Residual Strain Determination Through HOLZ Line Analysis

Having determined the "effective" electron wavelength in the [111] orientation, subsequent simulations of HOLZ patterns obtained from electroless copper were performed keeping this wavelength constant and varying the lattice parameter until a good match was obtained. In most cases non-symmetric distortion of the lattice was

Figure 54: A high magnification image of the central disk in Figure 53 showing the HOLZ lines of the diffraction pattern.

Figure 55: A computer simulation of the HOLZ lines of the [111] CBED pattern of Figure 54 with appropriate indexing.

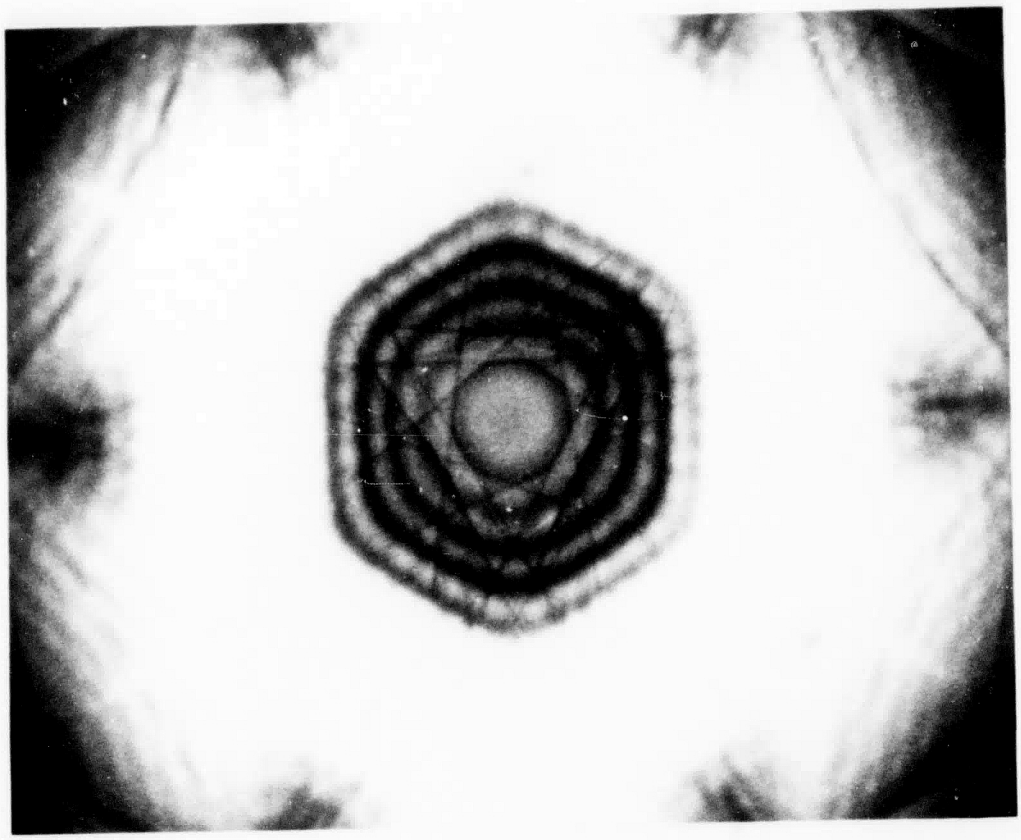

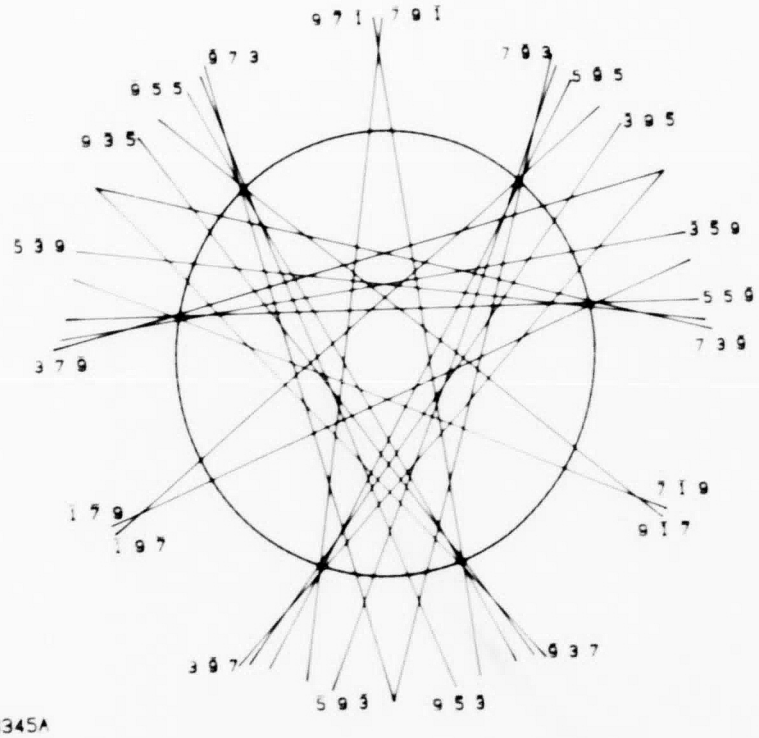

Cu (1 1 1)
a = 3.6150A
LAMBDA = 2.23345A
VOLTAGE = 120KV

Figure 56a-f: A series of computer simulations of HOLZ patterns for a lattice parameter of 0.3615 nm and a range of electron wavelengths (λ=0.00333 nm to λ=0.00336 nm). Figure 56e is considered to give the best math to the experimental pattern of Figure 54.

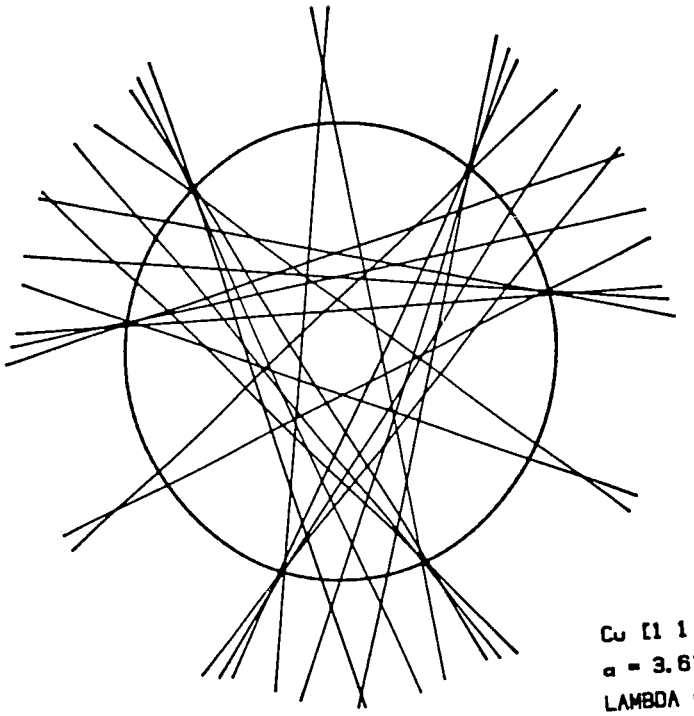

a

Cu [1 1 1]
a = 3.6150A
LAMBDA = 0.0333A
VOLTAGE = 120KV

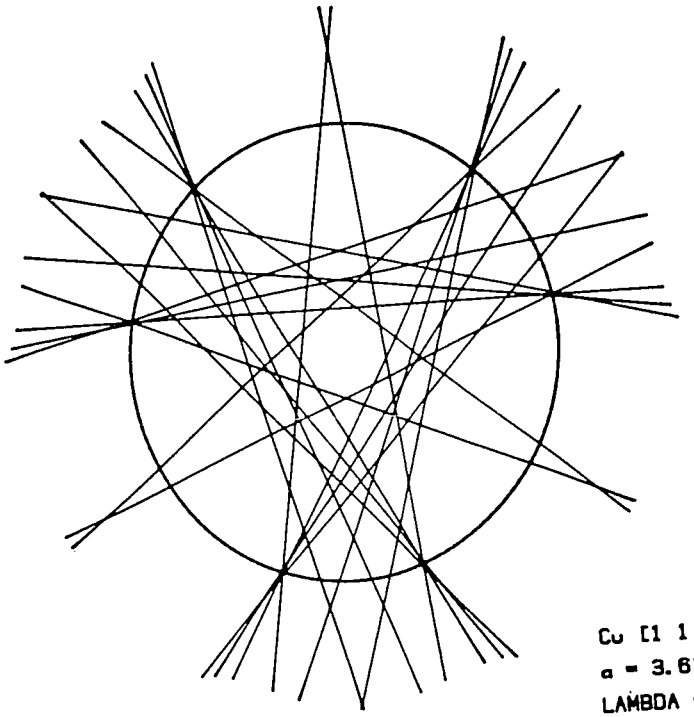

b

Cu [1 1 1]
a = 3.6150A
LAMBDA = 0.0334A
VOLTAGE = 120KV

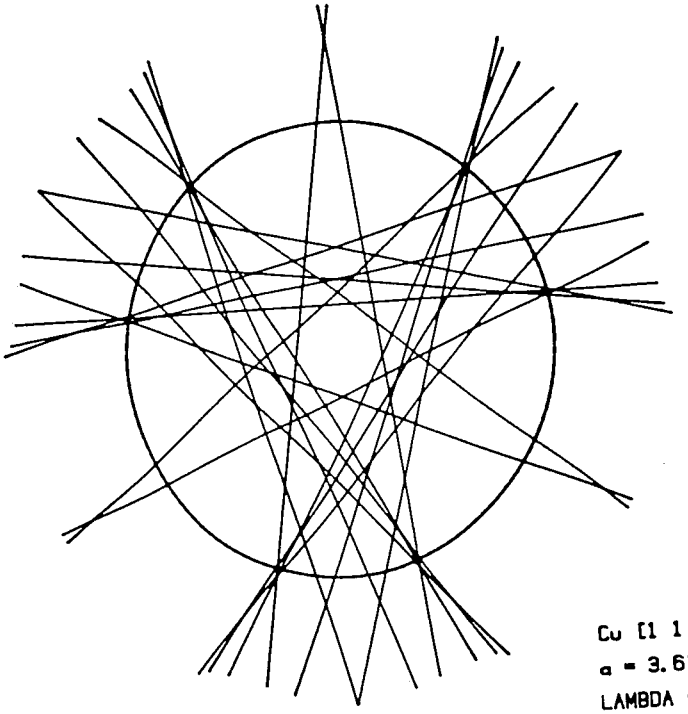

c

Cu [1 1 1]
a = 3.6150A
LAMBDA = 0.03345A
VOLTAGE = 120KV

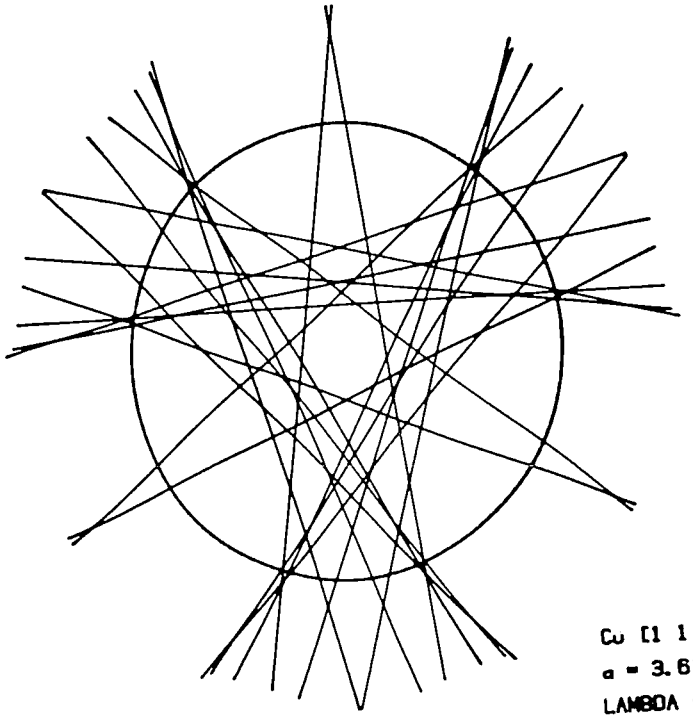

d

Cu [1 1 1]
a = 3.6150A
LAMBDA = 0.0335A
VOLTAGE = 120KV

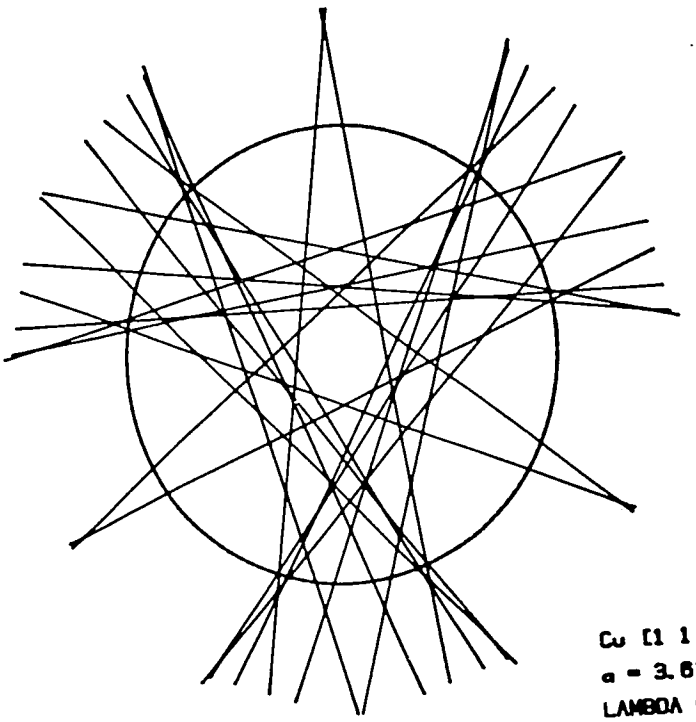

e

Cu [1 1 1]
a = 3.6150A
LAMBDA = 0.03355A
VOLTAGE = 120KV

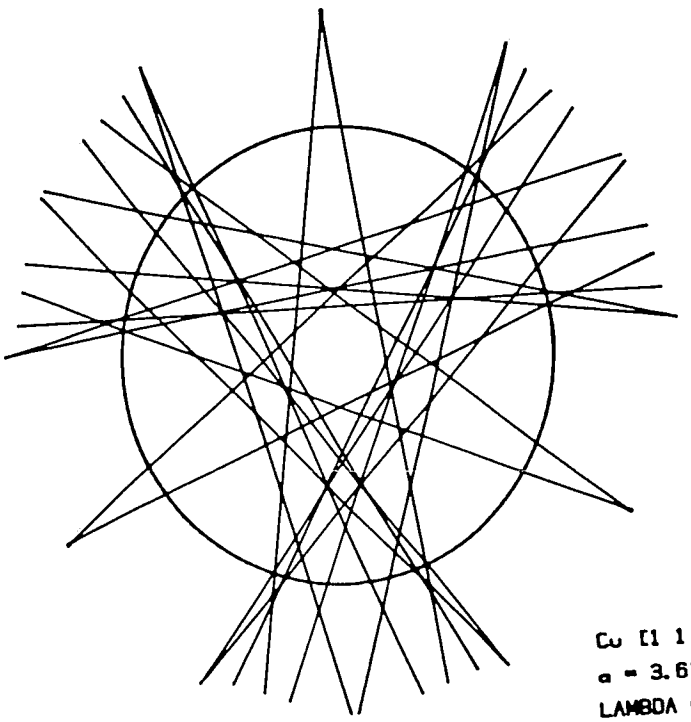

f

Cu [1 1 1]
a = 3.6150A
LAMBDA = 0.0336A
VOLTAGE = 120KV

evident in the HOLZ patterns, and accurate simulation was achieved through independent variation of the lattice constants in each of three unit lattice directions. The degree of asymmetric distortion was evaluated as the degree of tetragonality or c/a ratio required to obtained good simulation matching.

Figure 57a shows a [111] HOLZ pattern taken from a specimen of as-received electroless copper. This HOLZ pattern is representative of 80% (X/N = .8) of the grains analyzed from as-received electroless copper samples. A computer simulated [111] pattern with good matching, shown in Figure 57b, was obtained with a cubic lattice parameter of 0.3615 nm, the lattice parameter of pure copper at room temperature. Therefore, 80% of the grains were considered to possess no detectable lattice strain and the residual stress level could be considered something less than the yield strength of the copper. 20% of the grains analyzed showed small deviations of lattice symmetry, however, these lattice distortions were observed only when analysis was carried out close to grain boundaries where some lattice misfit is expected. These strains were considered insignificant.

In order to evaluate whether lattice strain could actually be detected for small deformation using the HOLZ technique, the following cases were evaluated.

Tensile foils of electroless copper were stressed in uniaxial tension to different degrees of nominal elongation, then unloaded and specimens punched out of the gage center. Figure 58a shows a [111] HOLZ pattern from a foil tested to 0.5% nominal elongation. This HOLZ pattern represents ~60% of the grains analyzed. The patterns showed a

Figure 57a-b: (a) [111] HOLZ pattern taken from as-received electroless copper representative of 80% of the examined grains. (b) A computer simulation [111] pattern showing good matching to (a) achieved through a cubic lattice parameter of 0.3615 nm.

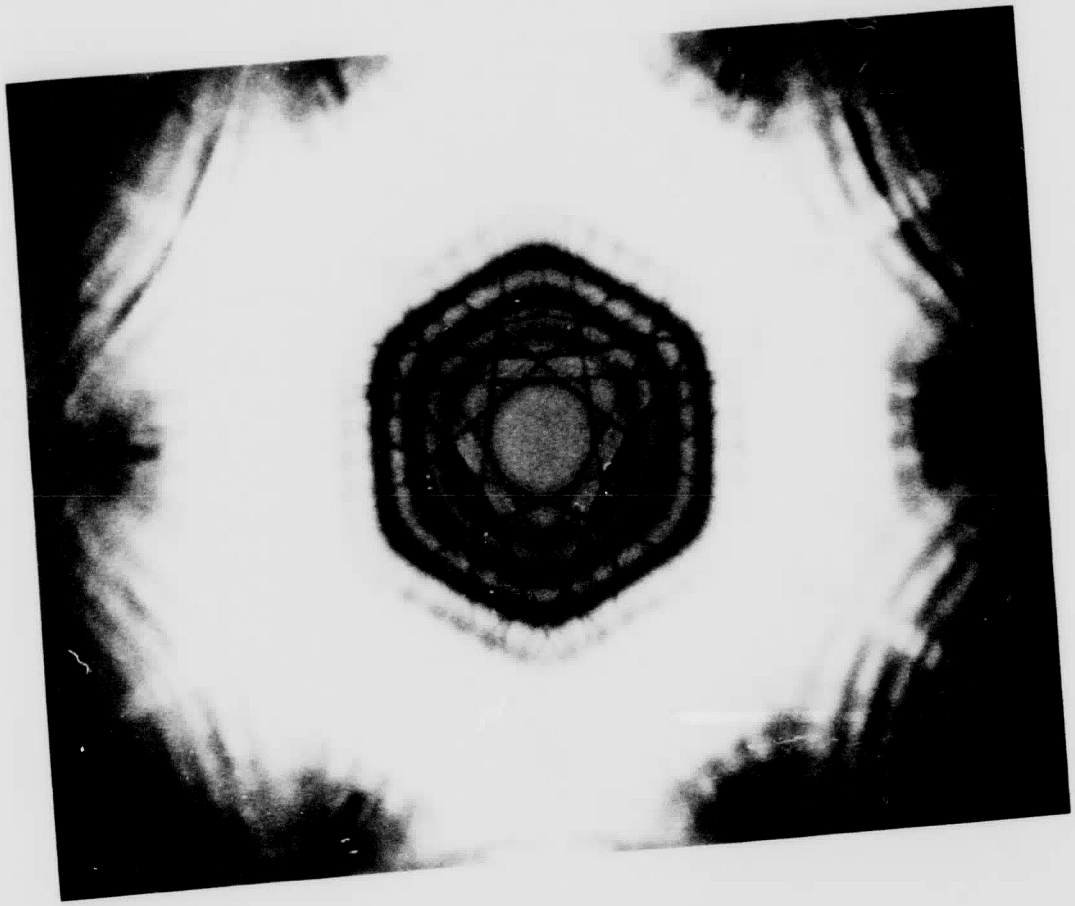

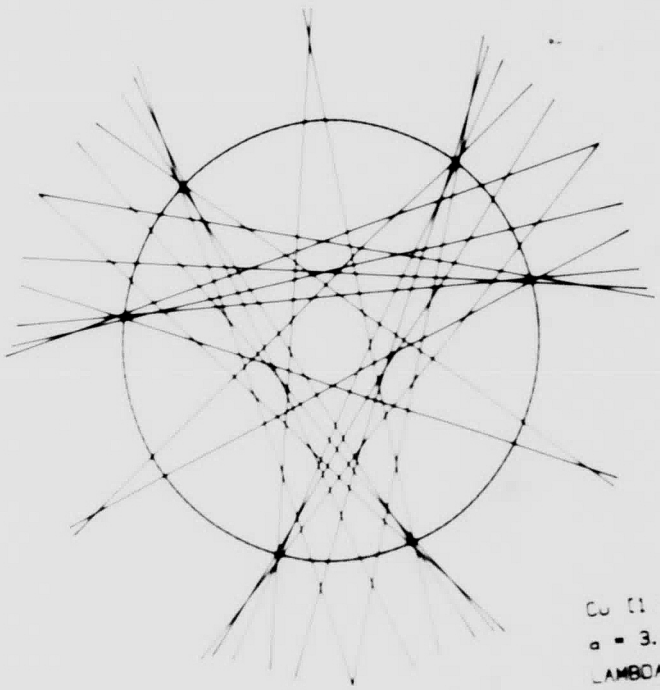

Cu [1 1 1]
a = 3.6150Å
LAMBDA = 0.03345Å
VOLTAGE = 120KV

range of lattice strain as the magnitude of microstrain from one grain to another varies in polycrystalline materials due to crystal orientation. Figure 58b is a computer simulation of Figure 58a in which the c/a ratio of 0.996 was required to produce a good match. Note the asymmetry in one of the three sides of the pattern. It is interesting to note that a 0.5% reduction in one lattice direction produces a tetragonality (c/a) of 0.995, extremely close to the tetragonality observed.

Another foil strained to 2% nominal elongation was analyzed, and Figure 59a shows the [111] HOLZ pattern representative of ∿75% of the grains. Note the increased asymmetry in the HOLZ pattern. Simulation of this pattern, Figure 59b, required a tetragonality of 1.004. In this case two lattice constants were varied in order to obtain good matching. However, it is clear from the frequency and degree of HOLZ pattern changes that small lattice distortions are easily recognized.

The residual strain in the PTH barrel of an actual MIB-PTH was evaluated using the HOLZ technique by sectioning a MIB as shown in Figure 15 and obtaining [111] HOLZ patterns. Figure 60 shows a typical micrograph of the microstructure of PTH barrel. Note the numerous dislocations present in the microstructure. Figure 61a shows a [111] HOLZ pattern representative of ∿70% of the grains analyzed. The HOLZ Pattern is very similar to that of Figure 58a, which was obtained from the 0.5% strained foil. A computer simulation of this pattern is shown in Figure 61b. Since an observable amount of lattice distortion was present in the microstructure of the PTH barrel, the residual stress state can be assumed to be at least the

Figure 58a,b: (a) [111] HOLZ pattern taken from foils tested to 0.5% nominal elongation. The pattern represents 60% of the examined grains. (b) A computer simulated [111] pattern in which a c/a ratio of 0.995 was required to achieve good matching.

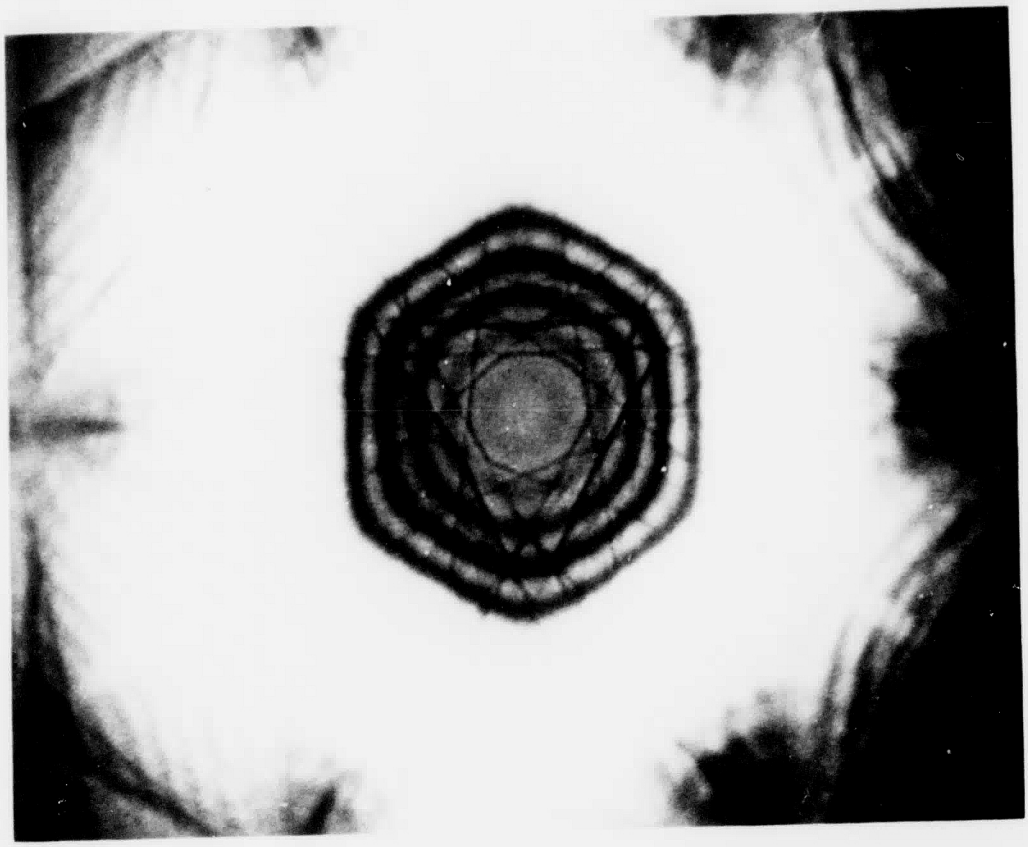

a = 3.6000A
b = 3.6150A
c = 3.6150A

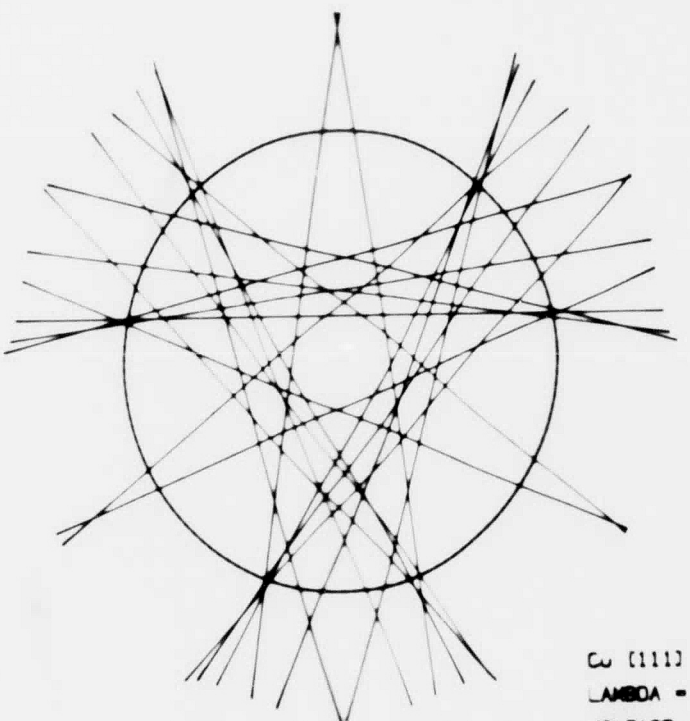

Cu [111]
LAMBDA = 0.03345A
VOLTAGE = 120KV

Figure 59a,b: (a) [111] HOLZ pattern taken from foils tested to 2% nominal elongation. The pattern represents 75% of the examined grains. (b) A computer simulated [111] pattern for which a c/a ratio of 1.004 was required to achieve good matching.

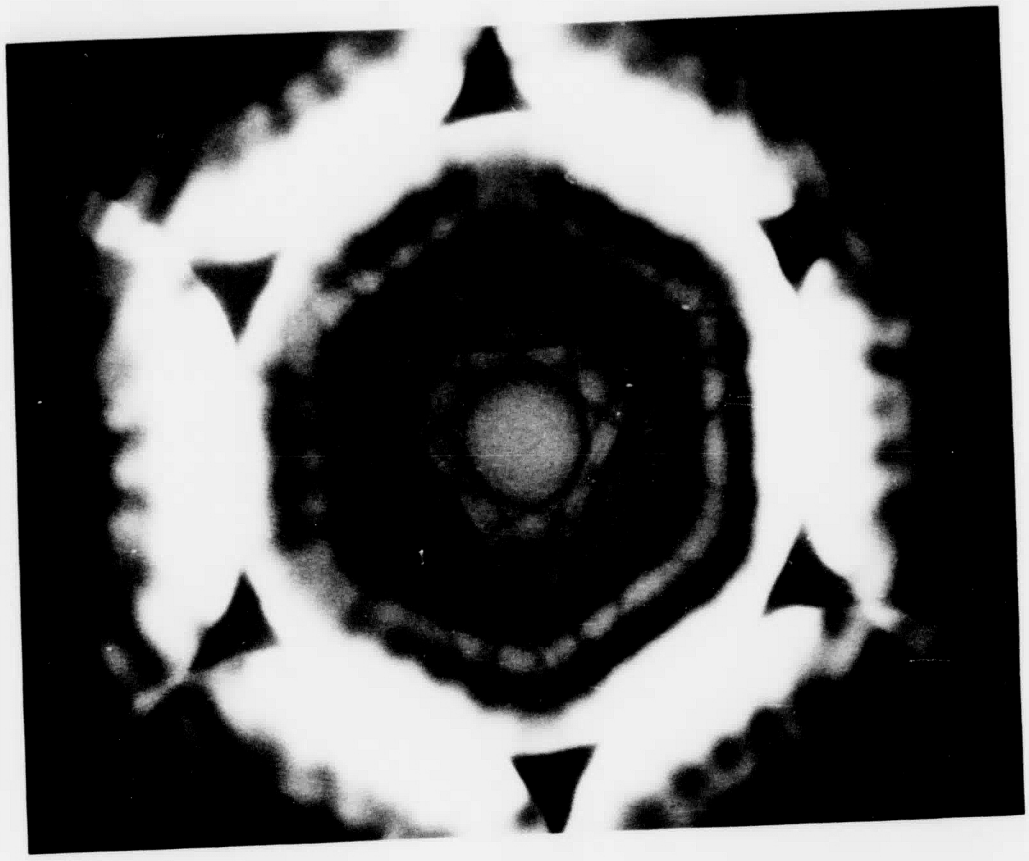

a = 3.6150A
b = 3.6000A
c = 3.6000A

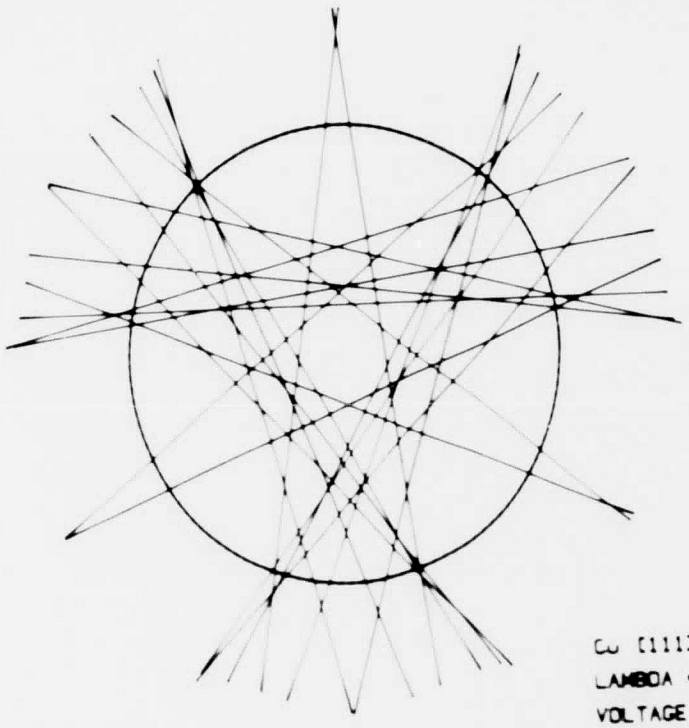

Cu [111]
LAMBDA = 0.03345A
VOLTAGE = 120KV

yield strength of the material. This result verifies the results obtained from the finite element analysis (FEA) of the stress state resulting from the PTH plating process. The FEA study showed that the PTH barrel exists in a state of residual compression in which the stresses are greater than the yield strength of the material.

The results of the HOLZ analysis for the residual strain present in the as-received electroless copper foils indicates that the plating of flat foils does not introduce residual stresses in excess of the yield strength of the copper. This result appears reasonable since there is less thermal expansion coefficient mismatch between the epoxy-glass and the copper in-the-plane of the MIB compared to the through-thickness direction, as with the PTH. These results agree with the internal stress results of Aycock, et al. [9] in which the internal stresses resulting from the plating of electroless copper foils were determined to be ∿50% of the yield strength of the material.

Thus, the residual stress state in these electroless copper foils does not play an important role in determining the ductility of these materials, because in ductile materials, the strain to yield point represents a negligibly small fraction of the total strain to failure. Therefore, residual stresses less than the yield strength of the material have an insignificant influence on the ductility.

Figure 60: TEM micrograph of the typical microstructure of electroless copper in an actual PTH structure. Note the numerous dislocations present in the microstructure.


0.4 μm

Figure 61a,b: (a) [111] HOLZ pattern taken from the copper barrel of the PTH structure. The pattern represents 70% of the examined grains. (b) A computer simulated [111] pattern for which a c/a ratio of ∿0.996 was required to achieve good matching. This pattern is very similar to those obtained for 0.5% nominal elongation samples.

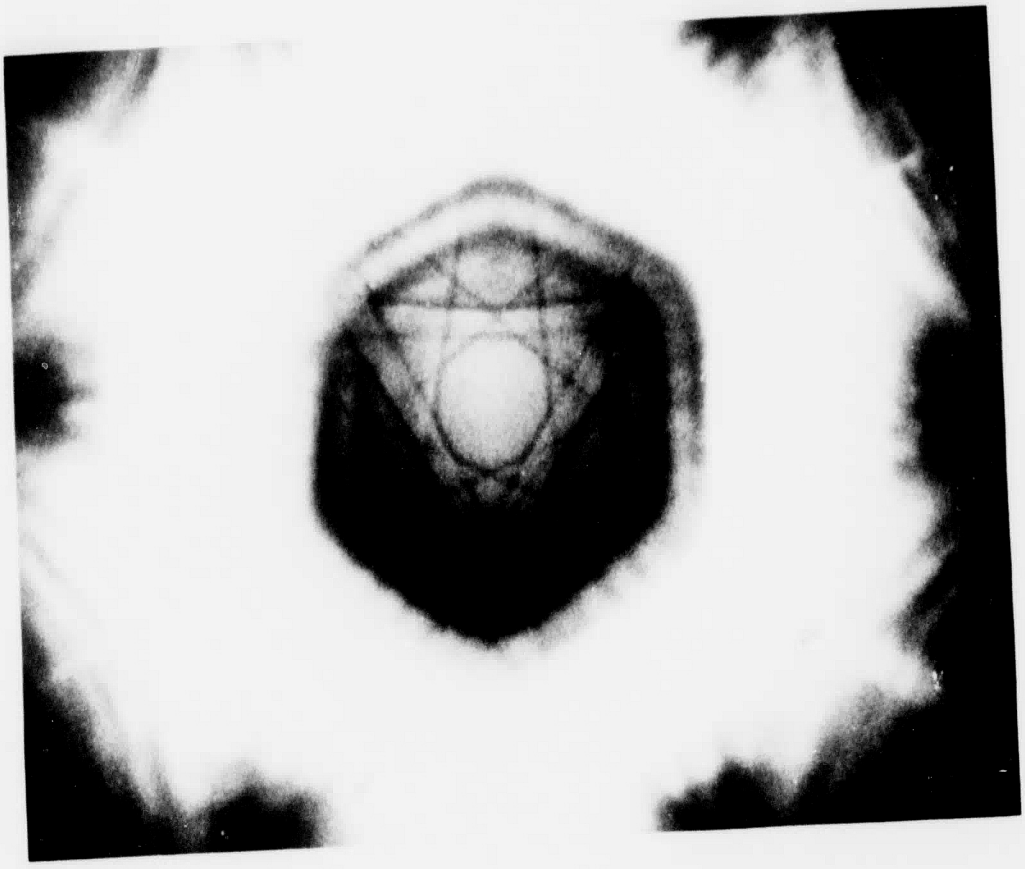

a = 3.6858A
b = 3.6158A
c = 3.6858A

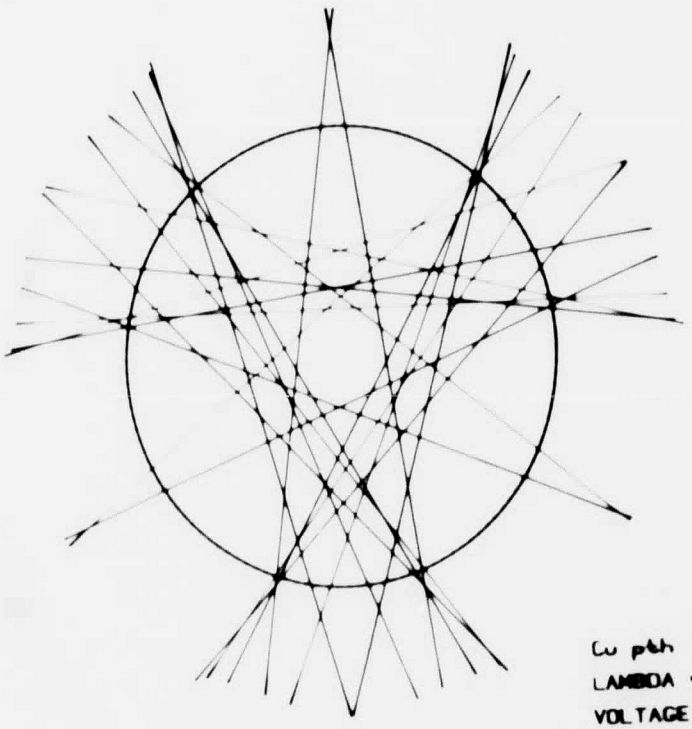

Cu pth [111]
LAMBDA = 0.03345A
VOLTAGE = 120KV

V. CONCLUSIONS

The thermomechanical deformation of electroless copper plated-through-holes (PTHs) in multilayer interconnection boards (MIBs) has been studied in an attempt to predict their long term reliability. A simple analytical model has been developed to evaluate the thermomechanical deformation of plated-through-holes (PTHs) which takes into consideration the geometry of the PTH structure. Based on this model, a simple equation was derived which related the copper PTH barrel stresses and strains to the temperature change introduced into the multilayer interconnection board (MIB).

Finite element analysis of the PTH structure was also conducted which provided information as to local variations in stresses and strains in the copper PTH barrel, in addition to determining the location of the maximum copper stress and strain (i.e. the inside diameter of the barrel, along the MIB centerline). It was determined that as a result of the plating process, the PTH barrels exist in a state of residual compression on the order of the yield strength of copper.

Good agreement was obtained for the average barrel strains calculated from both the analytical model and FEAs. The slightly larger strains obtained from the FEA is considered a result of the asymmetric loading allowed in this technique. The inclusion of an internal copper land in the FEA resulted in local strains considerably greater than the average barrel strain.

Furthermore, the FEA technique was used to evaluate the effect that delamination (along the copper/epoxy-glass interface) has on the

copper barrel strains. A delamination was found to amplify the strains significantly along the region of the delamination.

Tensile tests were conducted on electroless copper foils in order to evaluate their strength and ductility. It was determined that elongation to failure is an inappropriate method for evaluating the ductility of electroless copper foils since local deformations occur along the rough deposit surface; the latter serves to reduce the nominal foil elongation. It would appear that reduction in area at fracture is a better indication of the intrinsic ductility of the electroless deposits.

Tension-tension fatigue tests conducted on electroless copper foils indicated that the foils possess good fatigue resistance when tested in this manner. Furthermore, fatigue striations observed on the fracture surface were used to calculate crack growth rates and crack stress intensities. Striation spacing results showed good agreement with published data for wrought copper.

Cyclic strain fatigue (CSF) experiments were conducted using a specimen designed specifically for modeling the stress distribution in a PTH structure. These tests were conducted to allow critical evaluation of the influence of significant design and material parameters on the long term cyclic life of the PTH. Acoustic emission analysis was performed during each test in the hope of elucidating the mechanisms contributing to the copper barrel failure. The results indicate that the most significant improvement in fatigue life is obtained by reducing the interface surface roughness. The beneficial effects of reduced surface roughness are increased interfacial

strength and reduced stress concentrations. The most detrimental effect on fatigue life resulted when the ductility of the copper was reduced.

The resistance change technique is very useful in monitoring copper cracking, but provides no indication of interface delamination. Acoustic emission on the other hand, provides a good indication of when delamination occurs, but it provides little information as to the cracking process.

It was found that in all cases when delamination occured along the copper/epoxy-glass interface, fatigue resistance was reduced.

The results of the CSF tests were used to derive an expression relating the strain range to the number of strain cycles. This relationship along with the stress analysis results may be used to conservatively predict the life of a PTH.

Scanning electron microscopy was used to evaluate the surface roughness of electroless copper deposits. The surface roughness of these foils constitutes a significant fraction of the foil thickness, and as such, has a significant influence on the mechanical properties of these foils.

The dislocation arrangements resulting from fatigue deformation were observed using transmission electron microscopy. Strain hardening mechanisms were observed to operate in good agreement with previous investigations and no indication of strain hardening deficiencies were noted which may contribute to low ductility in these materials.

Microanalysis of the grain boundaries in electroless copper was carried out in the AEM to determine whether any impurity segregation

was present which may contribute to lower ductility in these materials. No impurity segregation was found to exist; however, it was found that coherent bremsstrahlung (CB) peaks may be generated in the AEM x-ray spectra which may either mask or other peaks, or be misinterpreted as elemental peaks. Careful choice of kV and orientation may minimize the effects of CB, however, the number of grain boundaries available for analysis may be significantly reduced.

Residual strain in electroless copper foils was analyzed using Convergent Beam Electron Diffraction (CBED) and HOLZ line position measurements. It was found that the residual strain in as-received electroless copper foils was negligibly small and did not contribute to reduced ductility. In addition, the observation of significant residual strain in the copper barrel of an actual PTH verifies the FEA results which predicted that the PTH resides in a residual compressive stress state on the order of the yield strength of the material.

From the above discussion it appears that the low ductility of electroless copper based on elongation to failure data maybe an artifact resulting from the fact that localized deformation located at the numerous stress concentrations on the deposit surface reduces the nominal elongation of the gage length. The only evidence of low ductility in these foils is the small elongations to failure. All other evidence such as large reduction in area at fracture, the presence of strain hardening mechanisms, no impurity segregation, and no significant residual strain, indicate that good intrinsic ductility exists in these foils.

VI. SUGGESTIONS FOR FUTURE WORK

This thesis has described both an analytical, as well as a finite element approach to studying the thermomechanical deformation of PTHs in MIBs. However, neither approach attempts to model the physically rough copper/epoxy-glass interface in the PTH. Including a model of this rough surface in either approach should produce more realistic stress-strain results.

A test methodology has been developed here to evaluate the influence of certain design and material variables on the reliability of PTHs. The results of these tests can by no means be completely conclusive due to the relatively small number of samples of each variable which were tested. Further tests should be conducted before the actual influence of each variable can be determined. Also a better understanding of the delamination process may be achieved by incorporating AE technology into currently used interface strength tests such as the peel test.

In addition, the possibility of conducting in-situ SEM fatigue tests of actual PTHs appears attractive for providing useful information as to the micromechanisms of PTH deformation.

REFERENCES

1. Fox, A., "Mechanical Properties at Elevated Temperature of CuBath Electroplated Copper for Multilayer Boards," Journal of Testing and Evaluation, JTEVA, Vol. 4, No. 1, Jan. 1976, pp. 74-84.

2. Oien, M. A., "Methods for Evaluating Plated-Through Hole Reliability," 14th Annual Proceedings, IEEE Reliability Physics Symposium, 1976, pp. 129-131.

3. Oien, M. A., "A Simple Model for the ThermoMechanical Deformations of Plated-Through-Holes in Multilayer Printed Wiring Boards," 14th Annual Proceedings, IEEE Reliability Physics, Symposium, 1976, pp. 121-128.

4. Honma, H. and Mizushima, S., "Applications of Ductile Electroless Copper Deposition of Printed Circuit Boards," Japan Metal Finishing Technology, Vol. 34, 290, Jan. 1983, pp. 47-52.

5. Seraphim, D. P., "A New Set of Printed-Circuit Technologies for the IBM 3081 Processor Unit," IBM Journal of Research and Development, Vol. 26, No. 1, Jan. 1982, pp. 37-44.

6. Rudy, D. A., "The Detection of Barrel Cracks in Plated Through Holes Using Four Point Resistance Measurements," 14th Annual Proceedings, IEEE Reliability Symposium 1976, pp. 135-140.

7. Ammann, H. H. and Jocher, R. W., "Measurement of Thermo-Mechanical Strains in Plated-Through-Holes," 14th Annual Proceedings, IEEE Reliability Physics Symposium, 1976

8. Anderson, R. and Wild, R., "TEM Analysis of Printed Circuit Board Copper Foil," Thirty-Eighth Annual EMSA Meeting, 1980, pp. 408-409.

9. Aycock, T. L., et al., "The Effects of Stabilizing Additives on the Microstructure and Properties of Electroless Copper Deposits," Metallurgical Transactions, Vol. 5, May 1974, pp. 1215-1223.

10. Okinaka, Y. and Nakahara, S., "Microstructure and Ductility of Electroless Copper Deposits," Acta Metall., Vol. 31, No. 5, pp. 713-724.

11. Okinaka, Y. and Nakahara, S., "Hydrogen Embrittlement of Electroless Copper Deposits," Journal of the Electrochemical Society, April 1976, pp. 475-478.

12. Homma, H. and Saito, K., Kinhyo-shi, 29, 88 (1978).

13. Ogura, T., Makino, A. and Masumoto, "Comparison of Auger Electron Spectroscopy and Etching Method for Analysis of Grain Boundary Segregation of Phosphorus," Scripta Met., Vol. 14, 1980, p. 887.

14. Westbrook, J. H., Met. Rev., "Segregation at Grain Boundaries," Vol. 9, 1964, p. 415.

15. Cliff, G. and Lorimer, G. W., "The Quantitative Analysis of Thin Specimens," J. of Microscopy, Vol. 103, 1975, p. 203.

16. Baumann, S. F. and Williams, D. B., "A STEM X-ray Microanalytical Study of the Equilibrium Segregation of Bismuth in Copper," Journal of Microscopy, Vol. 123, 1981, p. 299.

17. Michael, J. R. and Williams, D. B., "An Analytical Electron Microscope Study of the Kinetics of the Equilibrium Segregation of Bismuth in Copper," Metallurgical Transactions, Vol. 15A, Jan. 1984, pp. 99-105.

18. Doig, P. and Flewitt, P. E. J., "Microanalysis of Grain Boundary Segregation in Embrittled Iron-3 wt% Nickel Alloys Using STEM," J. of Microscopy, Vol. 112, 1978, p. 257.

19. Doig, P., Flewitt, P. E. J. and Wild, R. K., " Comparison of X-ray (STEM) and Auger Electron Spectroscopy for Microanalysis of Grain Boundary Segregation," Phil. Mag. A, Vol. 37, 1978, p. 759.

20. Doig, P., Lonsdale, D. and Flewitt, P. E. J., "X-ray Microanalysis of Grain Boundary Segregations in Steels Using the Scanning Transmission Electron Microscope," Metallurgical Transactions, Vol. 12, 1981, p. 1277-1282.

21. Goldstein, J. I., "Principles of Thin Film X-ray Microanalysis," Introduction to Analytical Electron Microscopy, J. J. Hren, J. I. Goldstein and D. C. Joy, eds., Plenum Press, New York, 1979, pp. 87-120.

22. Joshi, A. and Stein, D. F., "Auger Spectroscoic Analysis of Bismuth Segregated to Grain Boundaries in Copper," J. Inst. Met., Vol. 99, 1971, p. 178.

23. Powell, B. D. and Mykura, H., "Segregation of Bismuth to Grain Boundaries in Copper Bismuth Alloys," Acta Metall., Vol. 21, 1973, p. 1151.

24. Powell, B. D. and Woodruff, D. P., "Anisotropy in Grain Boundary Segregation in Copper Bismuth Alloys," Phil. Mag., Vol. 34, 1976, p. 169.

25. Seah, M. P. and Hondros, E. D., "Grain Boundary Segregation," Proc. Royal Microscopical Society London A, Vol. 335, 1973, p. 191.

26. Ecob, R. C.,Shaw, M. P., Porter, A. J. and Ralph, B, "The Application of Convergent-Beam Detector Diffraction to the Detection of Small Symmetry Changes Accompanying Phase Transformations, I. General and Methods," Phil. Mag. A, Vol. 44, 1981, pp. 1117-1133.

27. Jones, P. M., Rackham, G. M. and Steeds, J. W., "Higher Order Laue Zone Effects in Electron Diffraction and Their Use in Lattice Parameter Determination," Proc. Royal Microscopical Society London A, Vol. 354, 1977, pp. 197-222.

28. Ecob, R. C., Ricks, R. A. and Porter, A. J., "The Measurement of Precipitate/Matrix Lattice Mismatch in Nickel-Base Superalloys," Scripta Metall., Vol. 16, 1982, pp. 1085-1090.

29. Sarikaya, M., Thomas, G. and Steeds, J. W., "Solute Element Partitioning and Austenite Stabilization in Steels," Prov. International Conference on Solid-Solid Phase Transformations, H. I. Aaronson, ed., The Metallurgical Society of AIME, 1981, pp. 1421-1425.

30. IBM Confidential Report, "Reliability Investigation of Multilayer Interconnection Boards (MIBs)," AD689845, Contract No. F30602-68-C-0019, Section XI, pp. 72-87.

31. Goldstein, J. I., et al., "Image Formation in the Scanning Electron Microscope," Scanning Electron Microscopy and X-ray

Microanalysis, J. I. Goldstein, et al., eds., Plenum Press, New York, 1981, pp. 143-146.

32. Boyde, A., "Quantitative Photogrammetric Analysis and Qualitative Stereoscopic Analysis of SEM Images," J. of Microscopy, Vol. 98, Pt. 3, August 1973, pp. 432-471.

33. Thompson, M. N., et al., "The Influence of Foil Thickness on X-ray Count Rates in STEM Microanalysis," Phil. Mag., Vol. 35, 1977, pp. 1537-1542.

34. Vecchio, K. S., "The Effects of Coherent Bremsstrahlung Peaks in AEM Studies of Grain Boundary Segregation," accepted for publication by the Electron Microscopy Society of America, 1985.

35. Carpenter R. W. and Spence, J. C. H., "Three-Dimensional Strain-Field Information in Convergent-Beam Electron Diffraction Patterns," Acta. Cryst., Vol. A38, 1982, pp. 55-61.

36. Porter, A. J., Shaw, M. P., Ecob, R. C. and Ralph, B., "The Application of Convergent Beam Electron Diffraction to the Detection of Small Symmetry Changes Accompanying Phase Transformations, II. Recrystallization of Superalloys," Phil. Mag. A, Vol. 44, No. 5, 1981, pp. 1135-1148.

37. Williams, D. B., Practial Analytical Electron Microscopy in Materials Science, Philips Electron Optics Publishing Group, New Jersey, 1984, p. 124.

38. Ibid, pp. 127-138.

39. Bates, R. C. and Clark, W. G. Jr., "Fractography and Fracture Mechanics," Trans. Quart., ASM, Vol. 62, No. 2, 1969, p. 380.

40. Speidel, M. O., "Fatigue Crack Growth at High Temperatures," High Temperature Materials in Gas Turbines, Elsevier Scientific Publishing Co., Amsterdam, 1974, p. 212.

41. Lee, L. C., Darekar, V. S. and Lim, C. K., "Micromechanisms of Multilayer Printed Circuit Boards," IBM J. Res. Develop., Vol. 28, No. 6, Nov. 1984, pp. 711-718.

42. Snowden, K. U., 5th International Conference on Electron Microscopy, Philadelphia, J-7, 1962.

43. Snowden, K. U., "Dislocation Arrangements During Cyclic Hardening and Softening in Al Crystals," Acta Metall., Vol. 11, July 1963, p. 675-684.

44. Johari, O. and Thomas, G., "Factors Affecting Dislocation Substructures in Deformed Copper," Acta Metall., Vol. 12, No.5, May 1964, pp. 679-682.

45. Michael, J. R., M.S. Thesis, Lehigh University, 1981.

46. Reese, G. M., et al., "Coherent Bremsstrahlung from Kilovolt Electrons in Zone Axis Orientations," Phil. Mag. A, Vol. 49, No. 5, 1984, pp. 697-716.

47. Spence, J. C. H., et al., "Coherent Bremsstrahlung Peaks in X-ray Microanalysis Spectra," Phil Mag. B, Vol. 48, 1983, pp. L39-L43.

48. Kurizki, G. and McIver, J. K., "Crystal Potential Periodicity Effects on the Dynamics of Fast Charged Particles and Their Emission of Radiation," Phys. Letters A, Vol. 89, 1982, p. 43.

49. Spence, J. C. H., private communication, 1984.

APPENDIX I

DEFLECTED STRUCTURE. IDEALIZATION #1 $\Delta T = -52°C$

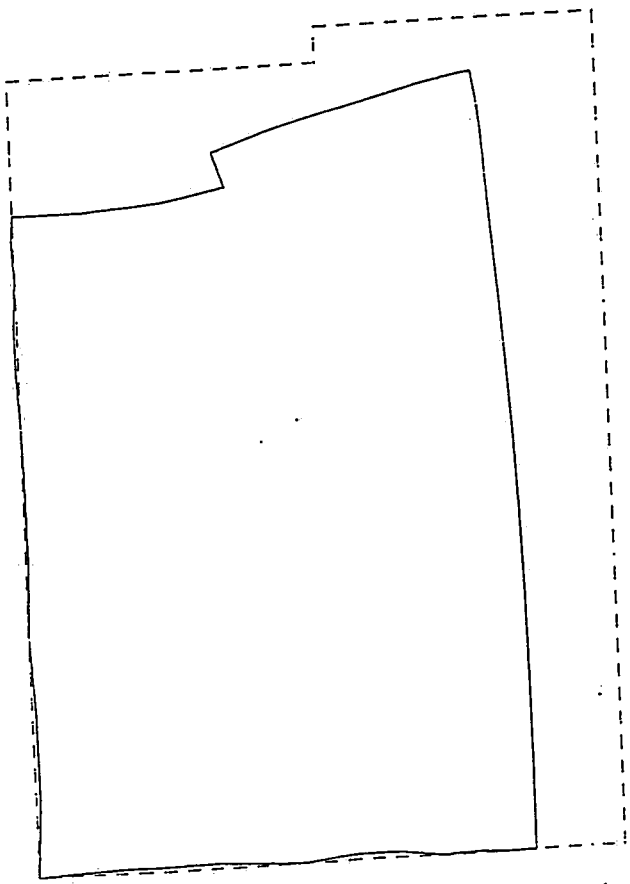

CONTOUR VALUES Y STRESSES IDEALIZATION #1 ΔT = -52°C

1--	-.22E+05
2--	-.20E+05
3--	-.18E+05
4--	-.16E+05
5--	-.14E+05
6--	-.13E+05
7--	-.11E+05
8--	-.90E+04
9--	-.72E+04
10--	-.53E+04
11--	-.35E+04
12--	-.17E+04
13--	.15E+03
14--	.20E+04
15--	.38E+04
16--	.56E+04
17--	.75E+04
18--	.93E+04
19--	.11E+05
20--	.13E+05
21--	.15E+05

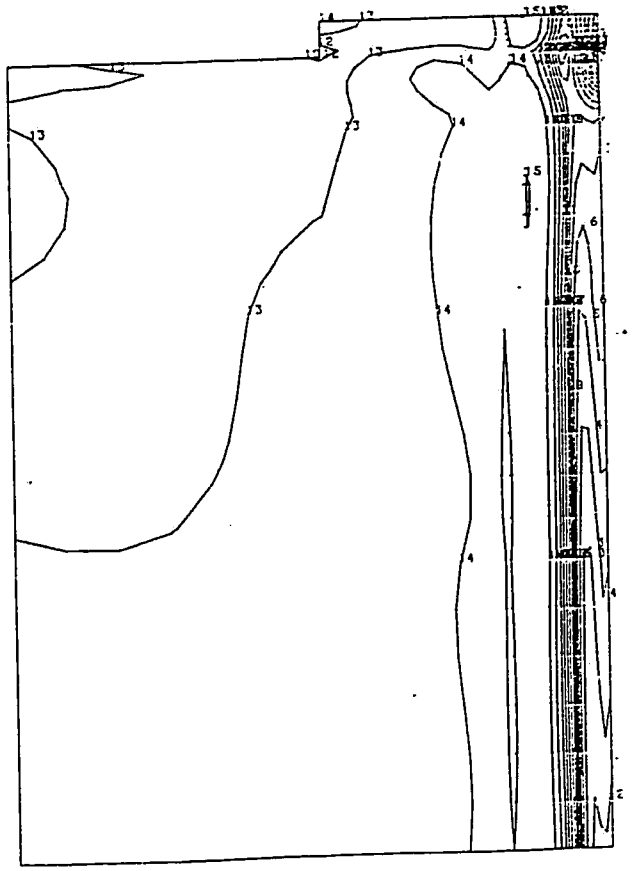

CONTOUR VALUES VON MISES STRESSES IDEALIZATION #1 $\Delta T = -52°C$

1--	.20E+03
2--	.12E+04
3--	.23E+04
4--	.33E+04
5--	.44E+04
6--	.54E+04
7--	.65E+04
8--	.75E+04
9--	.86E+04
10--	.96E+04
11--	.11E+05
12--	.12E+05
13--	.13E+05
14--	.14E+05
15--	.15E+05
16--	.16E+05
17--	.17E+05
18--	.18E+05
19--	.19E+05
20--	.20E+05
21--	.21E+05

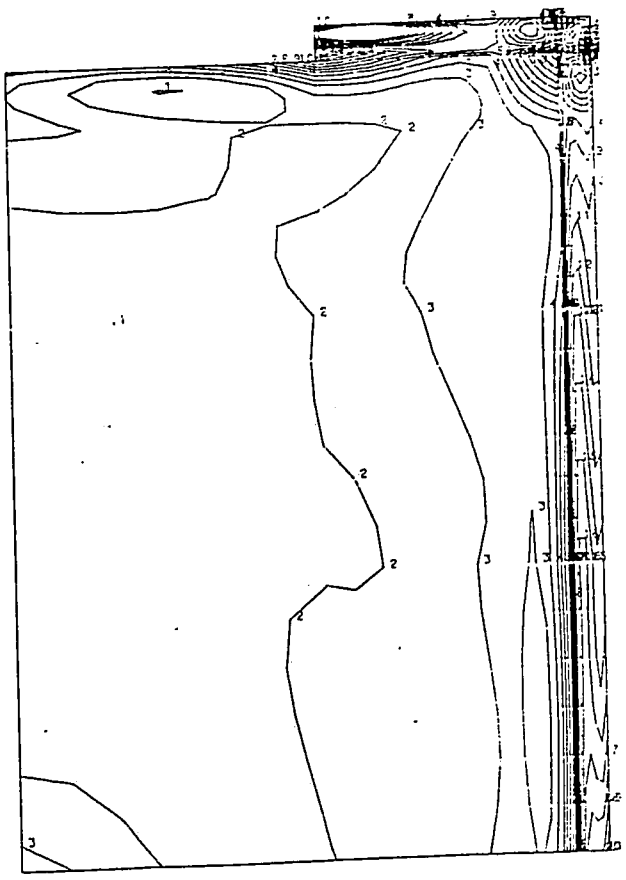

DEFLECTED STRUCTURE IDEALIZATION #1 $\Delta T = +10°C$

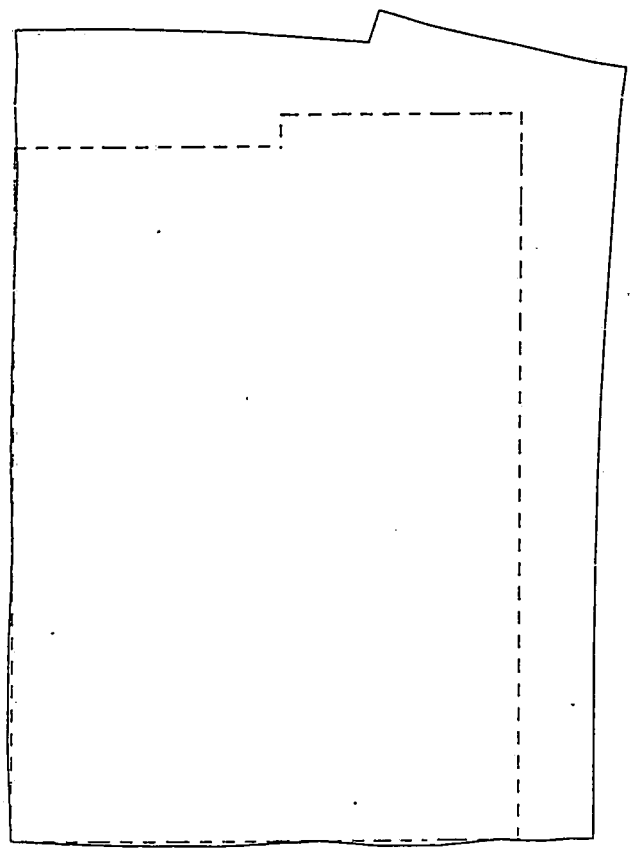

CONTOUR VALUES VON MISES STRESSES IDEALIZATION #1 ΔT = +10°C

1--	.39E+02
2--	.24E+03
3--	.44E+03
4--	.64E+03
5--	.84E+03
6--	.10E+04
7--	.12E+04
8--	.14E+04
9--	.16E+04
10--	.18E+04
11--	.21E+04
12--	.23E+04
13--	.25E+04
14--	.27E+04
15--	.29E+04
16--	.31E+04
17--	.33E+04
18--	.35E+04
19--	.37E+04
20--	.39E+04
21--	.41E+04

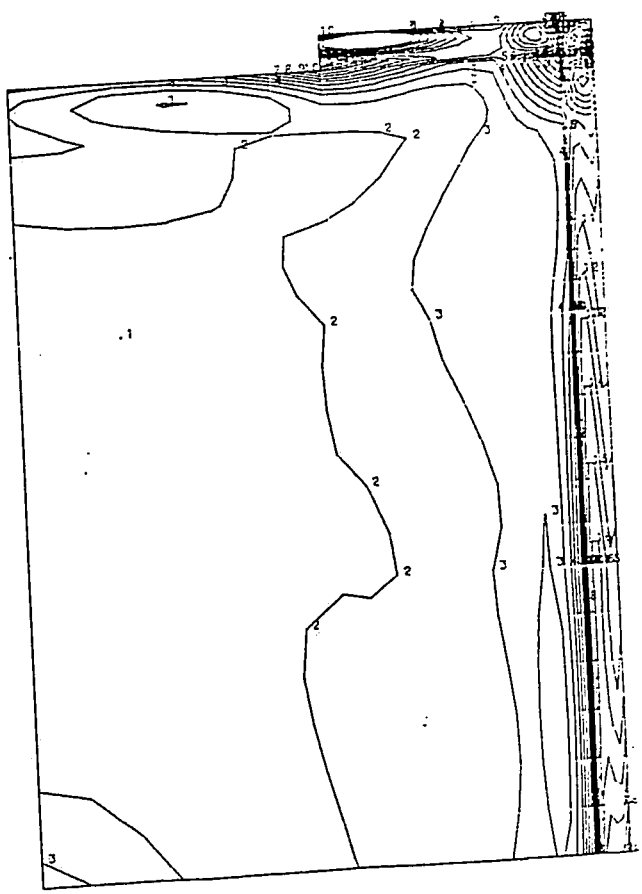

CONTOUR VALUES Y STRESSES IDEALIZATION #1 ΔT = +10°C

1--	-.28E+04
2--	-.25E+04
3--	-.21E+04
4--	-.18E+04
5--	-.14E+04
6--	-.11E+04
7--	-.73E+03
8--	-.38E+03
9--	-.28E+02
10--	.32E+03
11--	.68E+03
12--	.10E+04
13--	.14E+04
14--	.17E+04
15--	.21E+04
16--	.24E+04
17--	.28E+04
18--	.31E+04
19--	.35E+04
20--	.38E+04
21--	.42E+04

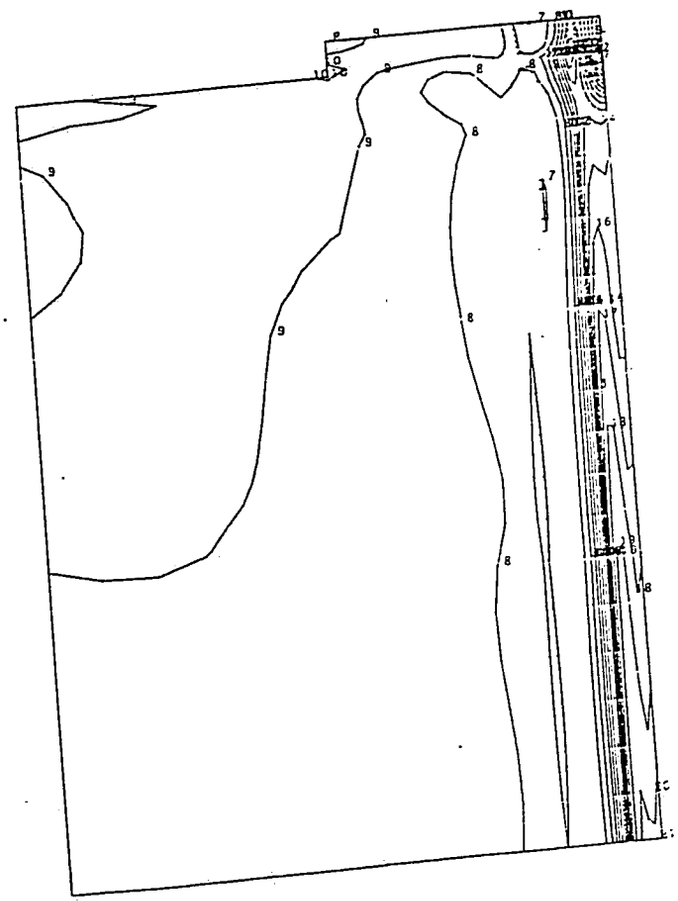

DEFLECTED STRUCTURE IDEALIZATION #1 $\Delta T = +20°C$

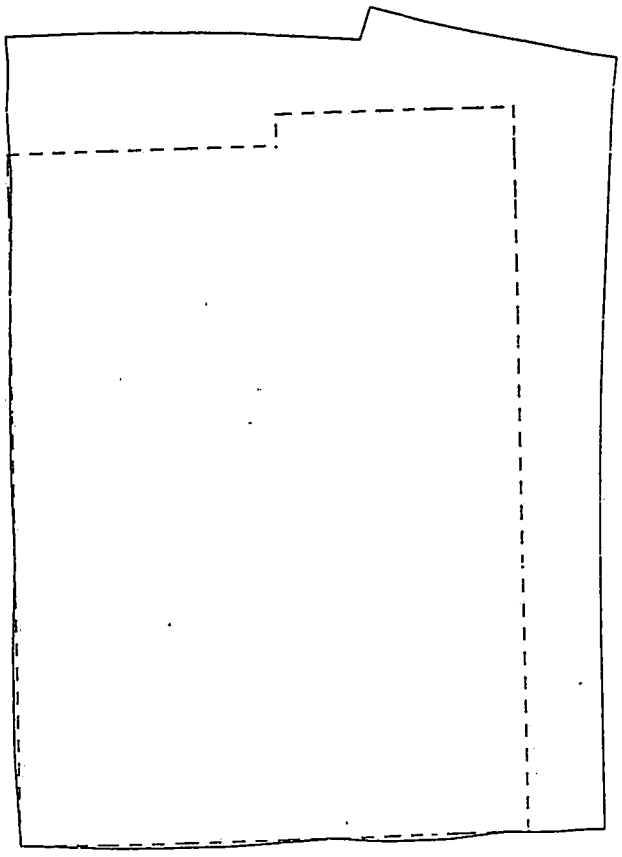

CONTOUR VALUES VON MISES STRESSES IDEALIZATION #1 ΔT = +20°C

1--	.77E+02
2--	.48E+03
3--	.88E+03
4--	.13E+04
5--	.17E+04
6--	.21E+04
7--	.25E+04
8--	.29E+04
9--	.33E+04
10--	.37E+04
11--	.41E+04
12--	.45E+04
13--	.49E+04
14--	.53E+04
15--	.57E+04
16--	.61E+04
17--	.65E+04
18--	.69E+04
19--	.73E+04
20--	.77E+04
21--	.81E+04

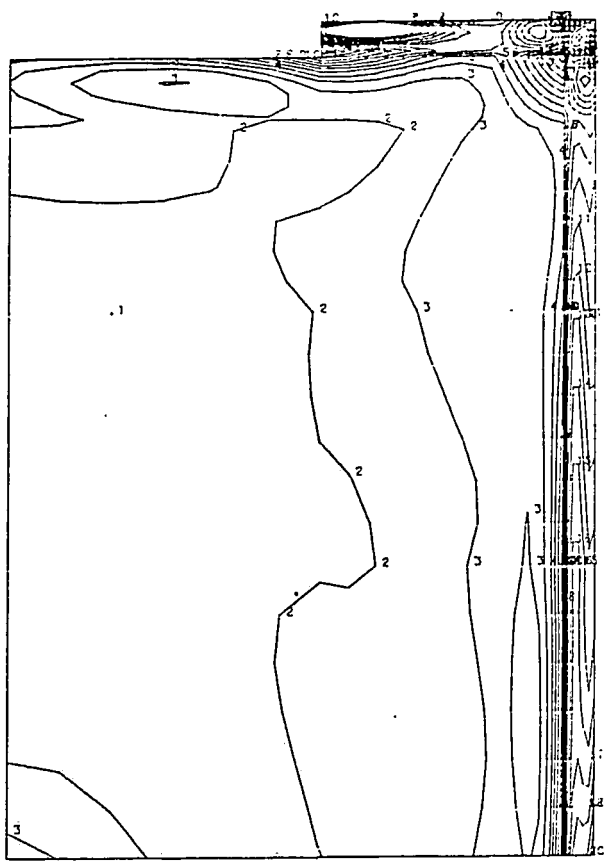

CONTOUR VALUES Y STRESSES IDEALIZATION #1 ΔT = +20°C

1--	-.57E+04
2--	-.50E+04
3--	-.43E+04
4--	-.36E+04
5--	-.29E+04
6--	-.22E+04
7--	-.15E+04
8--	-.76E+03
9--	-.56E+02
10--	.65E+03
11--	.14E+04
12--	.21E+04
13--	.28E+04
14--	.35E+04
15--	.42E+04
16--	.49E+04
17--	.56E+04
18--	.63E+04
19--	.70E+04
20--	.77E+04
21--	.84E+04

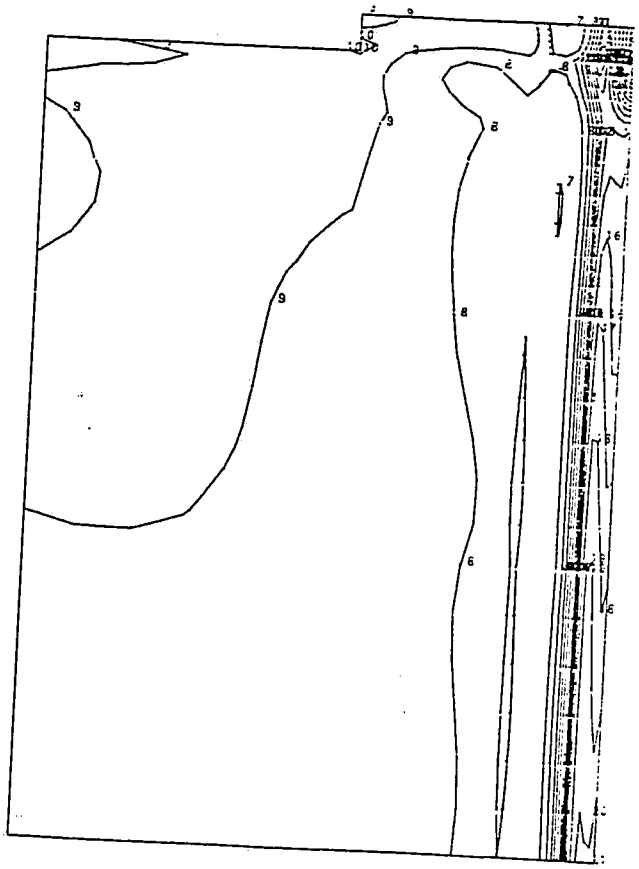

DEFLECTED STRUCTURE IDEALIZATION #1 ΔT = +30°C

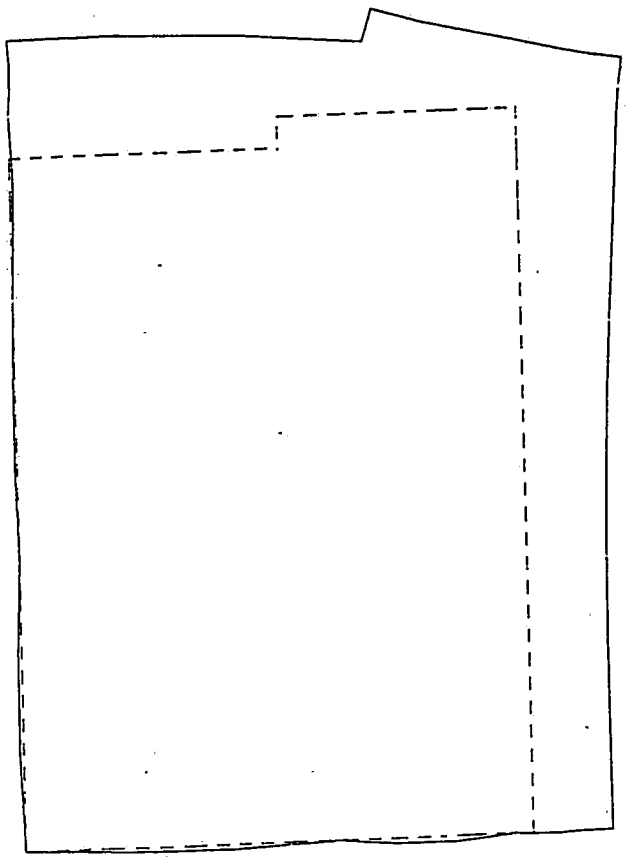

CONTOUR VALUES VON MISES STRESSES IDEALIZATION #1 ΔT = +30°C

1--	.12E+03
2--	.72E+03
3--	.13E+04
4--	.19E+04
5--	.25E+04
6--	.31E+04
7--	.37E+04
8--	.43E+04
9--	.49E+04
10--	.55E+04
11--	.62E+04
12--	.68E+04
13--	.74E+04
14--	.80E+04
15--	.86E+04
16--	.92E+04
17--	.98E+04
18--	.10E+05
19--	.11E+05
20--	.12E+05
21--	.12E+05

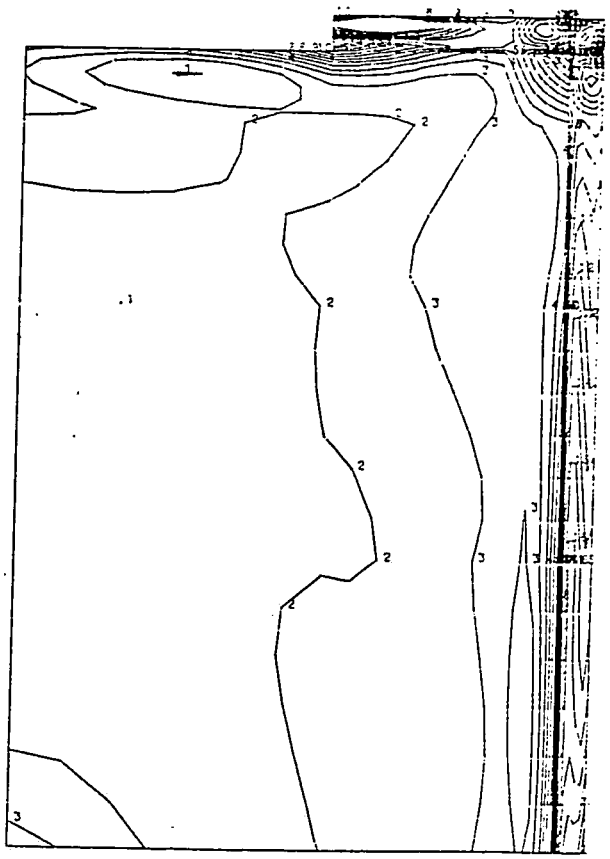

CONTOUR VALUES Y STRESSES IDEALIZATION #1 ΔT = +30°C

1--	-.85E+04
2--	-.75E+04
3--	-.64E+04
4--	-.54E+04
5--	-.43E+04
6--	-.33E+04
7--	-.22E+04
8--	-.11E+04
9--	-.85E+02
10--	.97E+03
11--	.20E+04
12--	.31E+04
13--	.41E+04
14--	.52E+04
15--	.62E+04
16--	.73E+04
17--	.84E+04
18--	.94E+04
19--	.10E+05
20--	.12E+05
21--	.13E+05

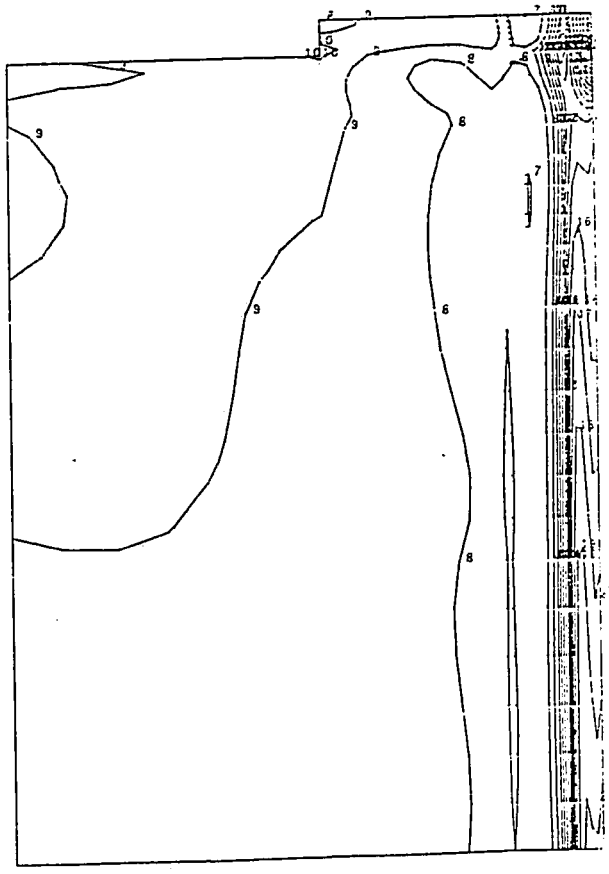

DEFLECTED STRUCTURE IDEALIZATION #2 $\Delta T = -52°C$

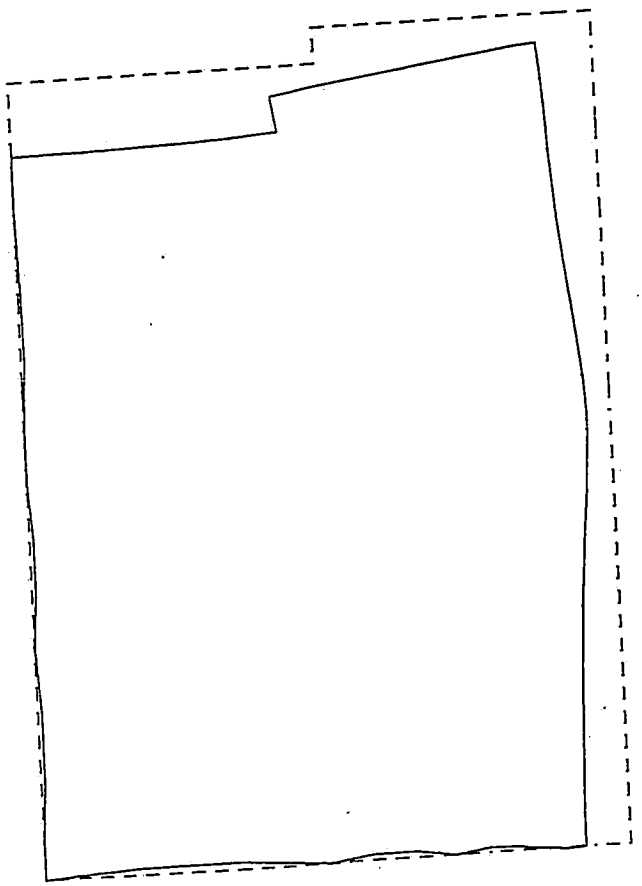

CONTOUR VALUES VON MISES STRESSES IDEALIZATION #2 $\Delta T = -52°C$

1--	.45E+03
2--	.43E+04
3--	.81E+04
4--	.12E+05
5--	.16E+05
6--	.20E+05
7--	.23E+05
8--	.27E+05
9--	.31E+05
10--	.35E+05
11--	.39E+05
12--	.42E+05
13--	.46E+05
14--	.50E+05
15--	.54E+05
16--	.58E+05
17--	.61E+05
18--	.65E+05
19--	.69E+05
20--	.73E+05
21--	.77E+05

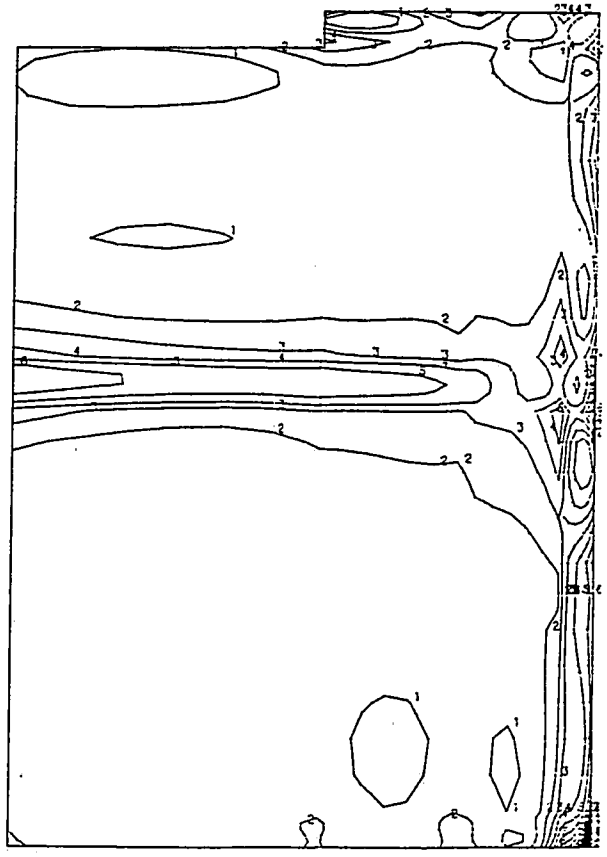

CONTOUR VALUES Y STRESSES IDEALIZATION #2 ΔT = -52°C

1--	-.54E+05
2--	-.50E+05
3--	-.46E+05
4--	-.41E+05
5--	-.37E+05
6--	-.32E+05
7--	-.28E+05
8--	-.24E+05
9--	-.19E+05
10--	-.15E+05
11--	-.11E+05
12--	-.63E+04
13--	-.20E+04
14--	.24E+04
15--	.67E+04
16--	.11E+05
17--	.15E+05
18--	.20E+05
19--	.24E+05
20--	.28E+05
21--	.33E+05

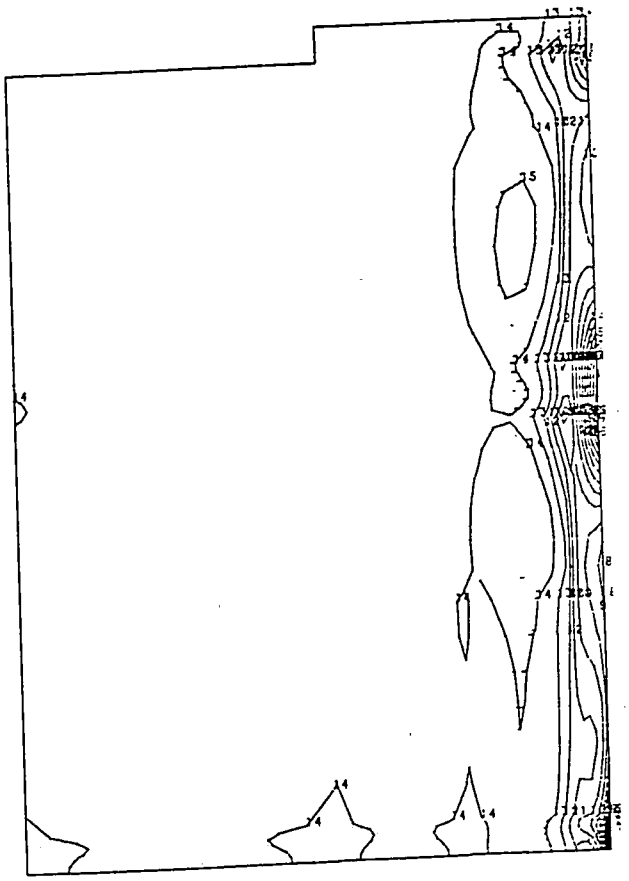

DEFLECTED STRUCTURE IDEALIZATION #2 $\Delta T = +10°C$

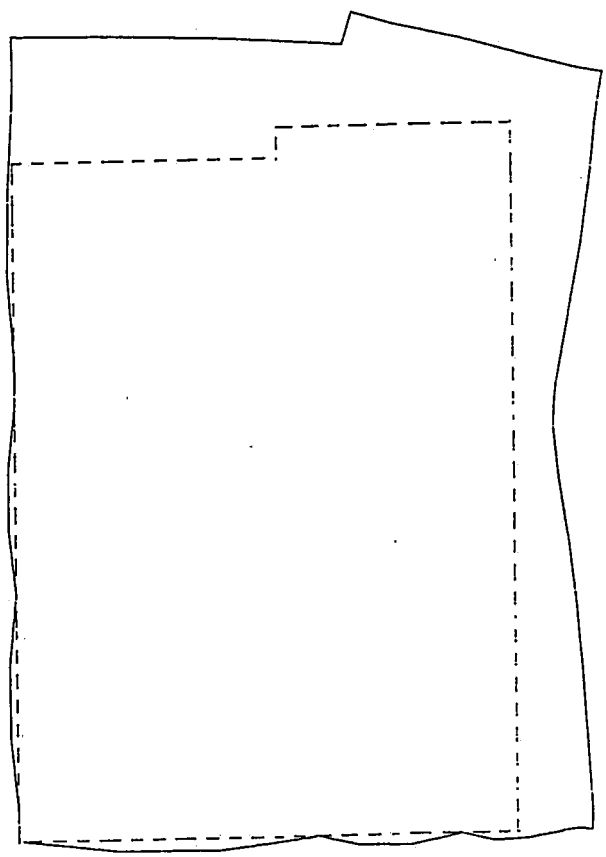

CONTOUR VALUES VON MISES STRESSES IDEALIZATION #2 ΔT = +10°C

1--	.87E+02
2--	.82E+03
3--	.16E+04
4--	.23E+04
5--	.30E+04
6--	.38E+04
7--	.45E+04
8--	.52E+04
9--	.60E+04
10--	.67E+04
11--	.74E+04
12--	.82E+04
13--	.89E+04
14--	.96E+04
15--	.10E+05
16--	.11E+05
17--	.12E+05
18--	.13E+05
19--	.13E+05
20--	.14E+05
21--	.15E+05

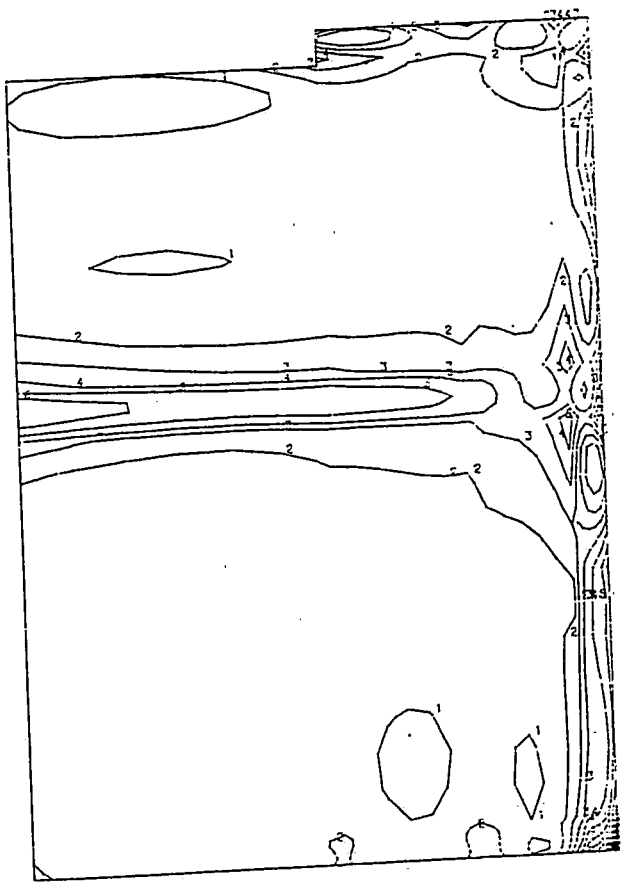

CONTOUR VALUES Y STRESSES IDEALIZATION #2 ΔT = +10°C

1--	-.63E+04
2--	-.55E+04
3--	-.46E+04
4--	-.38E+04
5--	-.30E+04
6--	-.21E+04
7--	-.13E+04
8--	-.45E+03
9--	.38E+03
10--	.12E+04
11--	.21E+04
12--	.29E+04
13--	.37E+04
14--	.46E+04
15--	.54E+04
16--	.62E+04
17--	.71E+04
18--	.79E+04
19--	.88E+04
20--	.96E+04
21--	.10E+05

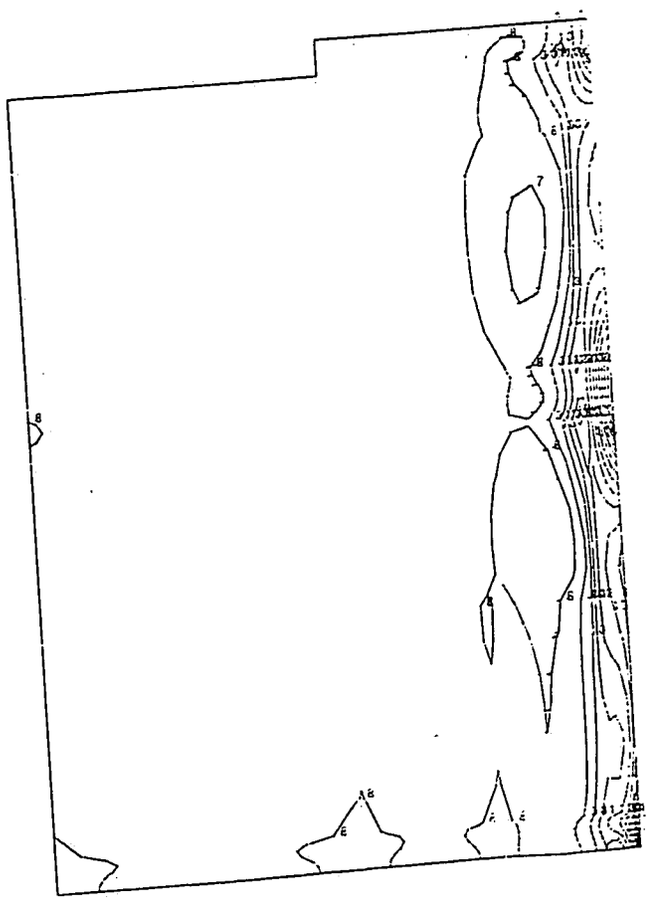

DEFLECTED STRUCTURE IDEALIZATION #2 $\Delta T = +20°C$

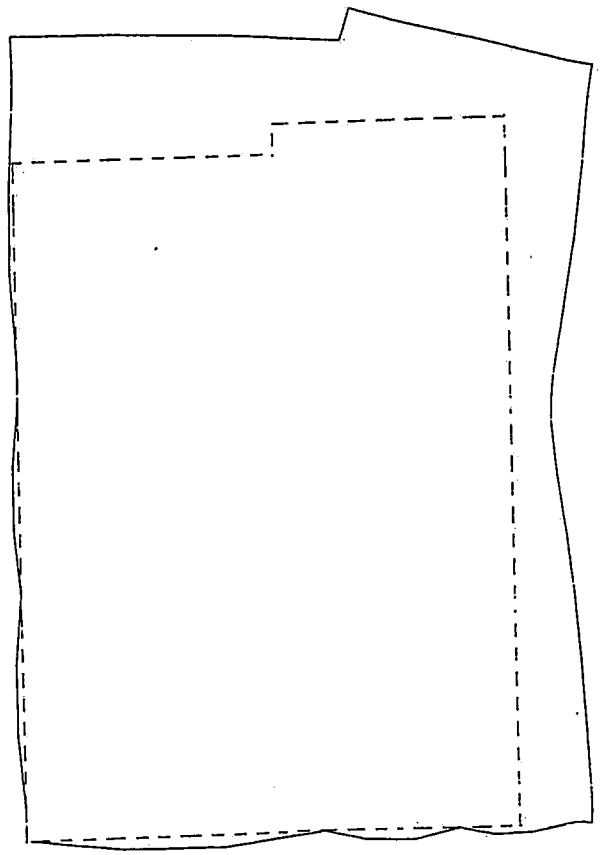

CONTOUR VALUES VON MISES STRESSES IDEALIZATION #2 ΔT = +20°C

1--	.17E+03
2--	.16E+04
3--	.31E+04
4--	.46E+04
5--	.60E+04
6--	.75E+04
7--	.90E+04
8--	.10E+05
9--	.12E+05
10--	.13E+05
11--	.15E+05
12--	.16E+05
13--	.18E+05
14--	.19E+05
15--	.21E+05
16--	.22E+05
17--	.24E+05
18--	.25E+05
19--	.27E+05
20--	.28E+05
21--	.30E+05

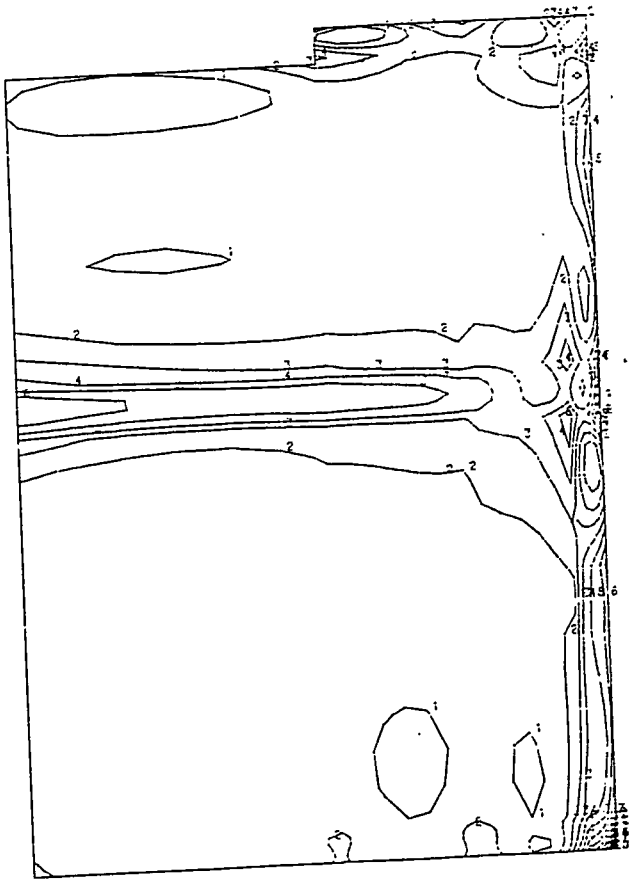

CONTOUR VALUES Y STRESSES IDEALIZATION #2 ΔT = +20°C

1--	-.13E+05
2--	-.11E+05
3--	-.93E+04
4--	-.76E+04
5--	-.59E+04
6--	-.43E+04
7--	-.26E+04
8--	-.91E+03
9--	.77E+03
10--	.24E+04
11--	.41E+04
12--	.58E+04
13--	.75E+04
14--	.91E+04
15--	.11E+05
16--	.12E+05
17--	.14E+05
18--	.16E+05
19--	.18E+05
20--	.19E+05
21--	.21E+05

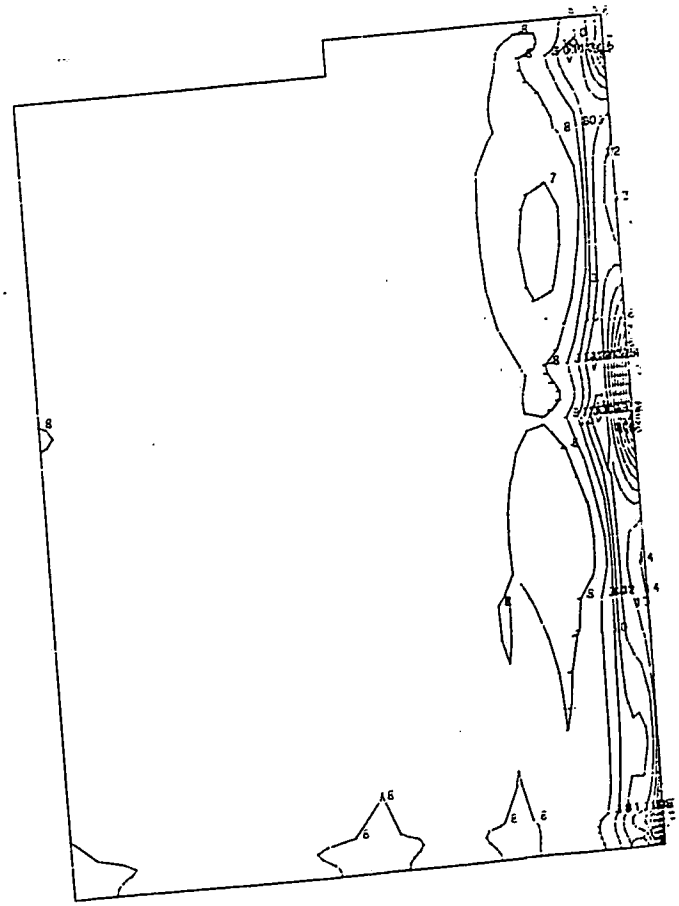

DEFLECTED STRUCTURE IDEALIZATION #2 $\Delta T = +30°C$

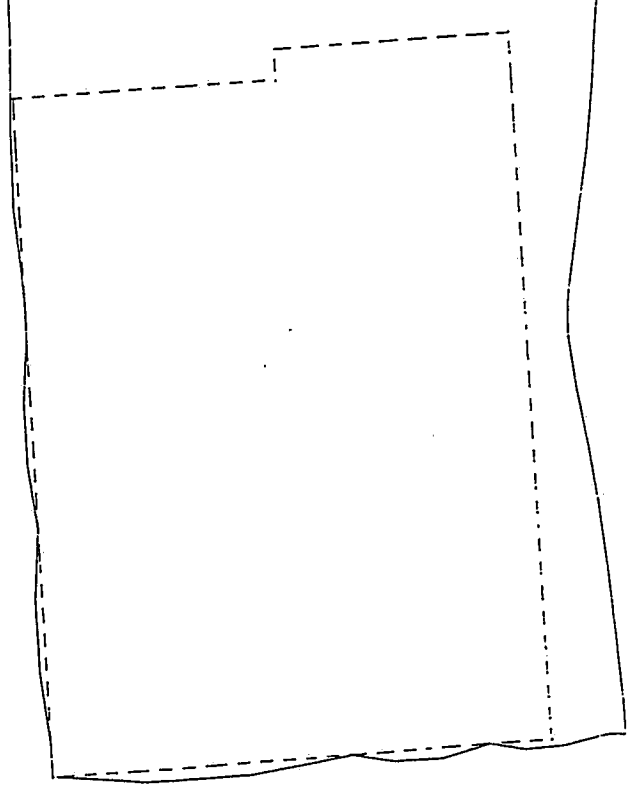

CONTOUR VALUES VON MISES STRESSES IDEALIZATION #2 ΔT = +30°C

1--	.26E+03
2--	.25E+04
3--	.47E+04
4--	.69E+04
5--	.91E+04
6--	.11E+05
7--	.13E+05
8--	.16E+05
9--	.18E+05
10--	.20E+05
11--	.22E+05
12--	.24E+05
13--	.27E+05
14--	.29E+05
15--	.31E+05
16--	.33E+05
17--	.35E+05
18--	.38E+05
19--	.40E+05
20--	.42E+05
21--	.44E+05

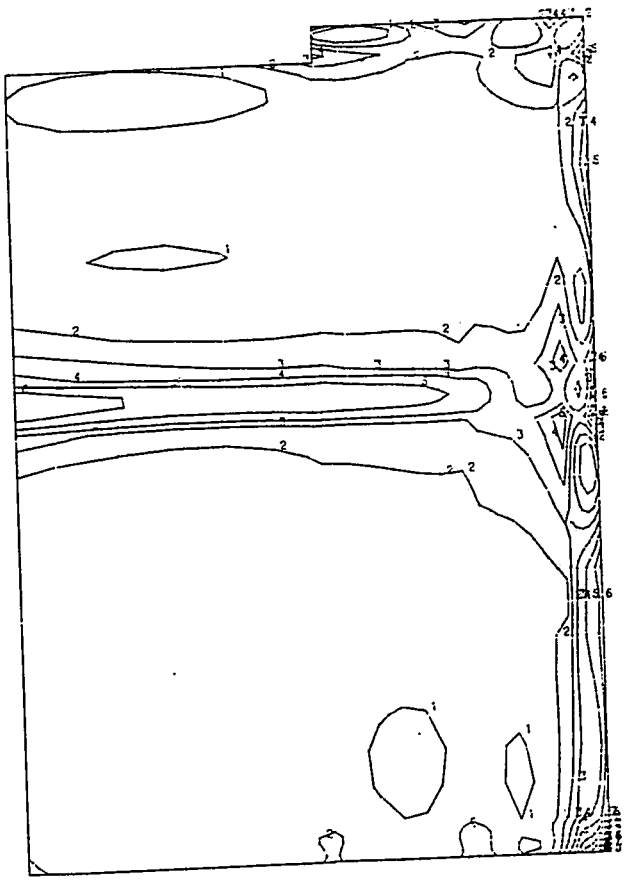

IDEALIZATION #2 ΔT = +30°C

CONTOUR VALUES v STRESSES

1--	-.19E+05
2--	-.16E+05
3--	-.14E+05
4--	-.11E+05
5--	-.89E+04
6--	-.64E+04
7--	-.39E+04
8--	-.14E+04
9--	.11E+04
10--	.37E+04
11--	.62E+04
12--	.87E+04
13--	.11E+05
14--	.14E+05
15--	.16E+05
16--	.19E+05
17--	.21E+05
18--	.24E+05
19--	.26E+05
20--	.29E+05
21--	.31E+05

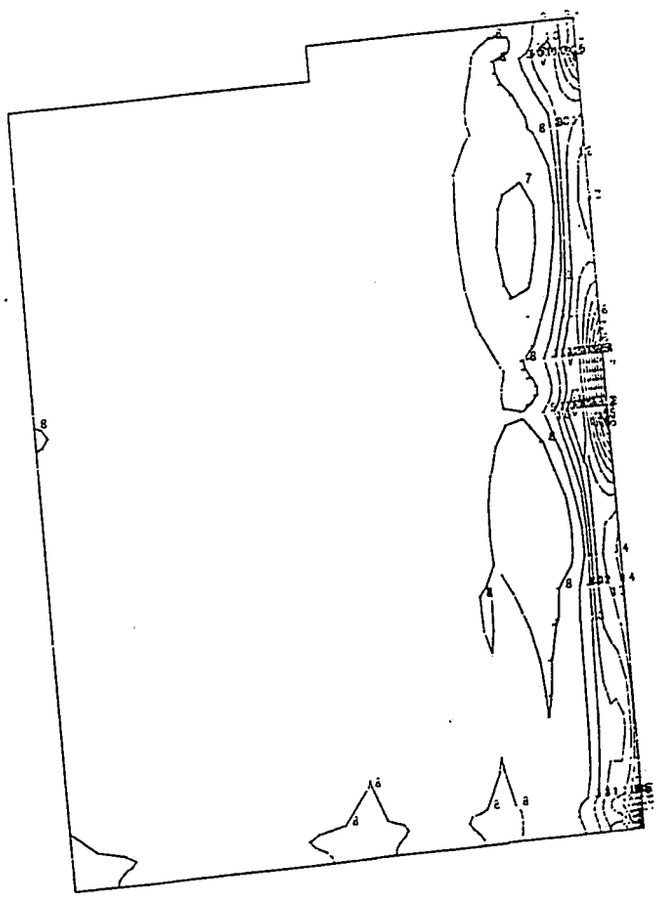

APPENDIX II

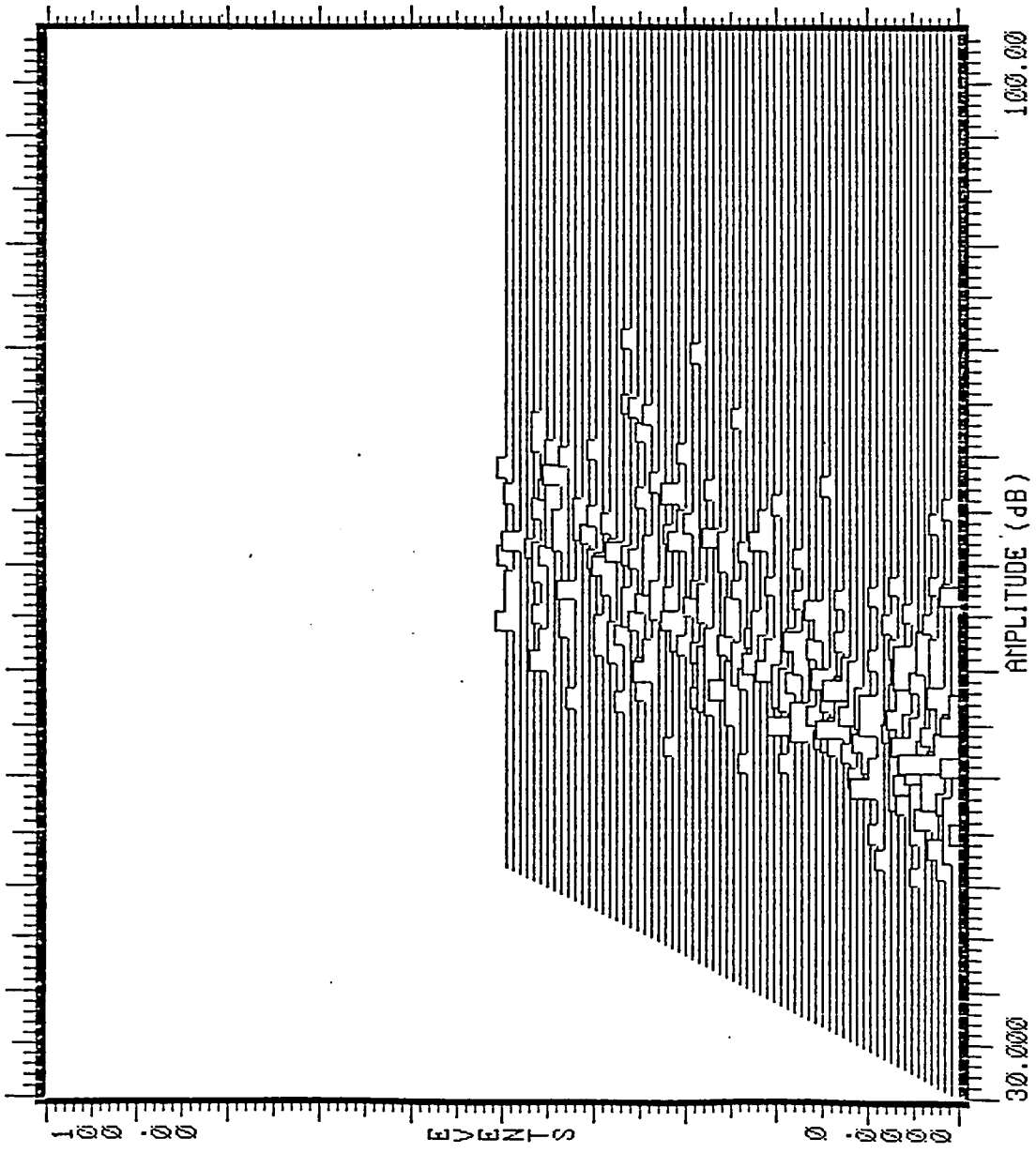

Control Group +/- 0.010% Strain Range

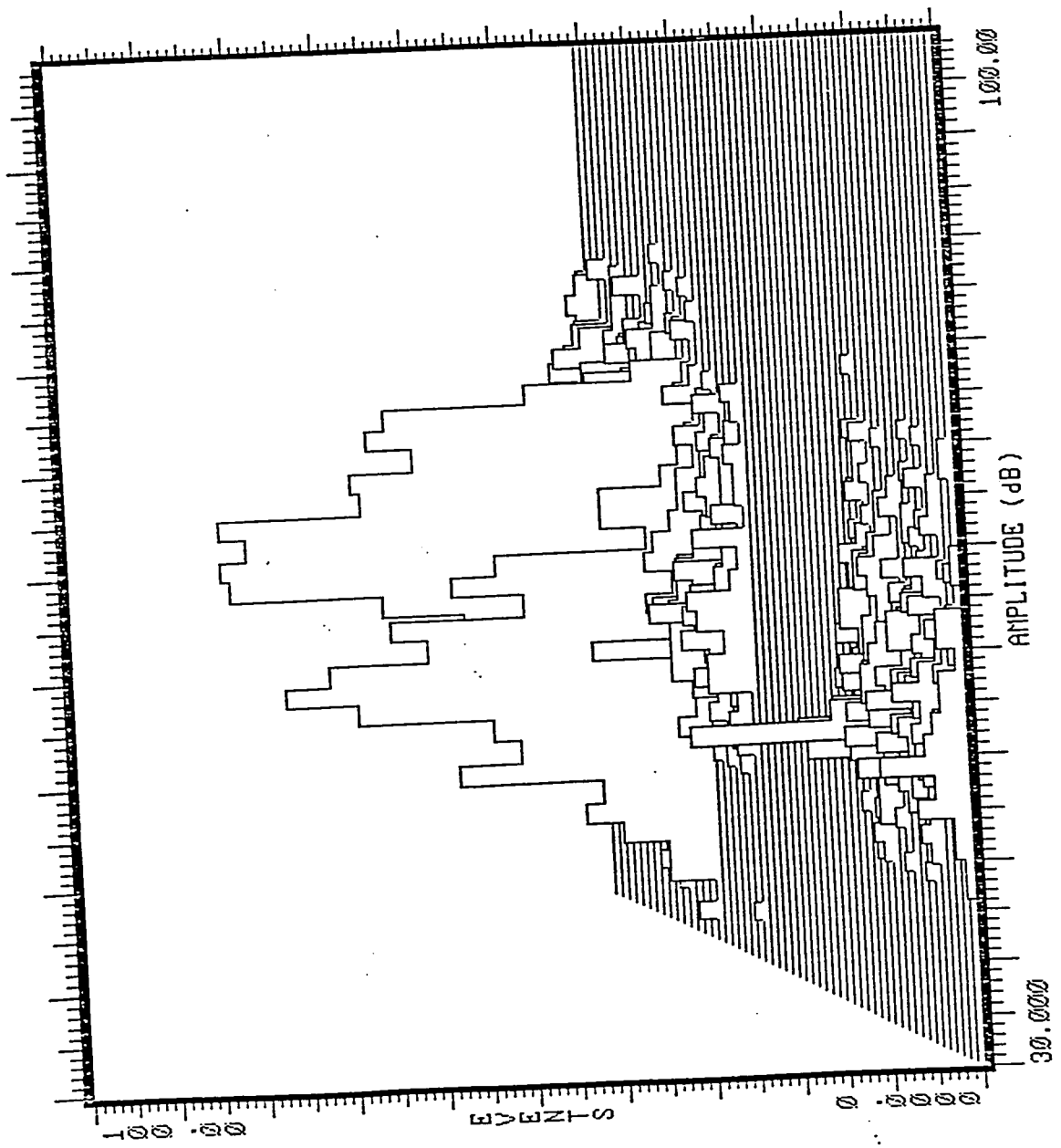

Control Group +/- 0.023% Strain Range

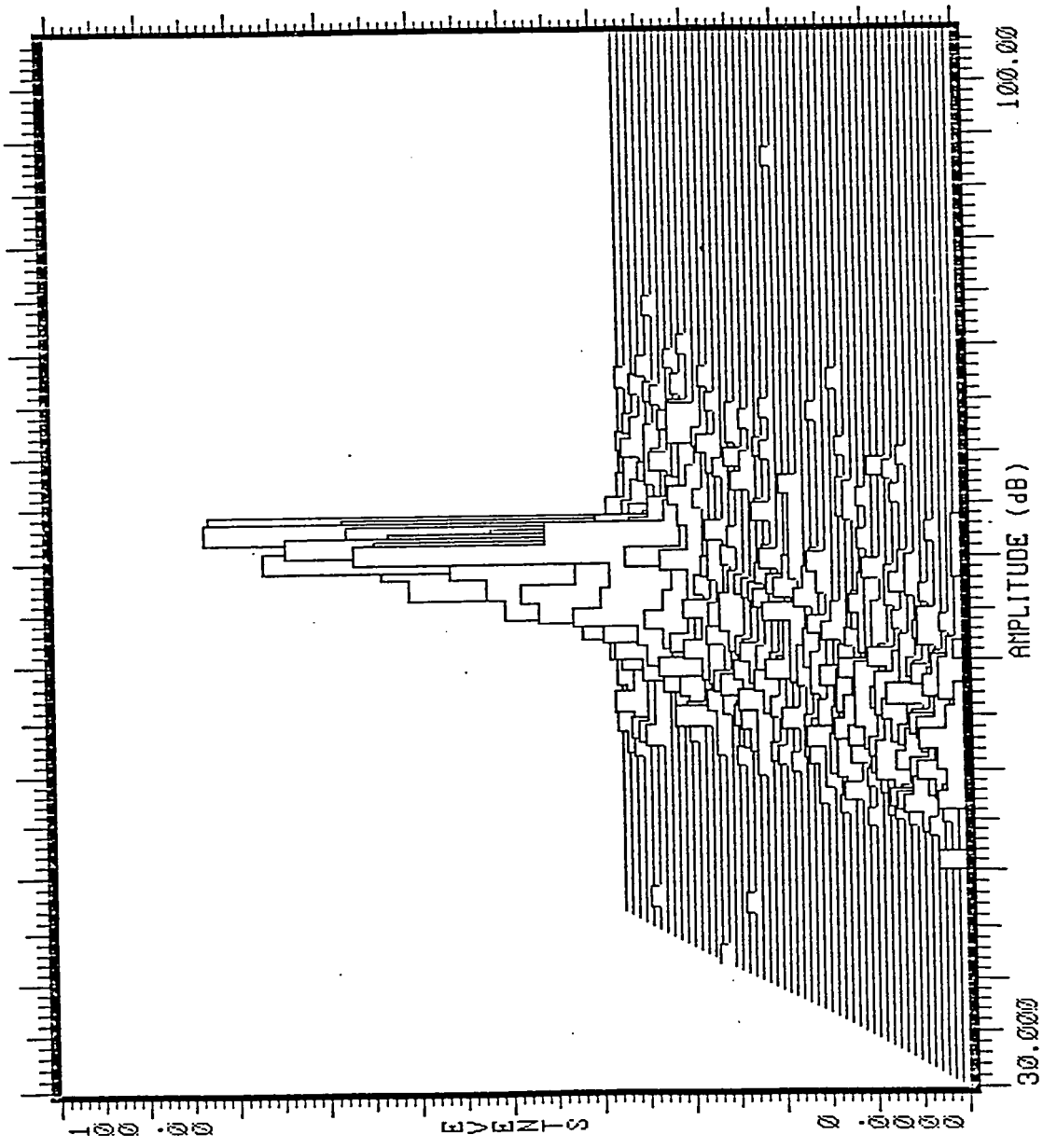

Control Group +/- 0.035% Strian Range

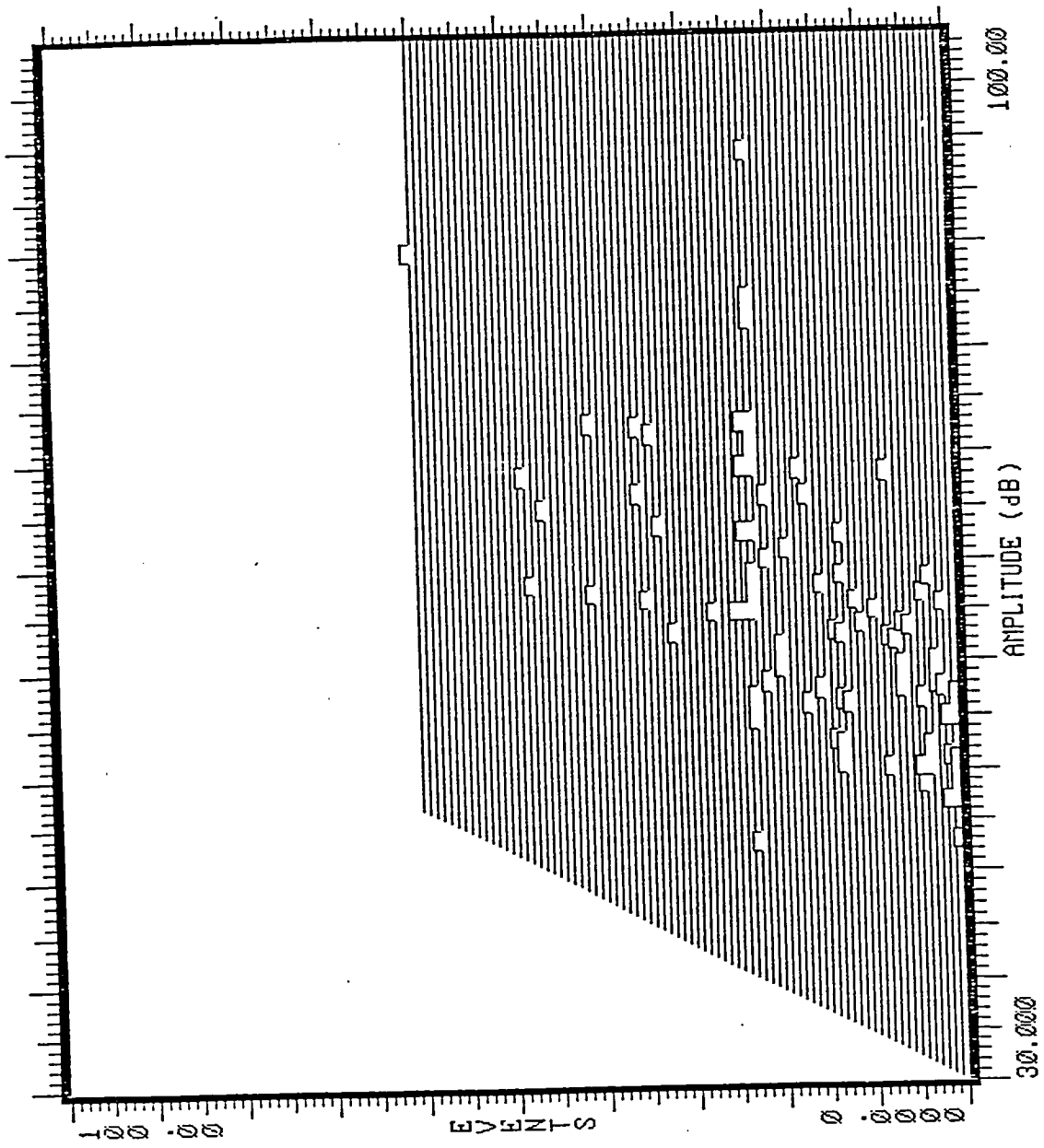

1 Micron Polished +/- 0.010% Strain Range

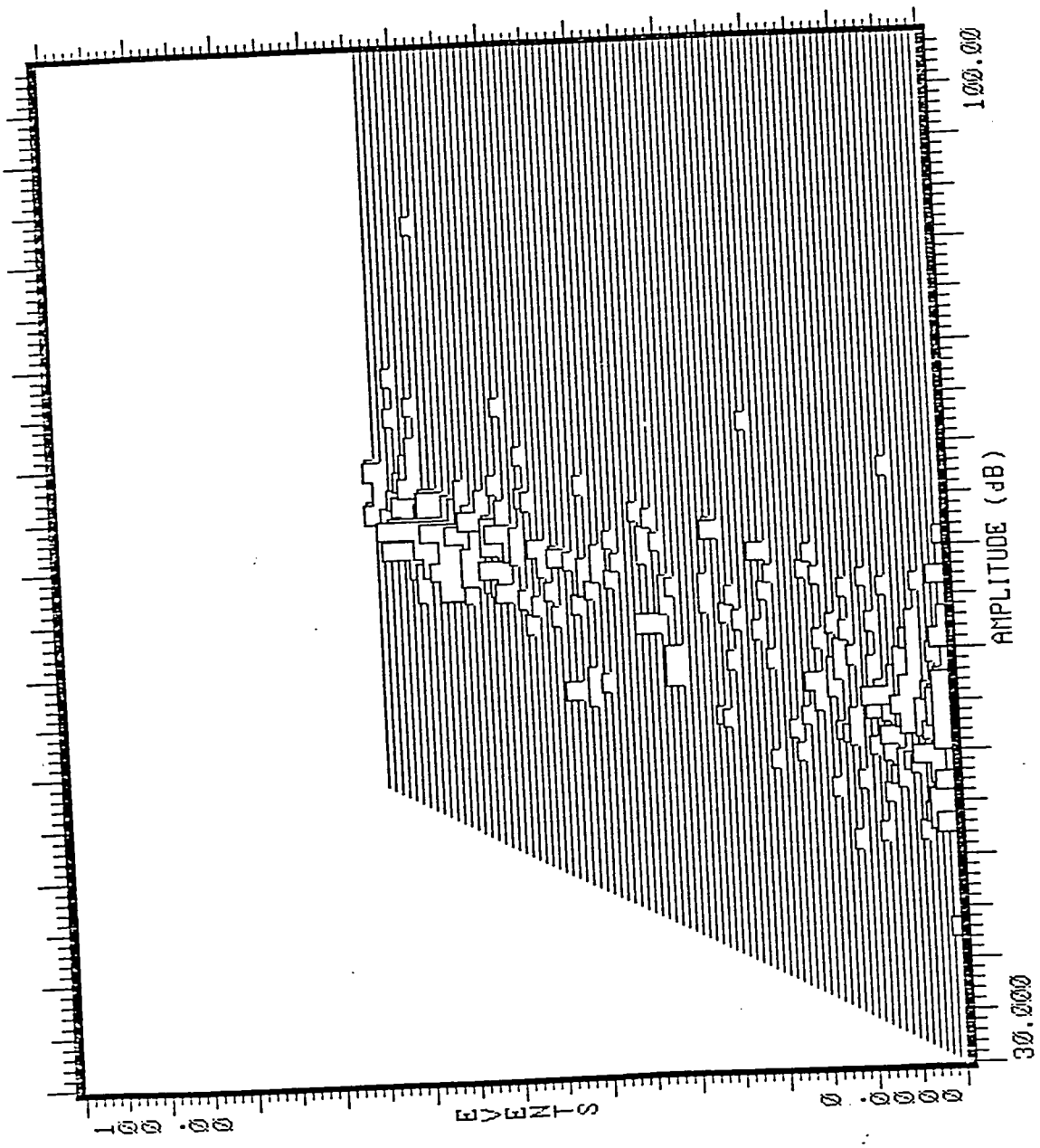

1 Micron Polished +/- 0.023% Strain Range

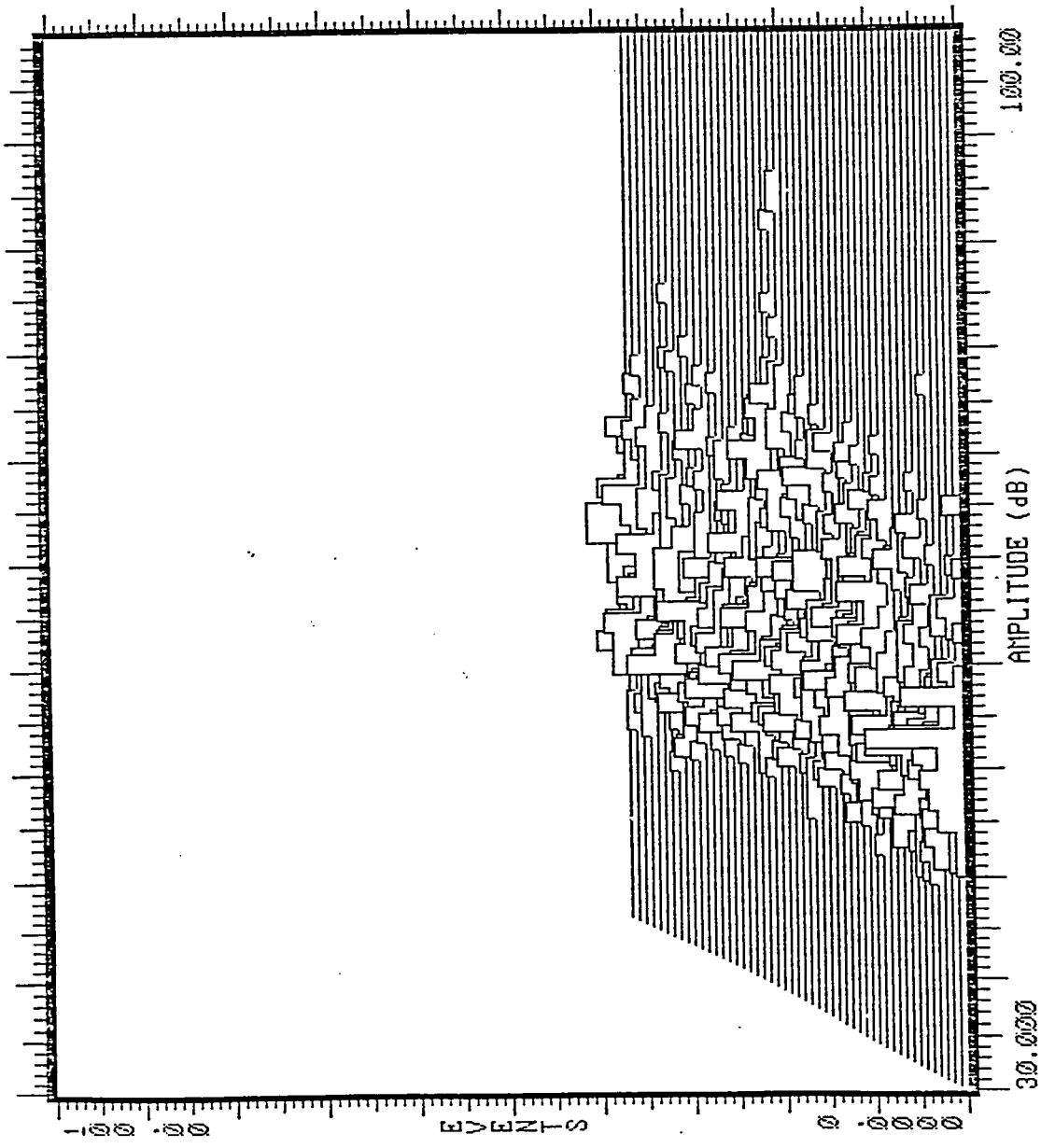

1 Micron Polished +/- 0.035% Strain Range

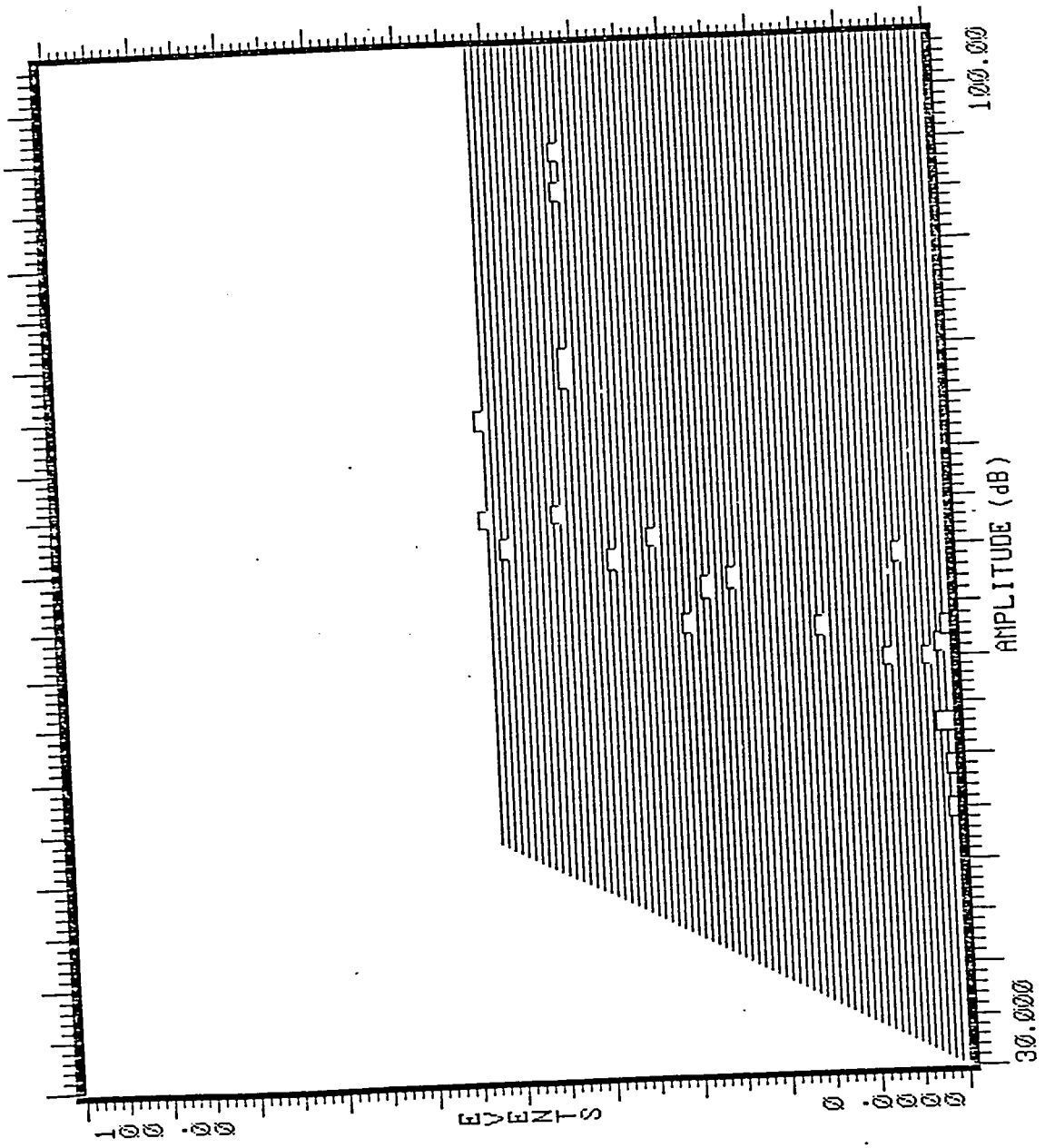

6 Micron Polished +/- 0.010% Strain Range

6 Micron Polished +/- 0.023% Strain Range

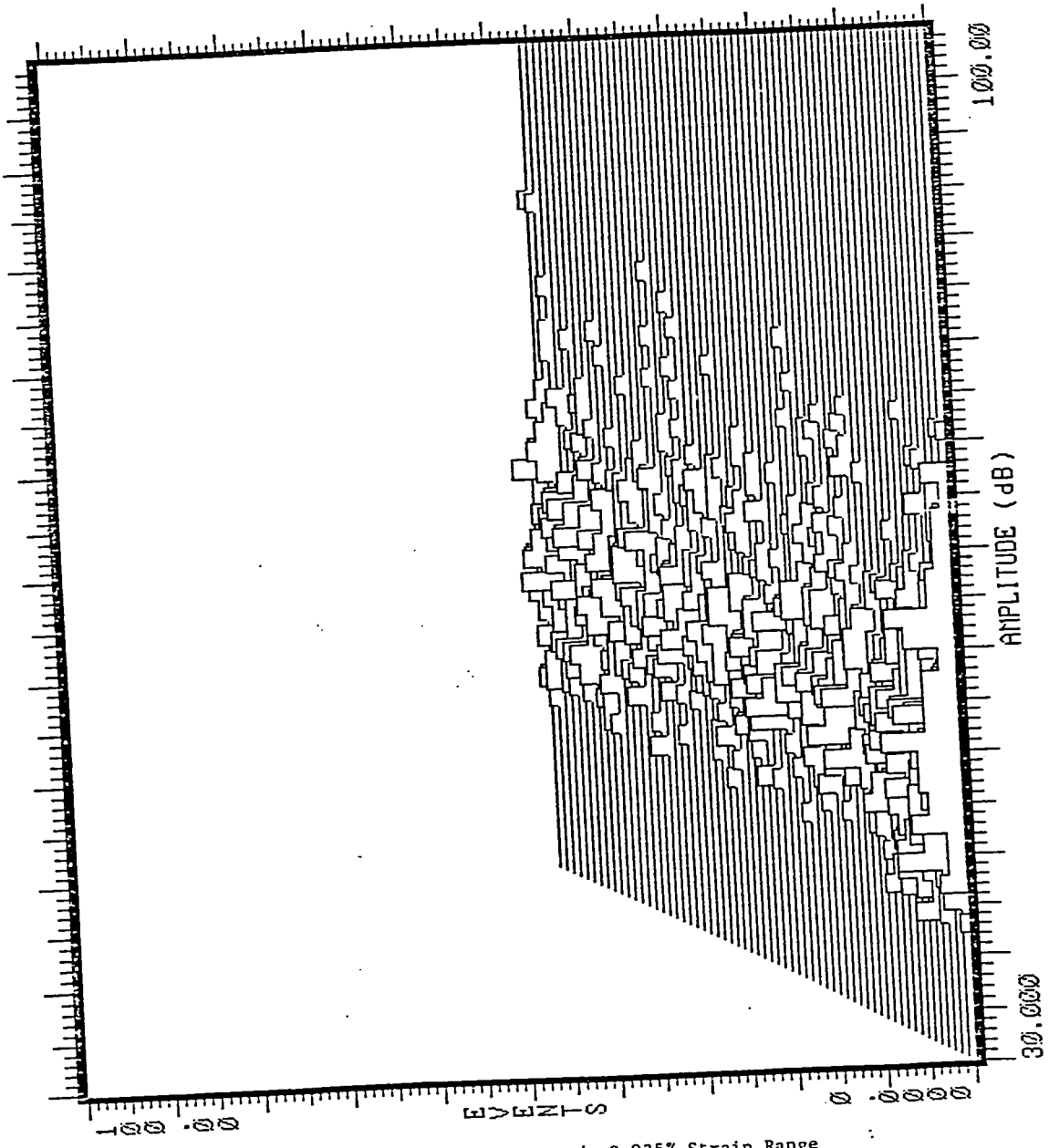

6 Micron Polished +/- 0.035% Strain Range

100.00
EVENTS
0.0000
30.000
AMPLITUDE (dB)
100.00
Aspect Ratio 6:1 +/- 0.010% Strain Range

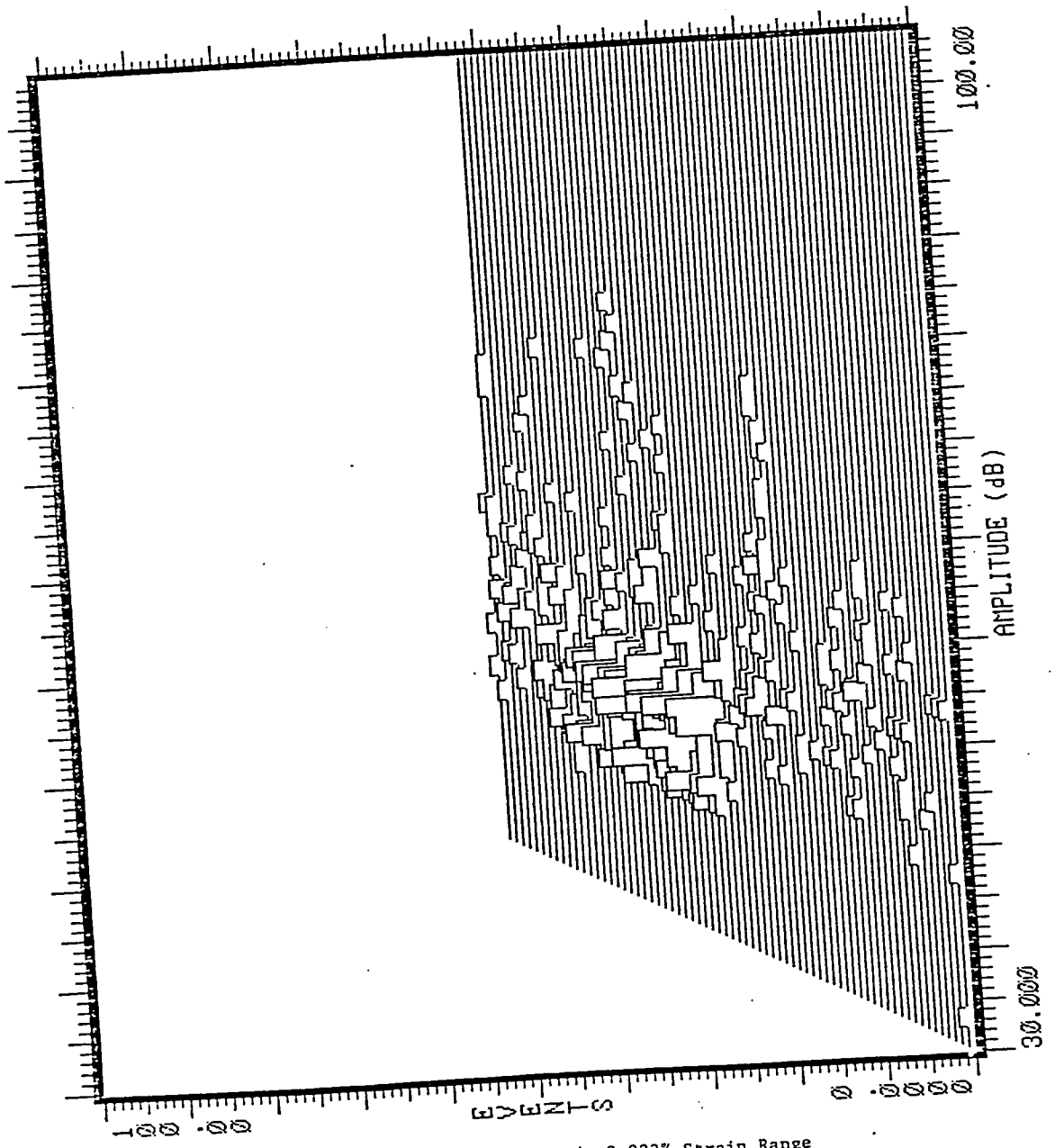

Aspect Ratio 6:1 +/- 0.023% Strain Range

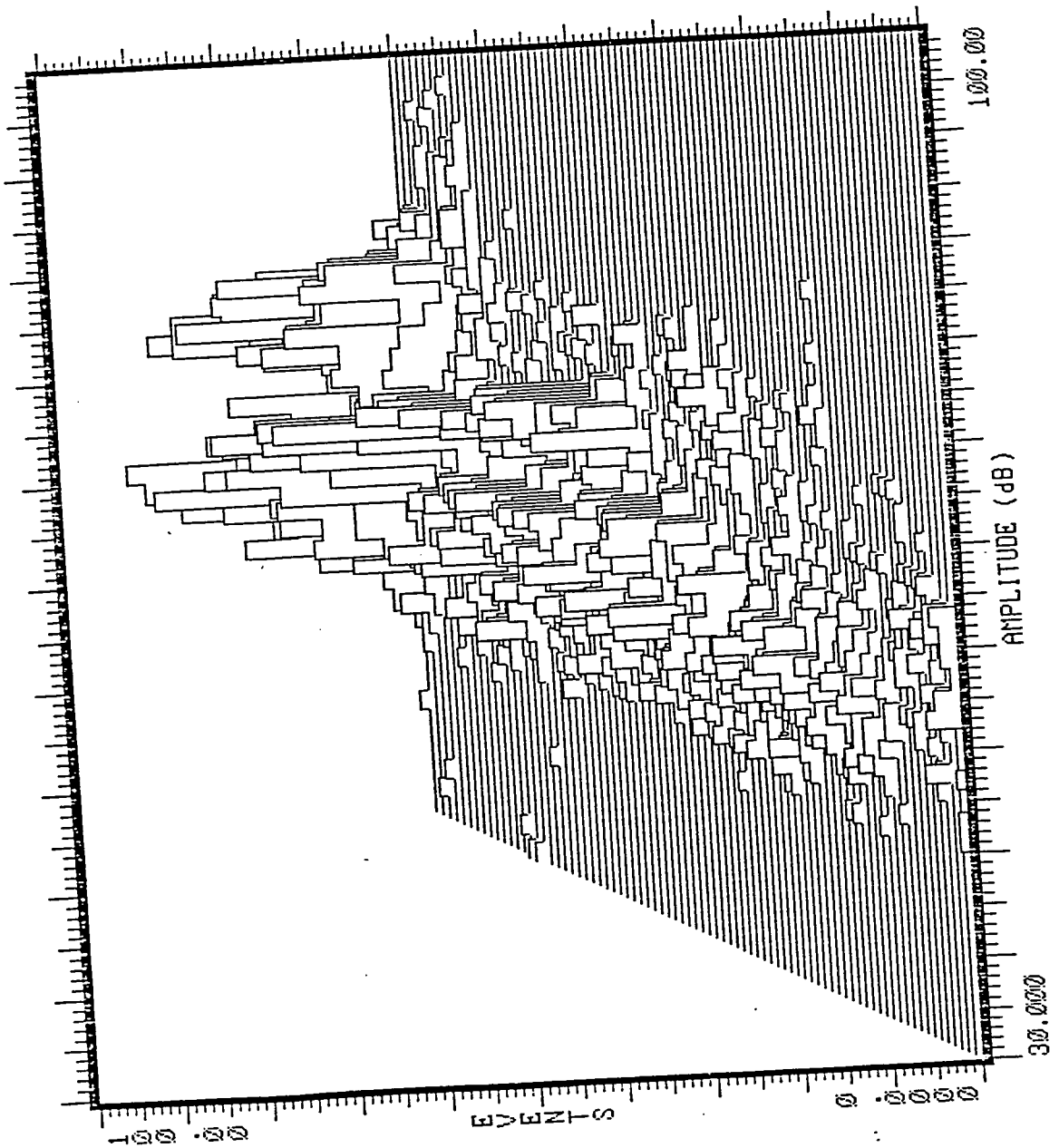

Aspect Ratio 6:1 +/- 0.035% Strain Range

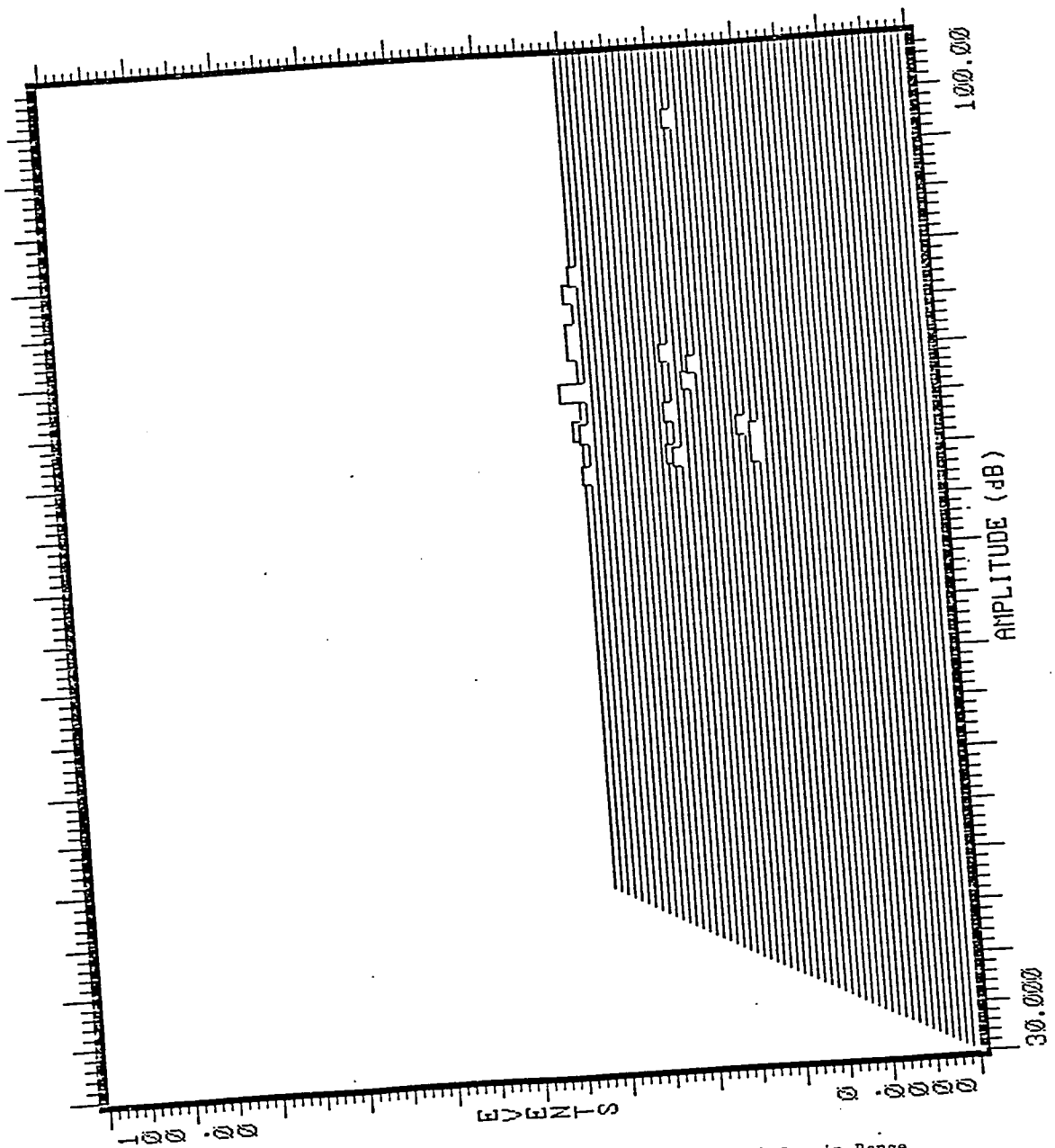

"Contaminated" Low Ductility Copper +/- 0.010% Strain Range

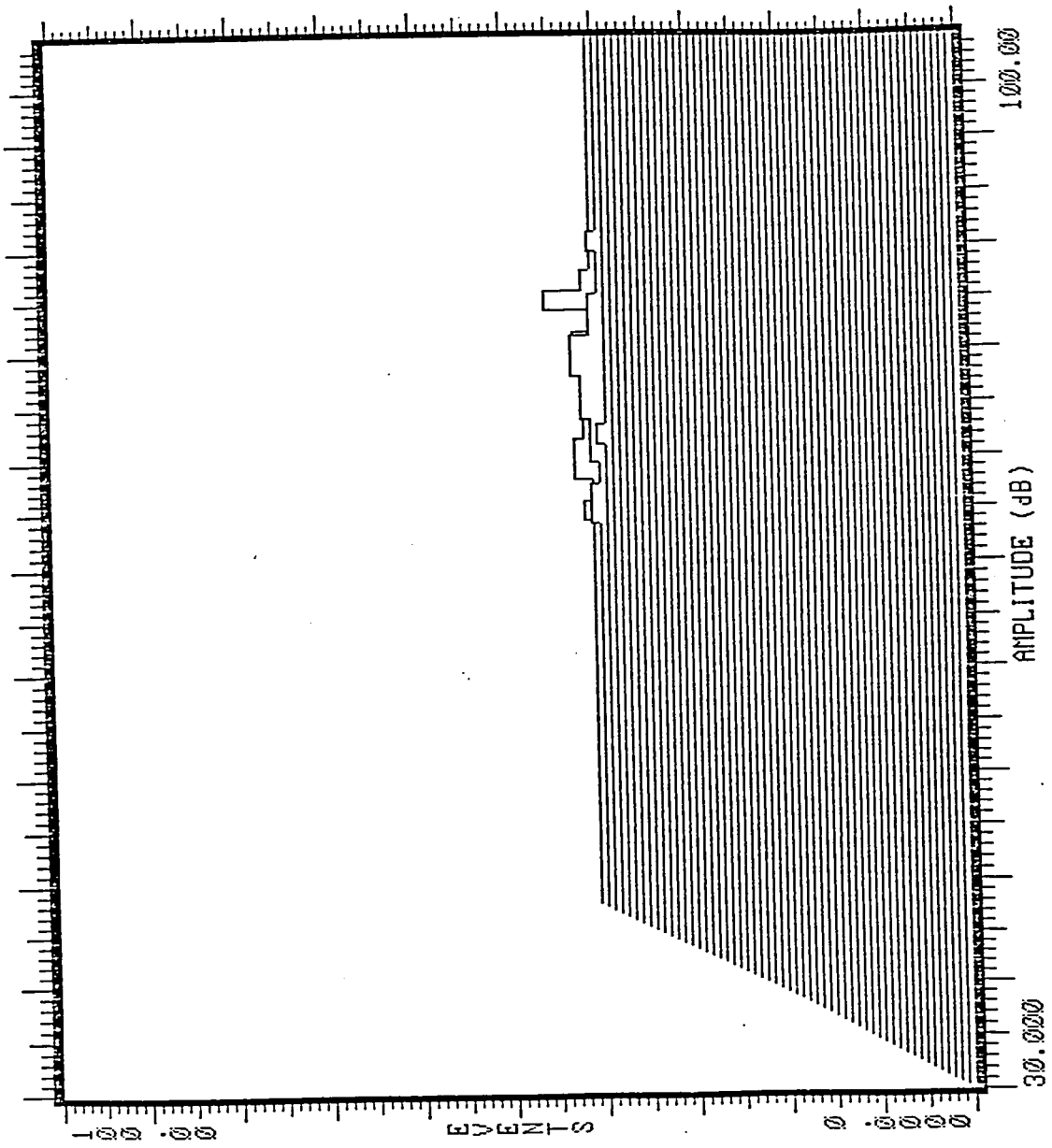

"Contaminated" Low Ductility Copper +/- 0.023% Strain Range

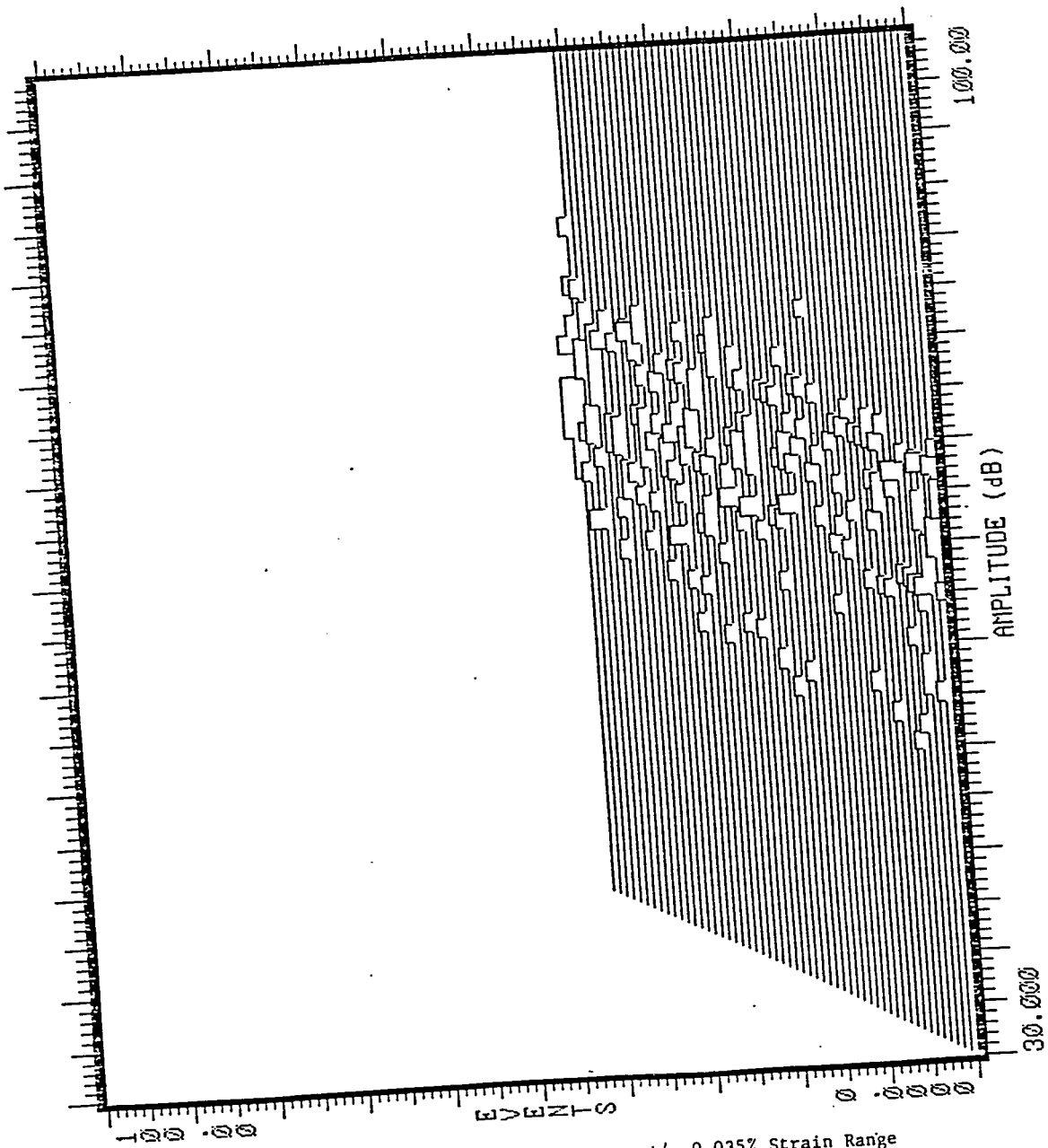

"Contaminated" Low Ductility Copper +/- 0.035% Strain Range

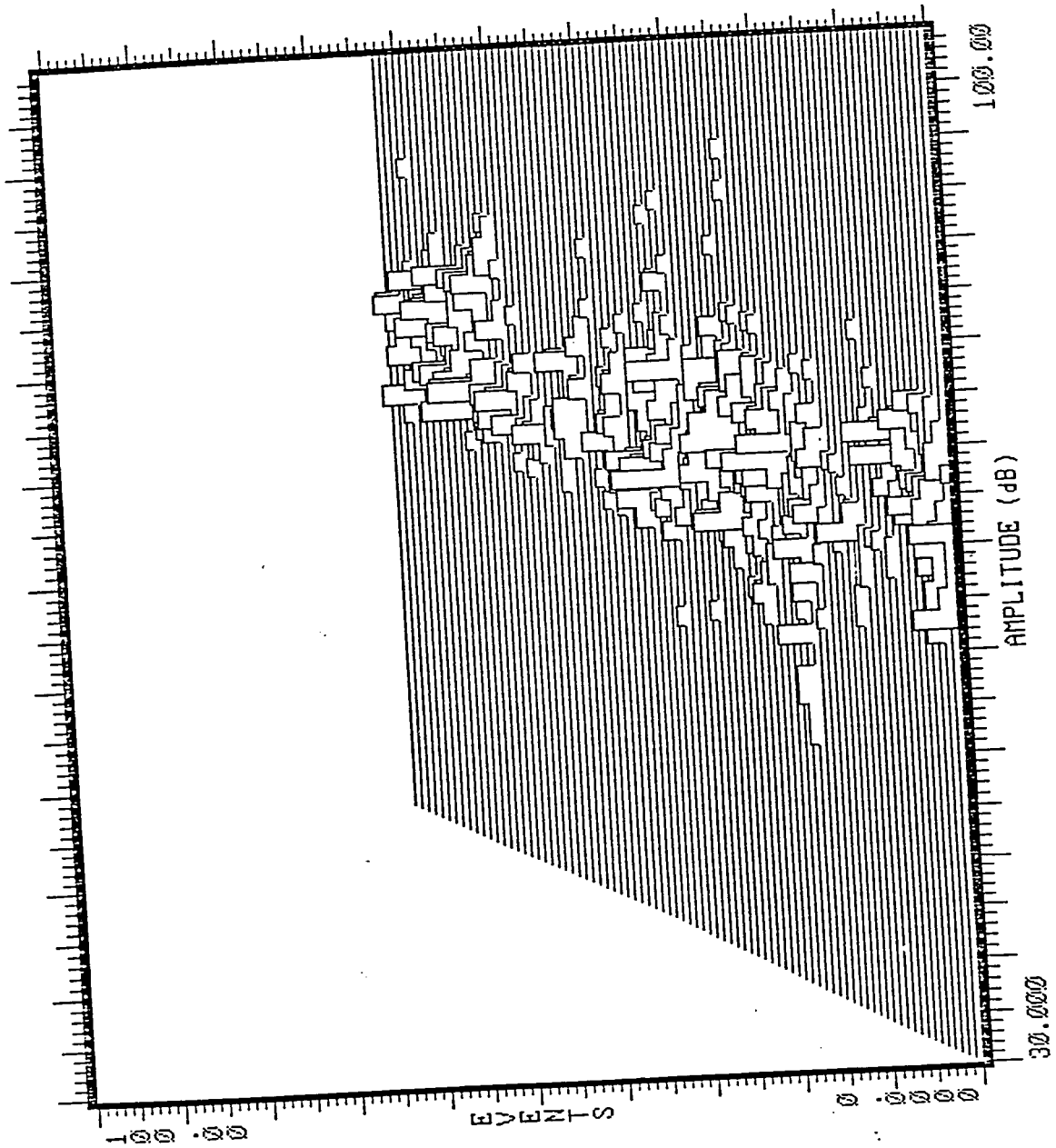

Activator #1 +/- 0.010% Strain Range

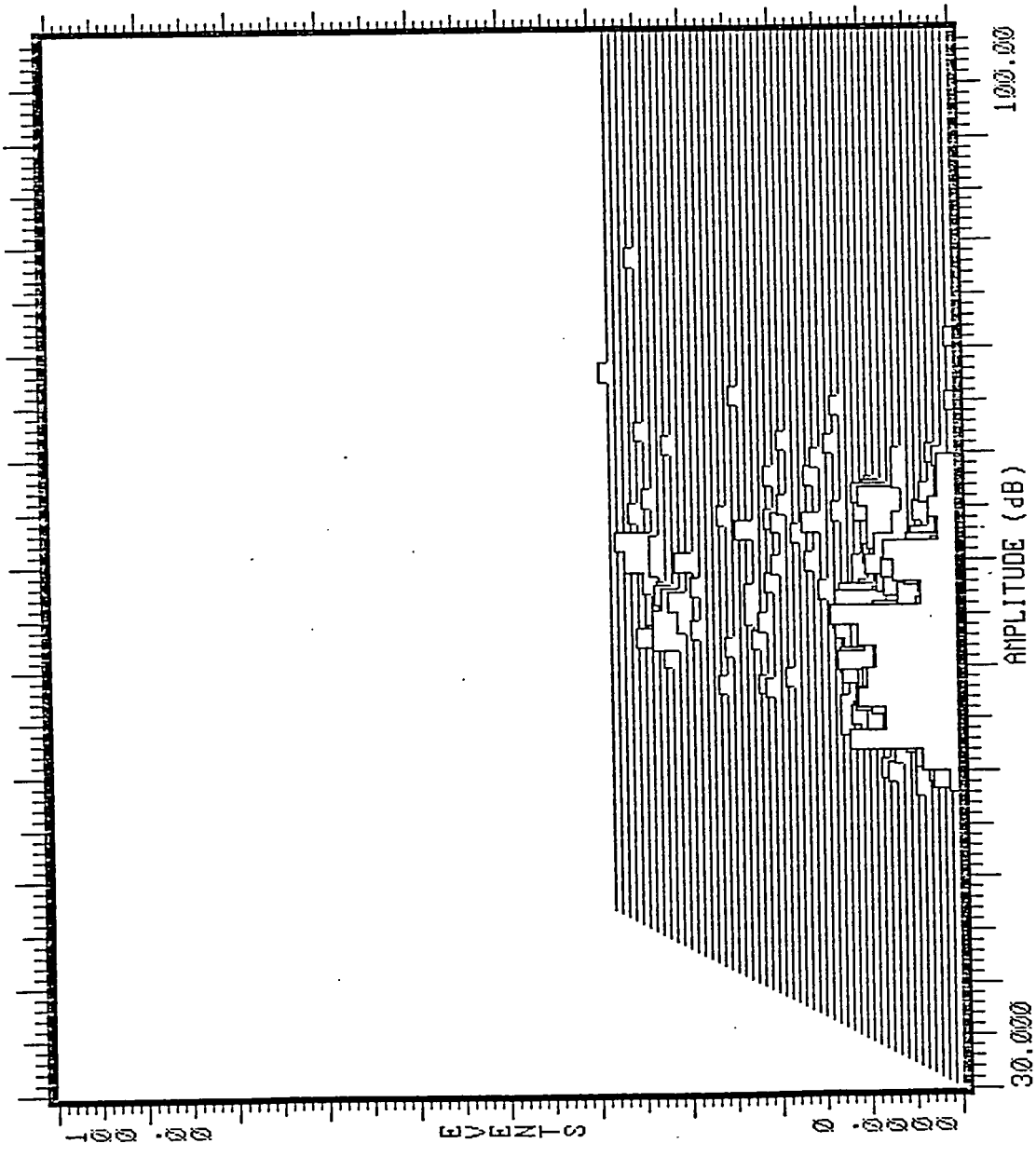

Activator #1 +/- 0.023% Strain Range

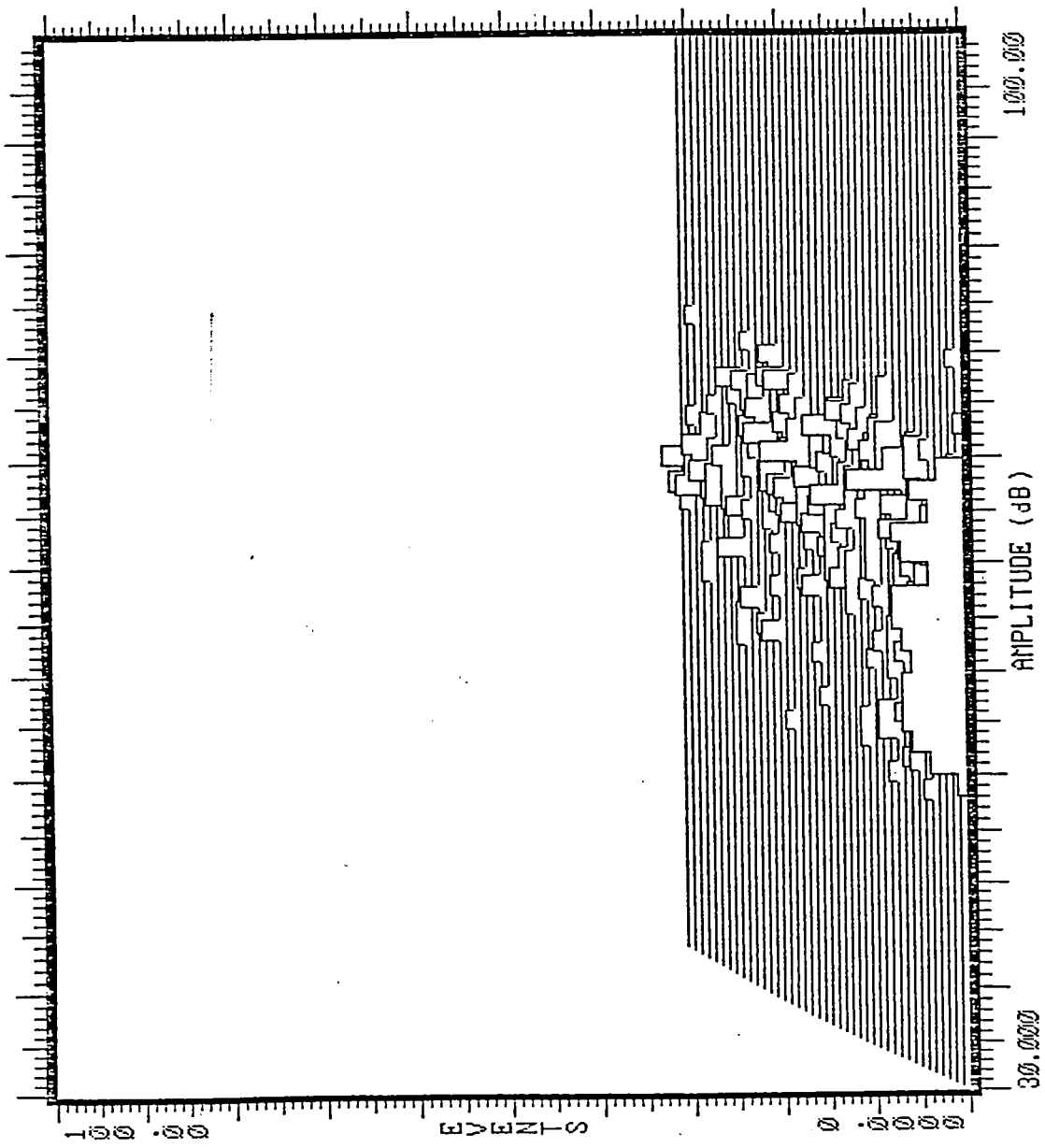

Activator #1 +/- 0.035% Strain Range

LIST OF ACRONYMS

PTH	Plated-through-hole
MIB	Multilayer interconnection board
AE	Acoustic emission
SCF	Cyclic strain fatigue
PAC	Physical Acoustic Corporation
APES	Axisymmetric/Planar Elastic Structures
FEA	Finite element analysis
SEM	Scanning electron microscope
TEM	Transmission electron microscope
STEM	Scanning transmission electron microscope
AEM	Analytical electron microscopy
AES	Auger electron spectroscopy
EDS	Energy dispersive x-ray spectroscopy
CBED	Convergent beam electron diffraction
HOLZ	High order laue zone
CB	Coherent bremsstrahlung
ZAP	Zone axis pattern

VITA

Kenneth S. Vecchio was born to Anthony and Elizabeth Vecchio on February 14, 1961, in Brooklyn, New York. He received his secondary education at Archbishop Molloy High School in New York City and was graduated in June 1979. In the fall of the same year, he entered Carnegie-Mellon University and was awarded a Bachelor of Science Degree in Metallurgical Engineering and Materials Science in June 1983.

Since September 1983, he has pursued his graduate education in the Department of Metallurgy and Materials Engineering at Lehigh University. While at Lehigh, he has been elected to the Sigma Xi Scientific Research Society, received a Presidential Scholarship from the Electron Microscope Society of America (EMSA), and is a joint member of ASM-AIME. He is currently a Research Assistant and an instructor in the Department of Metallurgy and Materials Engineering and was awarded a University Tuition Scholarship to pursue his doctorate. He has two technical publications in print or pending.